UNIVERSITY OF CALIFORNIA, SAN DIEGO

On the Dynamics of Inviscid Relaxation in 2D Fluids and Nonneutral Plasmas

A dissertation submitted in partial satisfaction of the

requirements for the degree Doctor of Philosophy

in Physics

by

David Anton Schecter

Committee in charge:

Daniel H. E. Dubin, Chairman
George F. Carnevale
C. Fred Driscoll
Thomas M. O'Neil
William R. Young

1999

The dissertation of David Anton Schecter is approved, and it is acceptable in quality and form for publication on microfilm:

Chairman

University of California, San Diego

1999

Table of Contents

List of Figures

Acknowledgements

I gratefully acknowledge the support of my thesis advisor Dr. Daniel H. E. Dubin, whose contributions to this dissertation are immense. With the same gratitude, I acknowledge the support and contributions of my unofficial advisors, Dr. C. Fred Driscoll and Dr. Thomas M. O'Neil.

I have enjoyed several conversations with Dr. George F. Carnevale and Dr. William R. Young, of the Scripps Institute of Oceanography. They gave me a broader perspective on my research, as it pertains to problems in oceanography and meteorology. I thank them for being members of my thesis committee.

I also thank Dr. Francois Anderegg, Dr. Ann C. Cass, Dr. Noel R. Corngold, James R. Danielson, Dr. Kevin S. Fine, Terry J. Hilsabeck, Dr. Eric M. Hollmann, Dr. Dezhe Jin, Dr. Jason M. Kriesel, Dr. Ilya M. Lansky, Dr. Tihiro Ohkawa and Dr. Ross L. Spencer for providing useful insight and constructive criticism during the course of my research. My conversations with Drs. Cass, Fine, Jin and Lansky were most frequent, and especially useful to my thesis. I thank Dr. W. Greg Flynn for his work on the cylindrical vortex-in-cell simulation that was used for Chapters 2 and 4. Finally, I thank Jo Ann Christina for help in preparing this manuscript.

Part of Chapter 2 of this dissertation has been published in Physical Review Letters, D. A. Schecter and D. H. E. Dubin, **83**, 2191-2194 (1999). Part of Chapter 3 will appear in the AIP Proceedings of the 1999 Nonneutral Plasmas Workshop,

D. A. Schecter, D. H. E. Dubin, A. C. Cass, C. F. Driscoll, I. M. Lansky and T. M. O'Neil, ed. J. J. Bollinger. Chapter 4 has been published in Physics of Fluids, D. A. Schecter, D. H. E. Dubin, K. S. Fine and C. F. Driscoll, **11**, 905-914 (1999). D. A. Schecter was the primary investigator and author of these papers.

This research was supported financially by the National Science Foundation (NSF PHY94-21318) and the Office of Naval Research (ONR N00014-96-1-0239).

Vita, Publications and Fields of Study

Vita

25 December 1972	Born, Louisville, Kentucky
1994	B.A., University of Chicago
1994	Research Assistant, Department of Physics, University of Chicago
1994-1996	Teaching Assistant, Department of Physics, University of California, San Diego
1995-1999	Research Assistant, Department of Physics, University of California, San Diego
1995	M.S., University of California, San Diego
1999	Ph.D., University of California, San Diego

Publications

1. D.A. Schecter and D.H.E. Dubin, "Vortex motion driven by a background vorticity gradient," Phys. Rev. Lett. **83**, 2191-2194 (1999). Also to appear in the AIP Proceedings of the 1999 Nonneutral Plasmas Workshop, ed. J.J. Bollinger.

2. D.A. Schecter, D.H.E. Dubin, K.S. Fine and C.F. Driscoll, "Vortex crystals from 2D Euler flow: Experiment and simulation," Phys. Fluids **11**, 905-914 (1999).

3. C.F. Driscoll, D.A. Schecter, D.Z. Jin, D.H.E. Dubin, K.S. Fine and A.C. Cass, "Relaxation of 2D turbulence to vortex crystals," Physica A **263**, 284-292 (1999).

4. I.M. Lansky, T.M. O'Neil and D.A. Schecter, "A theory of vortex merger," Phys. Rev. Lett. **79**, 1479-1482 (1997).

5. C.-H. Liu, S.R. Nagel, D.A. Schecter, S.N. Coppersmith, S. Majumdar, O. Narayan and T.A. Witten, "Force fluctuations in bead packs," Science **269**, 513 (1995).

6. D.A. Schecter, D.H.E. Dubin, A.C. Cass, C.F. Driscoll, I.M. Lansky and T.M. O'Neil, "Inviscid damping of elliptical perturbations on a 2D vortex," AIP Proceedings of the 1999 Nonneutral Plasmas Workshop, ed. J.J. Bollinger, in press.

7. C.F. Driscoll, D.Z. Jin, D.A. Schecter, E.J. Moreau and D.H.E. Dubin, "Dynamics, statistics and vortex crystals in the relaxation of 2D turbulence," Physica Scripta: Proceedings of Intl. Topical Conf. on Plasma Physics, in press. Also to appear in the Proceedings of the 5th Experimental Chaos Conference, in press.

Fields of Study

Major Field: Physics

Studies in Mathematical Physics
Professor Kim Greist

Studies in Theoretical Mechanics
Professors Donald R. Fredkin and Benjamin Grinstein

Studies in Advanced Classical Electrodynamics
Professor Thomas M. O'Neil

Studies in Plasma Physics
Professors Daniel H. E. Dubin and Vitali D. Shapiro

Studies in Fluid Mechanics
Professor W. Kendall Melville

Studies in Equilibrium Statistical Mechanics
Professor Daniel H. E. Dubin

Studies in Nonequilibrium Statistical Mechanics
Professor Patrick H. Diamond

Studies in Nonlinear and Nonequilibrium Dynamics of Physical Systems
Professor Patrick H. Diamond

Studies in Renormalization in Field Theory, the Renormalization Group and Critical Phenomena
Professor Terence T. Hwa

Studies in Quantum Mechanics
Professor Roger F. Dashen

Studies in Particles and Fields
Professor Julius Kuti

Abstract of the Dissertation

On the Dynamics of Inviscid Relaxation in 2D Fluids and Nonneutral Plasmas

by

David Anton Schecter
Doctor of Philosophy in Physics
University of California, San Diego, 1999
Professor Daniel H. E. Dubin, Chairman

Two-dimensional (2D) flows in atmospheres, oceans and plasmas can rapidly relax to metastable patterns before viscosity affects the dynamics. This dissertation is on the mechanics of inviscid relaxation. Three topics are covered: vortex motion driven by a background vorticity gradient, the inviscid damping (Landau damping) of asymmetries on a circular vortex, and vortex crystal formation.

All topics were motivated by experiments with magnetized electron columns, where the (r, θ) flow of electrons is approximately governed by the 2D Euler equations. These equations also govern 2D inviscid incompressible uniform-density fluids.

In one experiment, a turbulent flow relaxed through the migration of vortices to extrema in the background vorticity. In Chapter 2, a theory describing this vortex motion is developed. Generally, the vortex speed is proportional to the background vorticity gradient; however, a vortex that is prograde with respect to the background shear moves slower than a retrograde vortex of equal strength.

Separate theories are given for the motion of prograde and retrograde vortices. Both theories compare favorably to simulations and the experiment.

In Chapter 3, the rate at which a perturbed vortex relaxes toward an axisymmetric equilibrium is examined using linear perturbation theory. The initial perturbation is created by the brief application of an external flow field, modelling recent experiments. In the core of the vortex, the perturbation typically behaves like an exponentially damped normal mode. An eigenmode analysis shows that this "quasi-mode" is actually a wave-packet of neutral continuum modes that decays through interference as the continuum modes disperse. Physically, a quasi-mode decays to conserve total angular momentum as vorticity is mixed in an outer resonance layer. Theoretical decay rates are found to agree with the experiments.

In Chapter 4, vortex-in-cell simulations of 2D Euler flow are compared directly to electron plasma experiments in which turbulent flows relax to vortex crystals. A vortex crystal is an array of intense vortices that rotates rigidly in a lower vorticity background. The simulations and the experiments relax to vortex crystals at the same rate, proving that vortex crystal formation in electron plasmas does not require physics beyond the 2D Euler equations. Vortex crystals are formed due to the mixing of background vorticity by the intense vortices, which has a cooling effect on the chaotic vortex motion.

Chapter 1

General Introduction

The free relaxation of two-dimensional (2D) turbulence has been actively studied for decades, with applications in astrophysics, geophysics and plasma physics [1-8]. One relaxation mechanism is viscosity, which causes the bulk kinetic energy of the flow to slowly dissipate. However, 2D flows typically relax to stationary patterns on much faster time scales, while conserving the bulk kinetic energy that was initially bound in the turbulence.

In this thesis we investigate three mechanisms of inviscid relaxation, in three self-contained chapters. In Chapter 2, we study vortex motion driven by a background vorticity gradient, which leads to the segregation of positive and negative vortices. In Chapter 3, we examine the inviscid damping (Landau damping) of waves on an extended vortex, which occurs through a resonant interaction with comoving fluid. In Chapter 4, we discuss the mixing of background vorticity by the action of several like-sign vortices, and the resulting formation of a vortex crystal equilibrium, which consists of several like-sign vortices locked in rigid rotation.

1.1 2D Fluid Experiments with Magnetized Electron Plasmas

All sections of this thesis were motivated by 2D fluid experiments with magnetized electron plasmas [8, 9, 10, 11]. Figure 1.1 shows the experimental apparatus. The electrons are contained in a hollow cylindrical conductor. Large DC voltages are applied at both ends of the cylinder, to confine the electrons axially. A uniform magnetic field B is applied parallel to the trap axis (z-axis), and prevents the electrons from escaping to the wall.

In these experiments, the electrons bounce rapidly from one end of the trap to the other (along the z-axis). As a result, the r-θ velocity of an electron can be approximated by its average velocity over a bounce period. The 2D fluid equations that are obtained from this bounce averaging scheme can be written for the z-averaged electron density $n(r, \theta, t)$, or the vorticity $\zeta(r, \theta, t)$. Both formulations of the fluid dynamics are shown in Fig. 1.2.

The equations for electron density are called the drift-Poisson equations. They are shown in the left column of Fig. 1.2. Here, $\vec{v}(r, \theta, t)$ is the $\vec{E} \times \vec{B}$ drift velocity field and $\phi(r, \theta, t)$ is the electrostatic potential, which vanishes at the wall

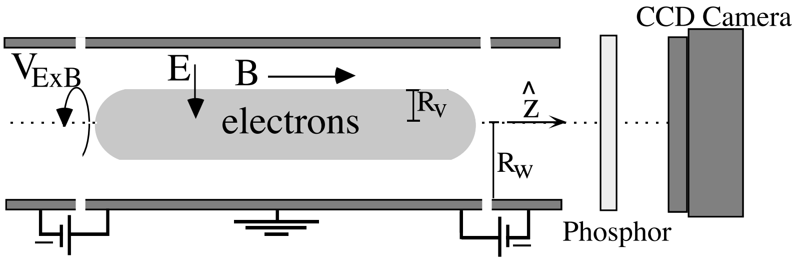

Figure 1.1: Experimental apparatus (Penning-Malmberg trap) for 2D fluid experiments with magnetized electron plasmas.

electron density n	vorticity ζ
$\vec{E} \times \vec{B}$ drift $\vec{v} = \hat{z} \times c\nabla\phi / B$	incompressible flow $\vec{v} = \hat{z} \times \nabla\psi$
Poisson's equation $\nabla^2\phi = 4\pi en$	Poisson's equation $\nabla^2\psi = \hat{z} \bullet \nabla \times \vec{v} \equiv \zeta$
advection of density $\frac{\partial n}{\partial t} + \vec{v} \bullet \nabla n = 0$	advection of vorticity $\frac{\partial \zeta}{\partial t} + \vec{v} \bullet \nabla \zeta = 0$

Figure 1.2: The approximate fluid equations for electron density n and the vorticity ζ of a magnetized electron plasma in a Penning-Malmberg trap. The boundary condition is $\phi, \psi = 0$ at the wall radius R_w.

radius R_w. The electron density is simply advected in the incompressible flow.

The equations for vorticity are the 2D Euler equations, which also govern inviscid incompressible uniform-density fluids. Here, $\psi(r, \theta, t)$ is a stream function that is related to the electrostatic potential by the equation $\psi = c\phi/B$. Comparing Poisson's equation for ϕ to Poisson's equation for ψ, we see that the vorticity is directly proportional to the electron density. That is, $\zeta = 4\pi ecn/B$. Therefore, the vorticity is advected with the electron density.

Because ζ is proportional to n, vorticity measurements are (theoretically) equivalent to density measurements. Thus, vorticity is measured by dumping the electrons onto a phosphor screen, and recording the density (vorticity) image with a CCD camera. Although this imaging is destructive, the initial conditions are approximately reproducible, so that the time evolution of a flow can be studied.

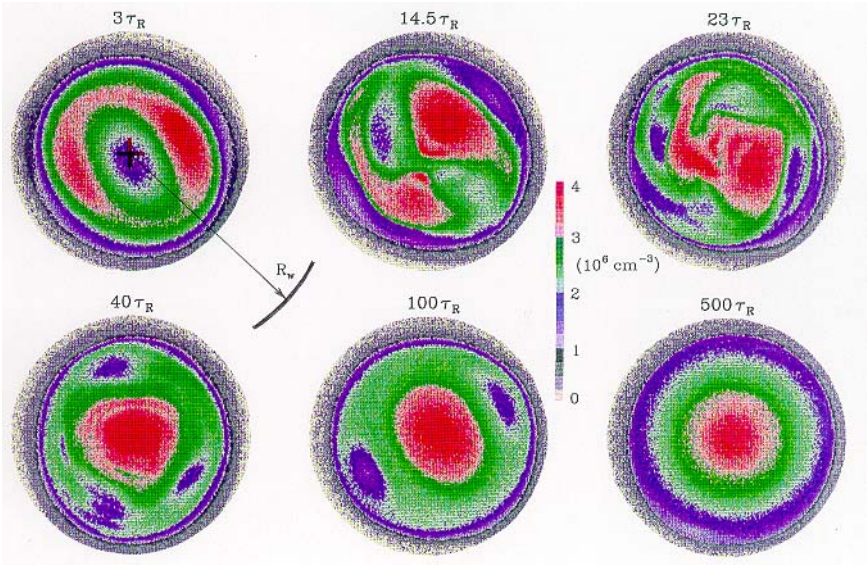

Figure 1.3: The instability and subsequent relaxation of a 2D vorticity (density) distribution [10]. The time scale for relaxation is determined by the rate at which 2 holes drift out of the distribution. $\tau_R \equiv 10\mu sec$.

1.2 Vortex Motion Driven by a Background Vorticity Gradient

Chapter 2 of this thesis was motivated by the experiment that is shown in Fig. 1.3, taken directly from Huang, Fine and Driscoll [10]. This experiment starts with an unstable vorticity distribution. After about $50\tau_R$ ($500\mu sec$), the flow settles into a quasi-stationary state, where there are two symmetrically placed holes (vorticity deficits) in an approximately circular background. These holes are sufficiently deep so that they are "self-trapped", and are not destroyed by the background shear.

The continued relaxation of the flow is controlled by the slow drift of the holes toward the edge of the background, where they are eventually sheared apart. Figure 1.4 shows the radial position r_h of the holes as a function of time [10]. The large scatter in the data is due to the destructive imaging technique. Each

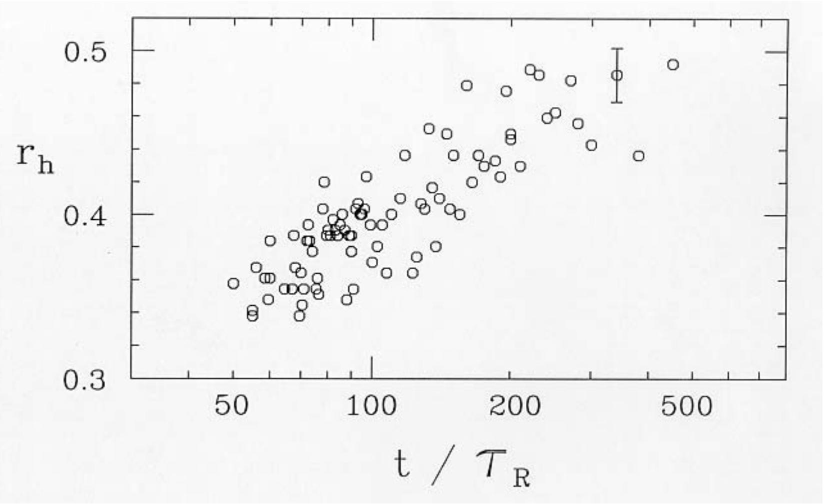

Figure 1.4: Hole radius r_h as a function of time [10]. Here, r_h is measured in units of $R_w = 3.2cm$.

datum corresponds to a separate evolution, with initial conditions that are slightly different than all others. We believe that the slow drift of holes toward the edge of the background is caused by the negative radial derivative of the background vorticity distribution. Similar motion of holes down vorticity gradients has been observed in numerical simulations (e.g. Ref. [12]).

The slow radial drift of vorticity holes that is observed in the electron plasma experiment has several close analogies. For example, hurricane trajectories are influenced by vorticity gradients in the background winds, and the north-south gradient in the Coriolis parameter, which can be thought of as a (potential) vorticity gradient [13-30]. In rotating tank experiments, vortices move up and down gradients in fluid depth, which play the same role as gradients in the Coriolis parameter [31, 32].

In Chapter 2 we examine the motion of both clumps (vorticity excesses) and holes in a monotonic background, similar to the experimental distribution. We calculate the rate at which clumps and holes ascend or descend a background vorticity gradient under the conditions that (i) the vortices are point-like and (ii) the background flow has strong shear.

Both clumps and holes act to level the local background vorticity gradient. However, this mixing affects clumps and holes oppositely: clumps move up the gradient, whereas holes move down the gradient [12, 13]. Eventually clumps settle on peaks of background vorticity, whereas holes settle in troughs. We will show that the opposite motion of clumps and holes is a consequence of momentum conservation.

The speed at which a vortex propagates along the gradient is different for prograde and retrograde vortices. By definition, a prograde vortex rotates with the local shear, and a retrograde vortex rotates against the local shear. We show that a linear analysis of the background vorticity evolution gives the motion of a weak retrograde vortex. For prograde vortices, like the holes in Fig. 1.3, the background evolution is always nonlinear, and the vortices move at a slower rate. This rate can be obtained from a simple “mix-and-move” estimate.

A very strong background shear can arrest the propagation of a vortex along a background vorticity gradient. For both prograde and retrograde vortices, we examine the critical shear level that is required to suppress gradient-driven motion. We find that the critical shear is much lower for a prograde vortex than it is for a retrograde vortex.

We note that the theory of vortex motion on a background vorticity gradient is similar to the clump-hole theory of plasma turbulence that was pioneered by Dupree [33, 34, 35, 36, 37, 38]. Here, a clump is an excess of ion (or electron) phase-space density, and a hole is a deficit of the same quantity. Plasma instabilities are associated with the motion of clumps and holes along gradients in phase-space density. Although the physics of phase-space clumps and holes differs from vortex motion in a 2D Euler fluid, many of the same techniques can be used to analyze

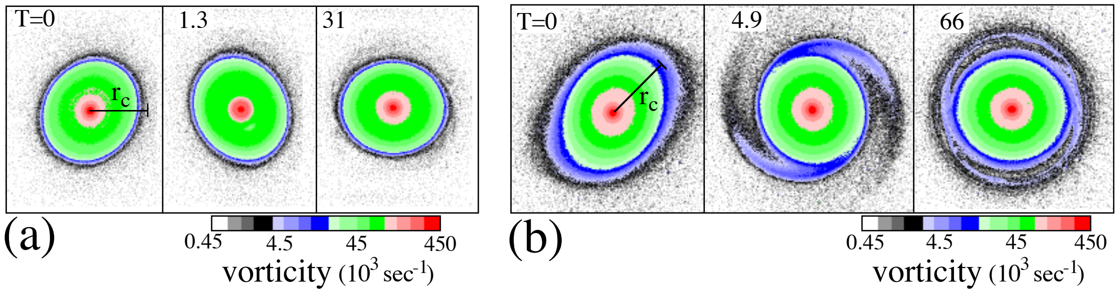

Figure 1.5: Experiments on inviscid damping. **(a)** An elliptical perturbation (mode) that persists. **(b)** An elliptical perturbation that decays through filamentation at r_c. Time T is measured in central rotation periods.

both problems.

1.3 Inviscid Damping

Chapter 3 of this thesis was motivated by the experiments that are shown in Fig. 1.5 [11]. Both experiments show the evolution of a monotonic vortex after an impulse deforms it into an ellipse. In experiment (a), the impulse excites an undamped elliptical mode, which persists for thousands of rotation periods, until dissipated by nonideal effects. In experiment (b), the elliptical vortex relaxes toward an axisymmetric state. During the relaxation, filaments are shed at a critical radius r_c, and vorticity contours become circular in the core of the vortex. We refer to this decay process as “inviscid damping”. Similar relaxation has been observed in numerical simulations, starting with the seminal work of Melander, McWilliams and Zabusky [39, 40, 41, 42].

One notable feature of inviscid damping is that the ellipticity decays at a rate that is approximately exponential [11, 43]. This experimental result is significant, since arbitrary perturbations need not decay exponentially.

In Chapter 3, we will show that the early evolution of the experimental vortices is well described by the linearized Euler equations. These equations are solved by expanding the perturbation into a sum of eigenmodes [44, 45, 46, 47]. We demonstrate that the eigenmodes of a monotonic vortex are neutrally stable, and form an orthogonal basis. Next, we derive a general formula for the response of each eigenmode to a brief perturbation in the flow field. We then study how the total excitation relaxes through the interference, or "phase-mixing" of these modes.

We first examine the evolution of initial conditions that are created by an impulsive flow field, applied by sources outside the vortex. These perturbations are of the same type that were studied experimentally. We find in general that the quadrupole moments (ellipticity) of these perturbations have an early stage of exponential decay, in accord with the experiments. Furthermore, we show that the decay rate is given a "Landau pole" of the equilibrium vortex [48, 49, 50].

Next, we turn our attention from the quadrupole moment to the vorticity perturbation $\Delta\zeta$. When the damping is light, we find that the vorticity perturbation (in addition to the quadrupole moment) decays exponentially with time for all radii less than a critical radius r_c, where filamentation occurs. That is, the vorticity perturbation acts like an exponentially damped eigenmode: $\Delta\zeta(\vec{r},t) \approx \xi(r)e^{-\gamma t}cos(2\theta - \omega_q t)$ for $r \lesssim r_c$. The critical radius r_c occurs where the fluid rotation frequency $\Omega_o(r)$ is resonant with the perturbation, and satisfies the equation $2\Omega_o(r_c) = \omega_q$.

These weakly damped vorticity perturbations are referred to as "quasi-modes", since they are not exact eigenmodes of the linearized Euler equations. We will show that a quasi-mode is a wave-packet of neutral eigenmodes, which occupy a narrow frequency band. Exponential decay occurs due to interference of these neutrally stable modes. The decay rate is proportional to the band-width of the wave-packet. This band-width goes to zero as the vorticity gradient at r_c goes to zero. With zero band-width, the quasi-mode is actually a single undamped eigenmode. This is the case in experiment (a) of Fig. 1.5, where r_c is outside the vortex.

We will show that quasi-modes (and discrete modes) dominate the experimental excitations because the eigenmodes in the wave-packet have exceptionally large multipole (quadrupole) moments. A large multipole moment implies that the eigenmode has a strong influence on the external flow. By reciprocity, the eigenmode couples strongly to flow fields that are applied from outside the vortex, like those which create the experimental perturbations. Eigenmodes which do not belong to the quasi-mode wave-packet tend to be self-shielding. Therefore, these eigenmodes couple weakly to externally applied flow fields.

We also analyze the case of strong damping, using a Gaussian vortex as an example. Here, we find that the narrow wave-packet occurring in weakly damped quasi-modes is replaced by a broad band wave-packet. We show that this broad band excitation corresponds to a vorticity perturbation that filaments over the entire vortex, rather than in a thin critical layer.

To conclude this section, we mention that inviscid damping in 2D hydrodynamics is analogous to Landau damping (collisionless damping) in plasma physics [48, 51, 52, 53, 54, 55, 56, 57]. Landau damping usually refers to the decay of compressional plasma waves due to their interaction with co-moving charged particles. Here, vorticity waves decay due their interaction with co-moving vorticity elements. In addition to the physical analogy between inviscid damping and Landau damping, there is also a close mathematical analogy. Thus, the term "Landau damping" is sometimes used in place of "inviscid damping" [48].

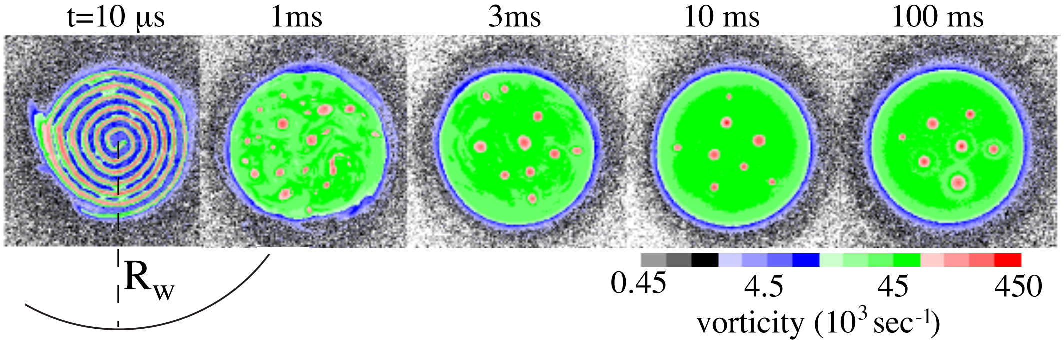

Figure 1.6: Observed formation of a vortex crystal.

1.4 The Formation of Vortex Crystals

Chapter 4 of this thesis was motivated by experiments of the kind that are shown in Fig. 1.6, which is taken directly from Fine et al [9]. This experiment starts with a spiral vorticity distribution, that rapidly generates a "soup" of intense vortices. These vortices chaotically advect, merge and shed filaments that stretch and mix to form a diffuse background. Eventually the chaotic motion of intense vortices "cools", mergers stop and the intense vortices tend to a pattern in rigid rotation (far right of Fig. 1.6). We refer to these patterns as vortex crystals.

The main point of Chapter 4 is to demonstrate that the formation of vortex crystals observed experimentally can be explained without incorporating physics beyond the 2D Euler equations. To this end, we compare the experiments directly to vortex-in-cell (VIC) simulations that numerically integrate the 2D Euler equations [58, 59]. The experiments and simulations are shown to relax at the same rates to vortex crystals with similar vorticity distributions. Close agreement between experiment and simulation provides strong evidence that 2D Euler theory alone can explain the formation of vortex crystals.

The formation of vortex crystals underscores the importance of understanding the dynamics of inviscid relaxation. Vortex crystals can not be explained with standard variational techniques that are sometimes used to predict final states of the relaxation. These include global maximum entropy postulates [61-72], and global minimum enstrophy postulates [61, 73, 74, 75]. Both theories, in their various forms, predict slowly varying distributions that fill the confinement region, not arrays of small intense vortices that survive the stage of vortex mergers.

It was proposed recently that the arrest of vortex mergers and the subsequent formation of vortex crystals is due to the ergodic mixing of the diffuse background by the intense vortices [60]. This hypothesis was justified by showing that the final states in the experiments are states that maximize the fluid entropy of the background, given the number of vortices and the energy, angular momentum, and total circulation of the flow. In Chapter 4, we further demonstrate that chaotic vortex motion is cooled through mixing of background vorticity. For example, we show that when the background vorticity is artificially removed from the simulations, there is no vortex cooling.

1.5 Other Processes

There are several mechanisms of inviscid relaxation that we do not directly address in this thesis, and which deserve some mention. One is vortex merger [76, 77, 78, 79]. Vortex merger is the process whereby vortices of the same sign attract one another and coalesce. Vortex merger is one mechanism for the "inverse cascade" of energy from small scales to large scales in 2D flows [80]. Through vortex merger, energy contained in the motion of many small-scale vortices is transferred to the flow in and around a few large-scale vortices.

The processes that we do examine are related to vortex merger in that they too effect the inverse cascade. In particular, consider the result of vortex motion that is driven by a background vorticity gradient. Positive vortices are driven toward background vorticity peaks, and negative vortices are driven toward background vorticity depressions (Fig. 1.3). Just as in vortex merger, positive vorticity tends to clump together, as does negative vorticity.

Inviscid damping also demonstrates the inverse cascade, in a less dramatic fashion. Through inviscid damping, asymmetrical perturbations on an extended vortex decay. For example, an elliptical vortex may become circular (Fig. 1.5.b). Thus, energy is transferred from high azimuthal wave-numbers (small scales) to low azimuthal wave-numbers (large scales).

Another process that we do not directly address is filamentation [81, 82]. Fine vorticity filaments are shed by vortices during their motion, especially during close-encounters (or mergers) with other vortices. The stretching and mixing of these filaments to form a diffuse background is a manifestation of the "forward cascade" of enstrophy (mean square vorticity) from large scales to small scales [83].

Of course, the background that is created by filamentation (or by external means) is central to the dynamics that we investigate in this thesis. This background profoundly affects vortex motion. We just mentioned how positive and negative vortices segregate due to the presence of a background vorticity gradient. However, the most stunning effect of background vorticity is that it can cool a system of chaotic vortices into a vortex crystal equilibrium.

Chapter 2

Vortex Motion Driven by a Background Vorticity Gradient

2.1 Introduction

The interaction of self-trapped vortices with a background vorticity gradient often plays an important role in 2D hydrodynamics. The interaction can cause the vortices to move transverse to the direction of the background flow, either up or down the vorticity gradient. Experiments with magnetized electron columns (Fig. 1.3) have shown how this transverse motion can set the time scale for the relaxation of 2D turbulence [10]. Hurricane motion is also influenced by gradients in the background vorticity. This includes the north-south variation in the Coriolis parameter, which can be thought of as a (potential) vorticity gradient [13].

The prediction of hurricane tracks is a problem of great practical importance, so it is hardly surprising that a considerable body of theoretical work has been devoted to the subject [13-32]. Here, we consider the motion of vortices on a background vorticity gradient in the regime where (i) the vortices are point-like, and (ii) the background flow has strong shear. Perhaps because this regime is not of direct application to the motion of tropical cyclones, the results described in this chapter have not been discussed previously (to our knowledge). Nevertheless, while point-like vortices and strong background shear may be rare in geophysical settings, they are common in nonneutral plasmas [9, 10] and may also be found on planets like Jupiter that have intense storms in strong zonal winds [84].

Self-trapped vortices can be classified as either prograde or retrograde. A prograde vortex rotates with the local background shear, while rotation in the opposite sense defines retrograde vortices. We find that a linear analysis of the background vorticity evolution gives the motion of a sufficiently weak retrograde vortex. For prograde vortices of any intensity, the background evolution is always nonlinear, and the vortices move at a slower rate. This rate is given by a simple "mix-and-move" estimate.

When the background shear is sufficiently large compared to the background vorticity gradient, prograde vortices no longer move across the flow. Instead, they flatten the local vorticity gradient and come to an equilibrium with the background. Retrograde vortices can also equilibrate with the background, but an even larger shear is required, since they tend to move faster than prograde vortices. Theoretical estimates for the size of the shear required for equilibration in both cases are derived, and are found to compare favorably to simulations that demonstrate this equilibration.

The theory and simulations presented in this chapter focus on incompressible 2D flows for which viscosity can be neglected. Such flows are governed by the 2D Euler equations:

$$\frac{\partial \zeta}{\partial t} + \vec{v} \cdot \nabla \zeta = 0, \qquad \vec{v} = \hat{z} \times \nabla \psi, \qquad \nabla^2 \psi = \zeta. \tag{2.1}$$

Here, $\vec{v}(r, \theta, t)$ is the velocity field, $\zeta(r, \theta, t) \equiv \hat{z} \cdot \nabla \times \vec{v}$ is vorticity and $\psi(r, \theta, t)$ is a stream function. The coordinates (r, θ) denote polar radius and angle, and t is time. For analysis, the vorticity is decomposed into vortices (v) and background

(b): $\zeta = \zeta_b + \sum \zeta_v$.

The vortices can be classified as either clumps (regions of excess positive vorticity) or holes (regions of excess negative vorticity, or deficits of positive vorticity). This classification is in addition to their classification as either prograde or retrograde. Clumps can in general be prograde or retrograde, and the same is true for holes.

It is well known that clumps ascend a background vorticity gradient and that holes descend the gradient (see for example Refs. [12, 13]). Figure 2.1 illustrates this phenomenon for the case of circular geometry, point-like vortices and strong background shear. At $t = 0$, a clump (black spot) and a hole (white spot) are placed in a circular shear-flow. The system is evolved with a vortex-in-cell (VIC) simulation that numerically integrates the 2D Euler equations (see Chapter 4 for a description of the VIC simulation). Eventually, the clump is driven to the peak in background vorticity, whereas the hole is driven toward the minimum.

Figure 2.2 shows the gradient-driven separation of a clump and hole in straight zonal flow. The flow is evolved using a VIC simulation in a periodic box. As before (Fig. 2.1), the clump migrates to the peak in background vorticity, whereas the hole migrates to the minimum. Thus, clumps and holes tend to opposite

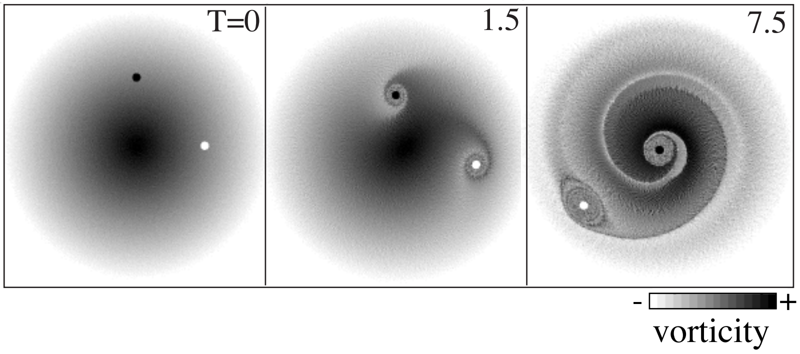

Figure 2.1: VIC simulation of the gradient-driven radial separation of a clump (black dot) and hole (white dot) in a circular shear flow [Eq. (2.29)].

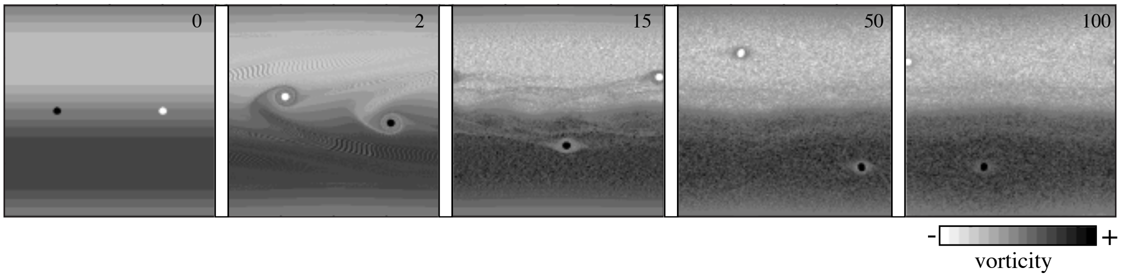

Figure 2.2: VIC simulation of the gradient-driven separation of a clump and hole in straight zonal flow. The numbers on each snap-shot indicate time.

extremes in the background vorticity, in both curved and uncurved geometry.

When the boundary conditions have rotational or translational symmetry, the opposite drifts of clumps and holes are easily explained using conservation of angular or linear momentum. Similar arguments have been used to explain the motion of phase-space density clumps and holes in plasma turbulence [36].

We first consider a small clump (Fig. 2.3.a) or hole (Fig. 2.3.b) in an axisymmetric background ζ_b that decreases slowly with r. The vortex will partially mix the background and move in response. If the fluid is contained by a cylindrical boundary, the motion is constrained by conservation of (canonical) angular momentum, P_θ.

It is convenient to write P_θ in terms of a background contribution and a vortex contribution,

$$P_\theta \equiv \int d^2r\, r^2 \zeta(r,\theta,t) = \Gamma_b \left\langle r^2 \right\rangle_b + \Gamma_v r_v^2. \tag{2.2}$$

Here $\Gamma_b > 0$ is the total circulation of the background flow, Γ_v is the vortex circulation, r_v is the radial position of the vortex and $\langle r^2 \rangle_b$ denotes the ζ_b-weighted spatial average of r^2. As shown in Fig. 2.3, local mixing increases $\langle r^2 \rangle_b$ by flattening the background (since $\zeta_b' < 0$). To conserve P_θ, the clump ($\Gamma_v > 0$) must decrease r_v and climb the background gradient, whereas the hole ($\Gamma_v < 0$) must increase r_v and descend the gradient, as observed in Fig. 2.1.

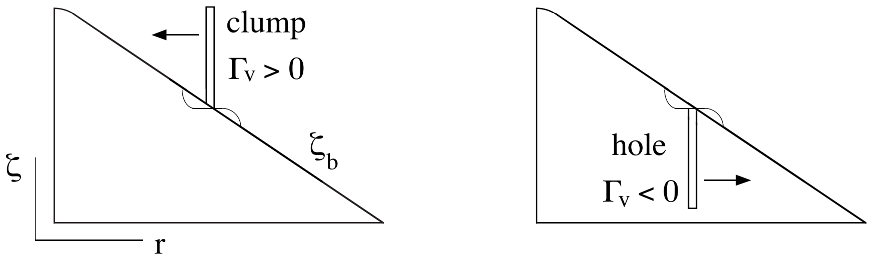

Figure 2.3: Local mixing of the background increases $\langle r^2 \rangle_b$. By conservation of P_θ, clumps and holes react oppositely.

If the fluid is bounded by parallel walls at $y = \pm Y$, the 2D Euler equations conserve P_x, the canonical linear momentum:

$$P_x \equiv \int d^2x \; y\zeta(x, y, t) = \Gamma_b \langle y \rangle_b + \Gamma_v y_v. \tag{2.3}$$

Here (x, y) is a rectangular coordinate system in the plane of the flow. The motion of a vortex along the y-gradient in ζ_b can be explained by conservation of P_x, just as motion along the radial gradient was explained by conservation of P_θ in cylindrical flow. If $\zeta_b'(y) < 0$, local mixing increases $\langle y \rangle_b$. By conservation of P_x a clump must climb the gradient and decrease y_v, whereas a hole must descend the gradient and increase y_v.

When there is no local vorticity gradient, local mixing does not affect the background vorticity distribution. Therefore, where $\zeta_b' = 0$, there is no local mechanism for the vortex to exchange angular or linear momentum with the background. This suggest that clumps will settle on hills of background vorticity and that holes will settle in troughs, where $\zeta_b' = 0$. This relaxation principle is consistent with Fig. 2.1 and Fig. 2.2.

In this introduction, we have demonstrated that the opposite drifts of clumps and holes along vorticity gradients is an important principle of organization in 2D flows at high (infinite) Reynolds numbers. In the remainder of this paper, we calculate the time scale for this organization to occur; i.e. the rate at which clumps climb vorticity gradients and the rate at which holes descend vorticity gradients. We consider the specific case of a single small vortex in a circular shear-flow, where the initial background vorticity is positive, axisymmetric and decreases monotonically with radius r. In this background a clump is retrograde and a hole is prograde.

In Section 2.2, we present a simple linear calculation of vortex motion that is driven by a background vorticity gradient. A more detailed linear theory is presented in Section 2.3. In Section 2.4, we compare linear theory to a nonlinear VIC simulation. We find that linear theory works well only for retrograde vortices, and fails for prograde vortices. In Section 2.5, we discuss why linear theory fails for prograde vortices. In Section 2.6, we derive a simple mix-and-move estimate for the motion of prograde vortices. In Section 2.7, we discuss how gradient-driven vortex motion is suppressed when the background shear is sufficiently large. In Section 2.8, we discuss gradient-driven vortex motion as a mechanism of self-organization in natural flows. Many intermediate results are derived in the appendices.

2.2 Simple Calculation of Gradient-Driven Drift

We now determine the radial speed of the vortex, making a few reasonable assumptions that reduce the math. A more detailed analysis is presented in Section 2.3.

The vortex's dominant translational motion is rotation about the center of the background. We work in this rotating frame, so the vortex is nearly stationary, and we define a local (x, y) coordinate system centered at the vortex. In these coordinates, the initial velocity due to the background is $\vec{v} = Ay\hat{x}$ near the vortex, where A is the shear. The initial background vorticity gradient is $\zeta_o'\hat{y}$ (where $\hat{y}$

points in the local r-direction).

Figure 2.4 shows the initial stream lines in the vicinity of a retrograde clump (a) and a prograde hole (b). The stagnation points in Fig. 2.4.a are at a distance l above and below the clump, where

$$l \equiv \sqrt{|\Gamma_v/2\pi A|}. \tag{2.4}$$

We treat the vortex and the disturbance that it generates as perturbations to the initial shear-flow, and suppose that the Euler equation for the evolution of ζ_b can be linearized,

$$\left[\frac{\partial}{\partial t} + Ay\frac{\partial}{\partial x}\right] \cdot \delta\zeta_b = -\zeta_o' \frac{\Gamma_v}{2\pi} \frac{x}{x^2+y^2}. \tag{2.5}$$

Here, $\delta\zeta_b(x, y, t)$ is the background vorticity perturbation, and we have used $\zeta_v = \Gamma_v\delta(\vec{x})$. This assumes that the vortex is point-like and moves slowly compared to the evolution of the background. We have also neglected the velocity perturbation due to $\delta\zeta_b$, assuming that it is negligible compared to the vortex velocity field.

Equation (2.5) can be solved by the method of characteristics, yielding

$$\delta\zeta_b = \frac{-\Gamma_v}{4\pi} \frac{\zeta_o'}{Ay} ln \left[\frac{x^2+y^2}{(x-Ayt)^2+y^2}\right]. \tag{2.6}$$

The radial velocity ($\dot{r}_v$) of the vortex is the y-component of the velocity perturbation that develops at the origin. By summing the contributions to the velocity field

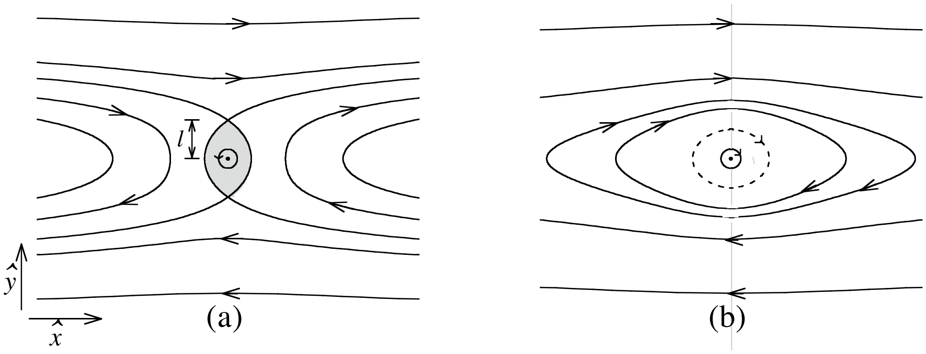

Figure 2.4: Initial stream lines for a retrograde clump (a) and a prograde hole (b) in a shear flow $\vec{v} = Ay\hat{x}$, $A > 0$.

from each background vorticity element, we obtain the following integral expression for $\dot{r}_v$ (here, $u \equiv x/y$) :

$$\dot{r}_v = \frac{\Gamma_v}{4\pi^2}\frac{\zeta_o'}{A}\int_l^L \frac{dy}{y}\int_{-\infty}^{+\infty} du \frac{u}{u^2+1} ln\left[\frac{u^2+1}{(u-At)^2+1}\right] \tag{2.7}$$

A small scale (l) and a large scale (L) cut-off are introduced to escape infinities in the y-integral. The small scale cut-off describes the minimum distance from the vortex at which nonlinearities in the background flow can be ignored. Thus, we identify the small scale cut-off with l [Eq. (2.4)], the size of the shaded trapping region in Fig. 2.4.a. To determine the upper cut-off, we note that curvature in the unperturbed flow can not be ignored for $|y| \gtrsim r_v$, where r_v is the radial position of the vortex. We therefore set $L = c \cdot r_v$, where c is presumably $O(1)$.

The integrals in Eq. (2.7) yield

$$\begin{aligned} \dot{r_v} = & \quad \frac{\Gamma_v}{2\pi}\frac{\zeta_o'}{|A|} ln(L/l) \cdot tan^{-1}(T/2) \\ = & \quad \pm\zeta_o' \, l^2 \, ln\,(c \cdot r_v/l) \cdot tan^{-1}(T/2), \end{aligned} \tag{2.8}$$

where $T \equiv |A|t$ and +/- is for clumps/holes. The u-integral, which gives the time-dependence, is evaluated in Appendix I. For $T >> 1$, the inverse-tangent is approximately $\pi/2$ and $\dot{r}_v$ is approximately constant.

Equation (2.8) gives a reasonable scaling for the vortex speed: $\dot{r}_v$ increases with Γ_v and ζ_o', while it decreases as the local shear A intensifies. However, the validity of Eq. (2.8) rests on the accuracy of Eq. (2.5), which neglects curvature in the unperturbed flow, the velocity perturbation due to $\delta\zeta_b$, motion of the vortex, and all nonlinear terms. We soon test Eq. (2.8) against a VIC simulation that keeps all of these effects; but first, we carry out a more detailed linear calculation for $\dot{r}_v$ that keeps stream-line curvature and the velocity perturbation due to $\delta\zeta_b$. This calculation reproduces Eq. (2.8) and gives a precise value for c, which appears in the logarithm.

Before moving on to a more detailed analysis in cylindrical geometry, we note that Eq. (2.8) also applies to gradient-driven drift in straight channel flow. If the background vorticity gradient is in the y-direction, then $\dot{y}_v$ replaces $\dot{r}_v$. The only difference appears in the logarithm. In straight channel flow, the upper cut-off L is presumably the width of the channel, or the length scale for variations in background vorticity.

2.3 Formal Linear Theory of Gradient-Driven Drift

This section contains a formal linear theory for the gradient-driven radial drift of a point-vortex in cylindrical shear flow.

To begin with, we break the background vorticity distribution into two parts:

$$\zeta_b(r,\theta,t) = \zeta_o(r) + \delta\zeta_b(r,\theta,t). \tag{2.9}$$

Here, ζ_o is the initial axisymmetric distribution, and $\delta\zeta_b$ is the disturbance that is created by the vortex. Furthermore, we break the total stream function into two parts:

$$\psi(r,\theta,t) = -\int_r^{R_w} dr' r' \Omega_o(r') + \delta\psi(r,\theta,t). \tag{2.10}$$

Here, $\Omega_o(r)$ is the initial rotation frequency of the background. The perturbation $\delta\psi$ consists of a background contribution ($\delta\psi_b$) and a vortex contribution ($\delta\psi_v$): $\delta\psi = \delta\psi_b + \delta\psi_v$. Both of these components are defined below:

$$\nabla^2 \delta\psi_b = \delta\zeta_b \tag{2.11.a}$$

$$\nabla^2 \delta\psi_v = \Gamma_v \frac{\delta(r - r_v)\delta(\theta - \theta_v)}{r_v} \tag{2.11.b}$$

The boundary conditions are $\delta\psi_b, \delta\psi_v = 0$ at the wall radius R_w.

Next, we introduce the dimensionless parameter

$$l/r_v = \frac{1}{r_v}\sqrt{\left|\frac{\Gamma_v}{2\pi\Omega_o'(r_v)r_v}\right|}, \tag{2.12}$$

which is the trapping length [Eq. (2.4)] normalized to the orbital radius of the vortex. The value of l/r_v is a measure of vortex strength to shear strength. We assume that the vortex is weak, or precisely that $l/r_v << 1$. We further assume that this condition permits us to linearize the Euler equation for the evolution of the background vorticity perturbation. That is, we take the following equation for the evolution of $\delta\zeta_b$:

$$\frac{\partial\delta\zeta_b}{\partial t} + \Omega_o(r)\frac{\partial\delta\zeta_b}{\partial\theta} - \frac{1}{r}\zeta_o'(r)\frac{\partial\delta\psi}{\partial\theta} = 0. \tag{2.13}$$

In contrast to the simple theory of gradient-driven vortex motion [Eq. (2.5)], stream-line curvature is kept in Eq. (2.13) by use of polar coordinates. The background stream function $\delta\psi_b$ is also kept, since $\delta\psi = \delta\psi_b + \delta\psi_v$.

It is convenient to expand the perturbation, using a Fourier series in the polar-angle θ:

$$\begin{bmatrix} \delta\psi \\ \\ \delta\zeta_b \end{bmatrix} = \sum_{m=-\infty}^{\infty} e^{im\theta} \begin{bmatrix} \Psi^{(m)}(r,t) \\ \\ Z^{(m)}(r,t) \end{bmatrix}. \tag{2.14}$$

Substituting Eq. (2.14) into Eq. (2.13), it is found that each Fourier coefficient of the vorticity perturbation evolves independently, according to

$$\left[\frac{\partial}{\partial t} + im\Omega_o(r)\right] \cdot Z = im\frac{\zeta_o'(r)}{r}\Psi. \tag{2.15}$$

Here, we have suppressed the superscript '(m)' on Z and Ψ. This will be standard, unless it would lead to ambiguity.

The background perturbation causes the vortex to leave its initial circular orbit. Specifically, the vortex moves radially according to $\dot{r}_v = -\frac{1}{r_v}\frac{\partial\delta\psi}{\partial\theta}\bigg|_{\vec{r}_v}$, which can be written

$$\dot{r}_v = \frac{2}{r_v} \sum_{m=1}^{\infty} m \cdot Im \left[\Psi^{(m)}(r_v, t) e^{im\theta_v} \right]. \tag{2.16}$$

Here, Im stands for the imaginary part of the quantity in brackets. The angular velocity of the vortex $\dot{\theta}_v$ is dominated by the unperturbed background rotation. So, we use the following approximation:

$$\dot{\theta}_v = \Omega_o(r_v). \tag{2.17}$$

The value of $\dot{r}_v$ is now calculated, using an unperturbed orbit approximation. In this approximation, the background perturbation is evolved with the vortex moving along a fixed circular orbit, and $\dot{r}_v$ is taken to be the radial velocity perturbation that develops at $\vec{r}_v$. The unperturbed orbit approximation is justified, assuming that $\dot{r}_v$ asymptotes to a fixed value rapidly compared to vortex motion through the background. The vortex then drifts radially with the asymptotic speed. Of course, the asymptotic speed changes parametrically with the radial position r_v of the vortex.

According to Eq. (2.16), to calculate $\dot{r}_v$, we must calculate the Fourier coefficients $\left\{ \Psi^{(m)} \right\}$ of the stream function. Let $\tilde{Z}(r,s)$ and $\tilde{\Psi}(r,s)$ denote the temporal Laplace transforms of $Z(r,t)$ and $\Psi(r,t)$. Here, s is the Laplace transform variable. From Eq. (2.15), we have

$$\left[s + im\Omega_o(r) \right] \tilde{Z} = im \frac{\zeta_o'(r)}{r} \tilde{\Psi}. \tag{2.18}$$

From Eq. (2.11),

$$\left(\frac{d^2}{dr^2} + \frac{1}{r}\frac{d}{dr} - \frac{m^2}{r^2} \right) \tilde{\Psi} = \tilde{Z} + \frac{\Gamma_v}{2\pi s} \frac{\delta(r - r_v)}{r}. \tag{2.19}$$

Note that Eq. (2.19) is written in a frame that rotates with the the orbital frequency of the vortex. In this frame, $\dot{\theta}_v = \Omega_o(r_v) = 0$. We have also set θ_v equal to zero.

Combining Eq. (2.18) with Eq. (2.19), we obtain the following equation for $\tilde{\Psi}(r,s)$:

$$\tilde{\Psi}(r,s) \equiv \frac{\Gamma_v}{2\pi s} G(r|r_v,s). \tag{2.20}$$

Here, G is the Green's function of the differential operator D_s,

$$D_s\left[G(r|r_v,s)\right] = \frac{\delta(r-r_v)}{r}, \tag{2.21}$$

and D_s is defined by the equation

$$D_s \equiv \frac{\partial^2}{\partial r^2} + \frac{1}{r}\frac{\partial}{\partial r} - \frac{m^2}{r^2} - \frac{im\zeta_o'(r)}{r[s+im\Omega_o(r)]}. \tag{2.22}$$

To obtain $\Psi(r,t)$, we must invert the Laplace transform. This yields the following integral expression for $\Psi(r,t)$:

$$\Psi(r,t) = \frac{\Gamma_v}{4\pi^2 i}\int_{\alpha-i\infty}^{\alpha+i\infty} ds \frac{G(r|r_v,s)}{s} e^{st}. \tag{2.23}$$

The integral in Eq. (2.23) is along the vertical line $s \equiv \alpha + i\omega$ in the complex plane, where α is positive and $-\infty < \omega < \infty$.

Following standard procedure, we neglect any poles of $G(r|r_v,s)$ that might exist in the right half of the complex s-plane (including the imaginary axis). We then use the Plemelj formula to obtain the following limit of Eq. (2.23) as $\alpha \to 0^+$:

$$\Psi(r,t) = \frac{\Gamma_v}{4\pi^2 i}\left\{P\int_{-\infty}^{\infty} d\omega \frac{G(r|r_v,0^+ + i\omega)}{\omega} e^{i\omega t} + i\pi G(r|r_v,0^+)\right\}. \tag{2.24}$$

Here, P denotes the "principal part" of the integral, which has a singular integrand at $\omega = 0$.

From our simple calculation [Eq. (2.8)], we found that $\dot{r}_v$ rapidly asymptotes to a constant value. We assume that the same is true here, and concern ourselves only with this time-asymptotic limit. In Appendix IV, we show that the time-asymptotic limit of the integral in Eq. (2.24) is $i\pi G(r|r_v,0^+)$. Therefore,

$$\begin{matrix} lim \\ t\to\infty \end{matrix}\; Im\left[\Psi(r,t)\right] = \frac{\Gamma_v}{2\pi} Im\left[G(r|r_v,0^+)\right] \tag{2.25}$$

Substituting Eq. (2.25) into Eq. (2.16), we find that the time-asymptotic value of the radial drift is given by the following equation:

$$\begin{aligned} \lim_{t \to \infty} \dot{r}_v &= \frac{\Gamma_v}{\pi r_v} \sum_{m=1}^{\sqrt{e} r_v / l} m \cdot Im \left[G^{(m)}(r_v | r_v, 0^+) \right] \\ &= \pm 2 |\Omega_o'(r_v)| l^2 \sum_{m=1}^{\sqrt{e} r_v / l} m \cdot Im \left[G^{(m)}(r_v | r_v, 0^+) \right], \end{aligned} \tag{2.26}$$

where +/− is for clumps/holes.

In Eq. (2.26), we have truncated the series at $m = \sqrt{e} r_v / l$. This cut-off is the inverse of the horizontal width (in radians) of the small trapping region (TR) around a retrograde clump, which is shaded in Fig. 2.4.a. Neglecting $m > \sqrt{e} r_v / l$ amounts to neglecting the contribution to $\dot{r}_v$ from the TR, where the linear equations are not valid, and the fluid is rapidly ($T \lesssim 1$) mixed by the vortex. Although the TR is defined only for a retrograde vortex, we try the same cut-off for a prograde vortex.

For small m, the Green's function $G(r | r_v, 0^+)$ must (in general) be found numerically. Our method for this computation is given in Appendix II. However, for large m, the imaginary part of the Green's function can be calculated analytically. From this analytic calculation, we obtain

$$Im \left[G(r_v | r_v, 0^+) \right] \rightarrow \frac{\pi \zeta_o'(r_v)}{4 m^2 |\Omega_o'(r_v)|}, \quad m >> 1. \tag{2.27}$$

Equation (2.27) is derived in Appendix III.

Because of Eq. (2.27), the sum in Eq. (2.26) diverges logarithmically as the m-number cut-off goes to infinity; i.e., as $l / r_v \rightarrow 0$. Thus, for sufficiently weak vortices, the time asymptotic radial drift is approximately given by

$$\dot{r}_v = \pm \frac{\pi}{2} \zeta_o'(r_v) \, l^2 \, ln \left(c \cdot r_v / l \right). \tag{2.28}$$

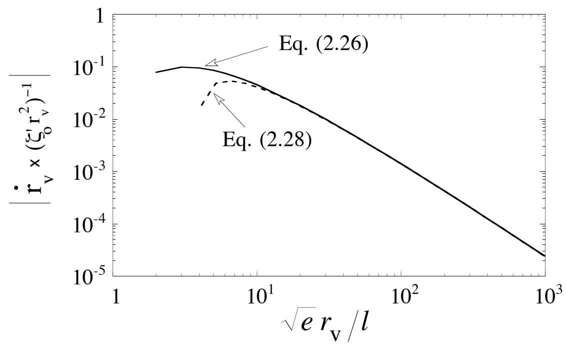

Figure 2.5: Comparison of Eq. (2.26) for $\dot{r}_v$ to the large $\sqrt{e}\, r_v/l$ approximation, Eq. (2.28).

Here, $+/-$ is for clumps/holes, and c is determined by the low-m values of the Green's function $G^{(m)}(r_v|r_v, 0^+)$. Note that Eq. (2.28) is equivalent to the $T \to \infty$ limit of our back-of-the-envelope calculation, Eq. (2.8). Therefore, the effects of $\delta\psi_b$ and curvature in the continuity equation [which we neglected in deriving Eq. (2.8)] are not important, provided that l/r_v is sufficiently small.

In practice, we obtain the value of c by setting Eq. (2.28) equal to a numerical solution of Eq. (2.26) for any large value of the m-number cut-off, $\sqrt{e}\, r_v/l$. The resulting equation is easily solved for c. As an example, we consider the radial velocity of a vortex at $r_v = 0.4$, in the background distribution of Eq. (2.29) (see next section). For this case, we obtain $c = 0.43$. In Fig. 2.5, we plot the time asymptotic value of $\dot{r}_v$, given by Eq. (2.26), versus $\sqrt{e} r_v/l$. Also in this figure, we plot the time asymptotic value of $\dot{r}_v$ that is given by Eq. (2.28), with $c = 0.43$. Clearly, Eq. (2.28) is an excellent approximation of $\dot{r}_v$ for all $l/r_v \lesssim 0.1$. Although c could in general depend on r_v, we find that for the vorticity profile of Eq. (2.29), the same $c = 0.43$ works for all $r_v \lesssim 0.7$.

The linear theory presented in this section neglects poles (in the s-plane) of the Green's function $G(r|r_v, s)$. This amounts to neglecting the excitation by the vortex of discrete modes in the background. In the next section we will show that neglecting the excitation of discrete modes is acceptable, for a case where the background vorticity varies slowly with radius. However, vortex-mode interactions may be important when there are large steps in the radial profile of the background [79].

2.4 The Success and Failure of Linear Theory

We now demonstrate that the linear equations of motion apply only to retrograde vortices, and that nonlinear effects must be kept to explain the slower drift of prograde vortices. We reach this conclusion by comparing a (nonlinear) VIC simulation[1] to a numerical integration of the linearized equations [Eqs. (2.15-2.17)].

In the linear simulation, the vortex position $\vec{r}_v$ and the Fourier coefficients $\left\{Z^{(m)}\right\}$ of the background vorticity are evolved forward in time with third-order Adams-Bashforth steps ($\sim 10^3$ steps per background rotation). The Fourier coefficients $\left\{\Psi^{(m)}\right\}$ of the stream function are each decomposed into a background contribution (Ψ_b) and a vortex contribution (Ψ_v): $\Psi = \Psi_b + \Psi_v$. Poisson's equation [the θ-Fourier transform of Eq. (2.11.a)] is solved for Ψ_b to second order accuracy in the radial grid-point spacing ($\sim R_w/2000$). For $m \leq \sqrt{e}\; r_v(t)/l(t)$, the vortex component of Ψ is given by

$$\Psi_v^{(m)}(r,t) = -\frac{\Gamma_v}{4\pi m}\left(\frac{r_<}{r_>}\right)^m \left[1 - \left(\frac{r_>}{R_w}\right)^{2m}\right] e^{-im\theta_v(t)},$$

where $r_>(r_<)$ is the greater (smaller) of r and $r_v(t)$. The number of (excited) Fourier components is made finite in the linear simulation by setting $\Psi_v^{(m)} = 0$ for $m > \sqrt{e}\; r_v(t)/l(t)$. With this scheme, the vortex never excites wave-numbers

---

[1] The VIC simulation is the same as that used in Chapter 4. Here, we use at most 1025×1025 gridpoints and 3×10^6 particles.

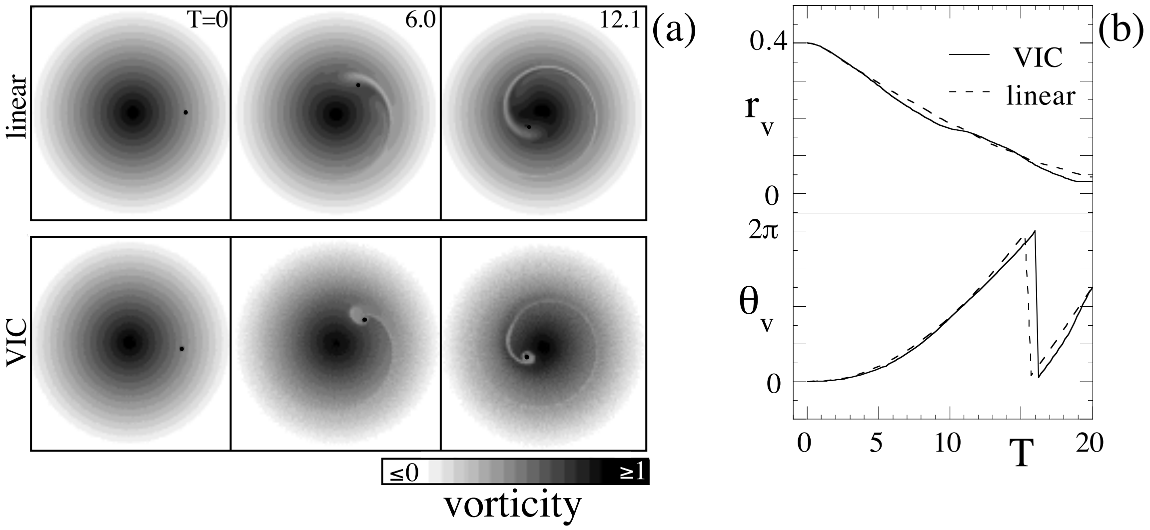

Figure 2.6: Inward spiral of a retrograde clump, computed with a linear simulation and a nonlinear VIC simulation: **(a)** sequence of contour plots, **(b)** (r_v, θ_v) vs. $T \equiv |\Omega_o'| r_v(0) t$.

greater than the maximum value of $\sqrt{e}\, r_v/l$ over the vortex trajectory. This cutoff was used (and explained) previously in deriving an analytic expression for the radial velocity of the vortex [Eq. (2.26)].

We consider the specific case where the initial background vorticity distribution (ζ_b at $t = 0$) is given by

$$\zeta_o(r) = \begin{cases} 1 - 1.25 \cdot r & r \leq 0.8 \\ 0 & r > 0.8. \end{cases} \tag{2.29}$$

The rotation frequency of this background is $\Omega_o(r) = 0.5 - 0.417 \cdot r$, for $r \leq 0.8$. The flow is bounded by a circular wall with radius $R_w = 1$, and there is free slip at this wall ($\psi = 0$ at R_w). The background chosen here represents a larger class, where the radial derivatives ζ_o' and Ω_o' vary slowly with r.

We first examine the motion of clumps, which are retrograde in this background. Figure 2.6 shows the inward spiral of a clump toward the center of the background. The clump strength l/r_v is initially 0.12.

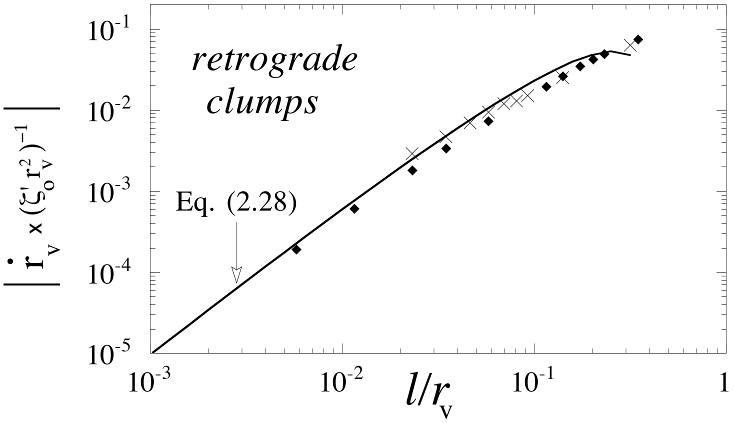

Figure 2.7: $\dot{r}_v$ vs. l/r_v for retrograde clumps in a linear simulation (diamonds) and a VIC simulation (X's). The solid line is the theory prediction of Eq. (2.28), with $c = 0.43$.

Figure 2.6.a shows a sequence of contour plots for both the linear simulation and the VIC simulation. Although the linear evolution is not identical to the VIC simulation, several features appear similar. These include the rate at which the clump travels toward the center of the distribution, and the wake that is left behind the clump.

Figure 2.6.b provides a more concise comparison of the clump trajectories. The top graph shows the linear (dashed line) and the VIC (solid line) computations of $r_v(t)$. There is good agreement between the linear and VIC results. The bottom graph shows that there is similar agreement for $\theta_v(t)$.

It is apparent from Fig. 2.6.b that the clump rapidly accelerates to an approximately constant radial speed. In Fig. 2.7, we plot the value of this speed as a function of the clump strength l/r_v. Here, all clumps start at $r_v = 0.4$ and the background is always given by Eq. (2.29). The clump strength l/r_v is varied by changing Γ_v only. The value of $\dot{r}_v$ is obtained from a straight-line fit to r_v vs. t, as r_v decreases from 0.375 to 0.35. In the plot, $\dot{r}_v$ is normalized to $\zeta_o' r_v^2$. Both $\zeta_o' r_v^2$ and the clump strength l/r_v are evaluated at $r_v = 0.363$. The diamonds correspond to linear simulations and each 'X' corresponds to a VIC simulation. The solid curve is Eq. (2.28), with $c = 0.43$.

Figure 2.7 presents several important results. To begin with, the VIC simulations generally agree with the linear simulations. This indicates that the linear equations [Eqs. (2.15-2.17)] are valid for retrograde vortices, when $l/r_v << 1$. Moreover, both simulations are well described by the analytic linear theory of Eq. (2.28), which relies on the unperturbed orbit approximation and neglects discrete modes of the background. The accuracy of Eq. (2.28) appears to improve as l/r_v approaches zero.

Good agreement between the simulations and our linear analysis [Eq. (2.28)] may seem surprising, especially because the analysis neglects the interaction of the vortex with the discrete normal modes of the background (i.e. the analysis neglects poles in the Green's function G). One can easily show that a vortex can not resonate with a discrete mode of a monotonic background, provided that the vortex is inside the background. For a discrete mode that varies like $e^{i(m\theta-\omega t)}$, the resonance condition is $m\Omega_o(r_v) = \omega$. That is, the vortex radius must equal the resonant radius of the mode. However, the resonant radius of a discrete mode can occur only where ζ_o' is zero, i.e. in a region outside the monotonic background [48]. Therefore, a vortex inside the background can not resonate with a discrete mode.

Nevertheless, discrete modes can still exist, and there is a question as to how much they influence the vortex motion. Figure 2.8 demonstrates explicitly that the effect of the discrete modes is negligible. Here, we plot the radial velocity perturbation that develops at $\vec{r}_v$ as a function of time, for a vortex that is fixed on its initial circular orbit. The vortex strength is $l/r_v = 0.03$, and the background is given by Eq. (2.29). To calculate $\dot{r}_v$, we used the linear simulation, but kept r_v artificially fixed at 0.4.

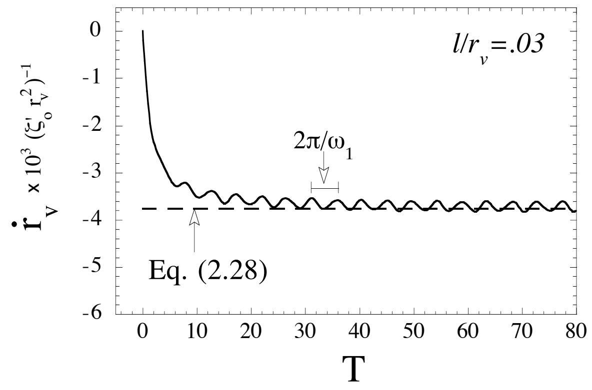

Figure 2.8: Radial velocity perturbation that develops at $\vec{r}_v$, for a clump fixed on its initial circular orbit. The solid line is a linear simulation, and the dashed line is the time-asymptotic theory neglecting discrete modes.

The value of $\dot{r}_v$ in Fig. 2.8 rapidly converges to Eq. (2.28), with $c = 0.43$. Therefore, in deriving Eq. (2.28), we were justified in neglecting the discrete modes. The only noticeable effect of these modes are small oscillations about the asymptotic value of $\dot{r}_v$. These oscillations have the same frequency as the $m = 1$ discrete mode, in a frame that rotates with the vortex. This frequency is given by the equation $\omega_1 = \Omega_o(R_w) - \Omega_o(r_v)$.

We now consider the motion of prograde holes. Figure 2.9 shows the outward spiral of a hole toward the edge of the background. As before, the background distribution is given by Eq. (2.29), and the initial vortex strength l/r_v is 0.12.

Figure 2.9.a shows a sequence of contour plots for both the linear simulation and the VIC simulation. In contrast to clump motion, here there is a dramatic difference between the linear simulation and the VIC simulation: the linear equations give a radial drift that is much too fast. Fig. 2.9.b shows $r_v(t)$ and $\theta_v(t)$ for both the linear (dashed line) and VIC (solid line) simulations. After $T \sim 1$ there is a sharp divergence between the linear and nonlinear trajectories. This rapid break-down of linear theory is explained in the next section.

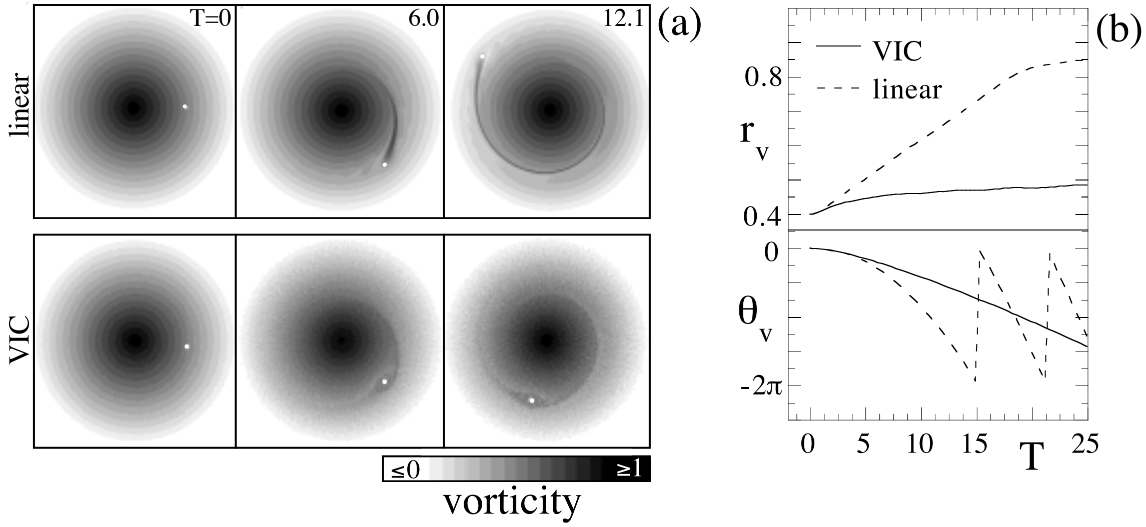

Figure 2.9: Outward spiral of a prograde hole, computed with a linear simulation and a nonlinear VIC simulation: (a) sequence of contour plots, (b) (r_v, θ_v) vs. $T \equiv |\Omega_o'|r_v(0)t$.

2.5 Nonlinear Trapping

In this section, we examine the time-scale for linear theory to break down in the mixing layer that surrounds a vortex. We find that for a prograde vortex, the time scale is practically instantaneous. This accounts for the apparent nonlinear behavior of holes, that was observed in Section 2.4. For a retrograde vortex, the linear time scale becomes infinite as $l/r_v \to 0$.

Figure 2.10.a shows the initial r-θ flow around a retrograde clump, with strength $l/r_v = 5 \times 10^{-2}$. Here, the stream lines are shown in a frame that rotates with the clump. Figure 2.10.b shows the r-θ flow around a prograde hole of the same strength. Both flows have mixing layers (shaded) centered at r_v, in which the θ-averaged background vorticity would flatten with time ($\frac{d\langle\zeta_b\rangle_\theta}{dr} \to 0$), were the vortex to remain stationary.

The clump's mixing layer consists of two regions: an inner trapping region (ITR) and an outer trapping region (OTR). This situation differs from the "slab approximation" where there was only one trapping region [shaded region in Fig. 2.4.a], corresponding to the ITR. The hole's mixing layer has only one part.

The success of linear theory for retrograde clumps and the failure of linear theory for prograde holes can be understood by considering the stream lines in Fig. 2.10. Linear theory breaks down when the trapped fluid (shaded) becomes mixed over length scales $\gtrsim l$, the small length-scale cut-off. Thus, linear theory breaks down for times greater than the orbital period of a fluid particle initially at $\vec{r}_*$, where $|\vec{r}_* - \vec{r}_v| \sim l$.

Let τ_* denote the orbital period of a fluid particle that has the initial polar coordinates $(r_v, -2l/r_v)$. This initial position is indicated by a '$*$' in Fig. 2.10. The period τ_* is plotted as a function of vortex strength l/r_v in Fig. 2.11, for both

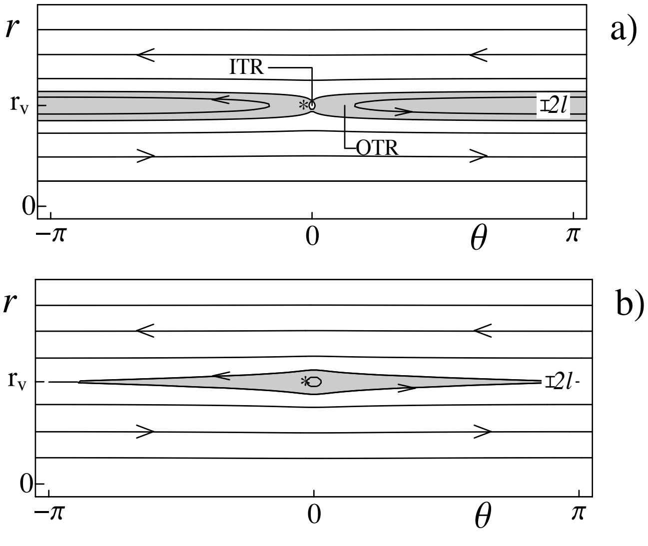

Figure 2.10: Initial stream lines and mixing layers (shaded) for **(a)** a retrograde clump and **(b)** a prograde hole at $r_v = 0.4$ in the circular shear flow given by Eq. (2.29). The stars correspond to the fluid particles whose orbital periods τ_* give the linear time-scale.

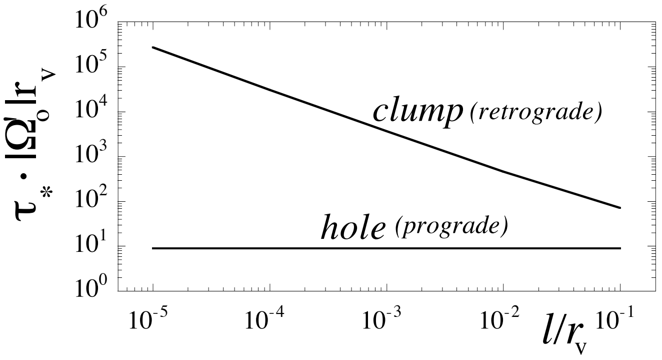

Figure 2.11: Linear time scale for prograde and retrograde vortices.

retrograde clumps and prograde holes.

For retrograde clumps, the fluid particle is in the OTR, and τ_* diverges to infinity as the vortex strength goes to zero. This divergence occurs because the particle velocity tends to zero (in the rotating frame) with the vortex strength, while the length of the orbit tends to a finite value ($4\pi r_v$). Thus, for retrograde clumps, linear theory stays valid infinitely long as $l/r_v \to 0$.

For prograde holes, the fluid particle has an orbit of length $\sim l$ and a velocity that is proportional to l; therefore τ_* remains constant as $l/r_v \to 0$. On the other hand, the time scale for the hole to move a distance of order l becomes infinite. Thus, the time scale for linear theory to fail becomes "instantaneous" relative to the time scale of vortex motion. This explains the sharp contrast between linear theory and the VIC simulation of the hole trajectory [Fig. 2.9].

Note that linear theory fails for holes not because the hole has negative vorticity, but because the hole is prograde with respect to the background shear flow in our example.

2.6 Mix-and-Move Estimate for Prograde Vortices

We now estimate the radial velocity of a prograde hole, using a "mix-and-move" argument. A more detailed estimate, which gives the same result, is carried out in Appendix VI.

A hole tends to mix a thin layer of background vorticity, and move a distance Δr in response. The mixing layer (ML) was described in Section 2.5, and corresponds to the shaded region in Fig. 2.10.b. From this figure, we see that the ML extends from $\theta = -\pi$ to π and has an average radial width of $\sim 2l$.

Suppose that the hole levels the entire ML ($\frac{d\left\langle \zeta_b \right\rangle_\theta}{dr} \to 0$) and has a negligible effect on fluid outside the ML. This mixing increases the background component of P_θ by an amount

$$\begin{aligned} \Delta P_{\theta,b} &\sim -\zeta_o' \int_{-\pi}^{\pi} d\theta \int_{r_v - l}^{r_v + l} dr\ r^3 (r - r_v) \\ &= -4\pi \zeta_o' r_v^2 l^3 + O(l^5). \end{aligned} \tag{2.30}$$

Here, we use the symbol '$\sim$' to indicate that the equation is an estimate. By conservation of P_θ, the hole must increase r_v by an amount Δr. Assuming that $\Delta r / r_v << 1$, we have

$$\Delta r = \frac{-\Delta P_{\theta,b}}{2\Gamma_v r_v} \sim l \frac{\zeta_o'}{\Omega_o'} \tag{2.31}$$

To obtain the hole velocity also requires an estimate of the time Δt for the ML to flatten. Presumably, this time is given by the orbital period of a fluid particle near the separatrix, which encloses the ML. We estimate that the average angular speed ($\dot{\theta}$) of this fluid particle is $\sim |\Omega_o'| l$, in the frame that rotates with the vortex. Since the orbit covers $\sim 4\pi$ radians (2π in both directions), we have

$$\Delta t \sim \frac{4\pi}{|\Omega_o'| l}. \tag{2.32}$$

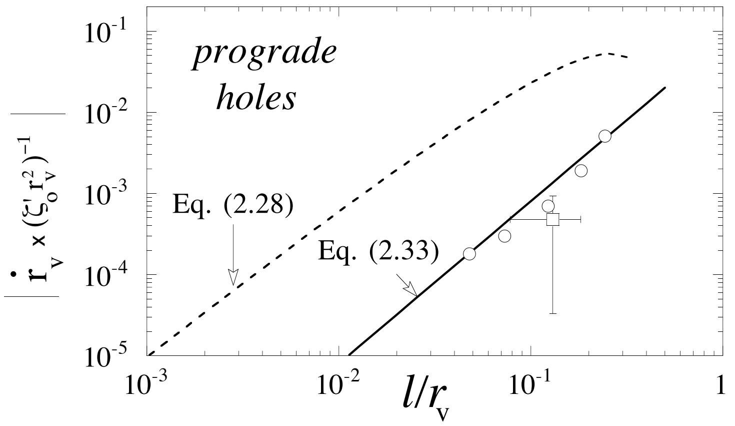

Figure 2.12: $\dot{r}_v$ vs. l/r_v for prograde holes in a VIC simulation (circles) and an experiment (square). The solid line is the prediction of the "mix-and-move" estimate [Eq. (2.33)], and the dashed line is the prediction of linear theory [Eq. (2.28)].

Finally, the velocity of the hole is given by

$$\dot{r}_v \sim \frac{\Delta r}{\Delta t} \sim -\frac{1}{4\pi} l^2 \zeta'_o. \tag{2.33}$$

Note that the l-scaling in linear theory [Eq. (2.28)] differs from the l-scaling in Eq. (2.33) by a factor of $ln(cr_v/l)$. Therefore, our estimate suggests that a retrograde vortex, which follows linear theory, will move infinitely faster than a prograde vortex as $l/r_v \to 0$.

In Fig. 2.12, we compare Eq. (2.33) to the late time hole velocities that are observed in the VIC simulations. As before, ζ_o is given by Eq. (2.29) and the holes are located initially at $r_v = 0.4$. The plotted values of $\dot{r}_v$ are from straight-line fits to r_v vs. t, as r_v increases from 0.5 to 0.6. The ratio l/r_v and the velocity normalization $\zeta'_o r_v^2$ are evaluated at $r_v = 0.55$.

The simulation velocities (denoted by O's) are between 0.6 and 1.1 times the values that are predicted by the mix-and-move estimate. Although the estimate is not perfect, it is much more accurate than linear theory (dashed line).

The drift velocity of holes down a vorticity gradient was recently measured by Huang, Fine and Driscoll [10]. This experiment was performed on a magnetized electron column, which behaves like an ideal 2D fluid. The experiment starts with an unstable flow that rapidly evolves into an axisymmetric vorticity distribution with two (occasionally 3) holes (Fig. 1.3). Typically these holes are evenly spaced in θ and have roughly the same values for r_v. The remainder of the relaxation is controlled by the slow drift of the holes down the background vorticity gradient, and out of the distribution.

There was some concern that the slow radial drift of holes was a "kitchen effect" of the experiment, which has nothing to do with 2D Euler flow. However, the measured value of $\dot{r}_v$ (plotted in Fig. 2.12) is within a factor of 4 of Eq. (2.33), which is at the level of our estimated error. Although strong conclusions should not be drawn from a single datum, it appears that we have captured the fundamental mechanism for the radial motion of holes in the experiments.

A more critical eye might notice, disregarding error bars, that the VIC simulation gives a larger value of $\dot{r}_v$ than the experiment. This suggests that the presence of an additional hole, which changes the structure of the ML, might slow down the outward radial drift. This has been verified by placing an additional hole in the VIC simulation, 180^o degrees opposite the original hole (and at the same r_v). The value of $\dot{r}_v$ decreases by a factor of 2, in close agreement with the experiment.

2.7 The Suppression of Gradient-Driven Drift by Large Shear

The mix-and-move estimate of the previous section assumes that the hole continuously moves into new regions where the θ-averaged background vorticity has a slope $\frac{d\langle\zeta_b\rangle_\theta}{dr} \approx \zeta_o'$. However, if the mixing layer (ML) moves with the hole,

$\frac{d\left<\zeta_b\right>_\theta}{dr}$ shortly becomes zero at r_v, and the radial drift stops.

We postulate that most of the ML moves adiabatically with the hole, and the radial drift is suppressed, when

$$t_l >> \Delta t. \tag{2.34}$$

Here, t_l is the predicted time for r_v to increase by l, which is the radial length scale of the ML, and Δt is the time required for the ML to be mixed.

In the previous section, we argued that the mixing time Δt is approximately $4\pi/l|\Omega'_o|$ [Eq. (2.32)]. The "escape time" t_l is given by $l/\dot{r}_v$. Here, we assume that $\dot{r}_v$ is given by Eq. (2.33). Putting these estimates into Eq. (2.34) yields the following condition for no radial drift (past a displacement of order l):

$$\frac{\Omega'_o}{\zeta'_o} >> 1. \tag{2.35}$$

Equation (2.35) indicates that a large shear prevents the prograde hole from drifting toward the edge of the background.

Alternatively, one can postulate that radial drift is suppressed when $l >> \Delta r$. Here, Δr is the radial displacement of the hole due to mixing of the entire ML, and is determined by conservation of P_θ. In the previous section, we estimated that $\Delta r \sim l\zeta'_o/\Omega'_o$ [Eq. (2.31)]. Using this result, we regain Eq. (2.35) for the suppression of radial drift.

For the simulation data in Fig. 2.12, $\Omega'_o/\zeta'_o = 1/3$, so only a small fraction of the ML moves with the hole.[2] However, by artificially increasing $|\Omega'_o|$ in the VIC simulation, so that Ω'_o/ζ'_o is greater than 1, we can examine hole motion when the mix-and-move model breaks down.

Figure 2.13 shows how $\dot{r}_v$ changes with Ω'_o/ζ'_o for holes of initial strength $l/r_v = 0.2$. The background vorticity is given by Eq. (2.29); however, the shear Ω'_o

---

[2] In the experiment, $\Omega'_o/\zeta'_o \sim 1/7$–$1/2$.

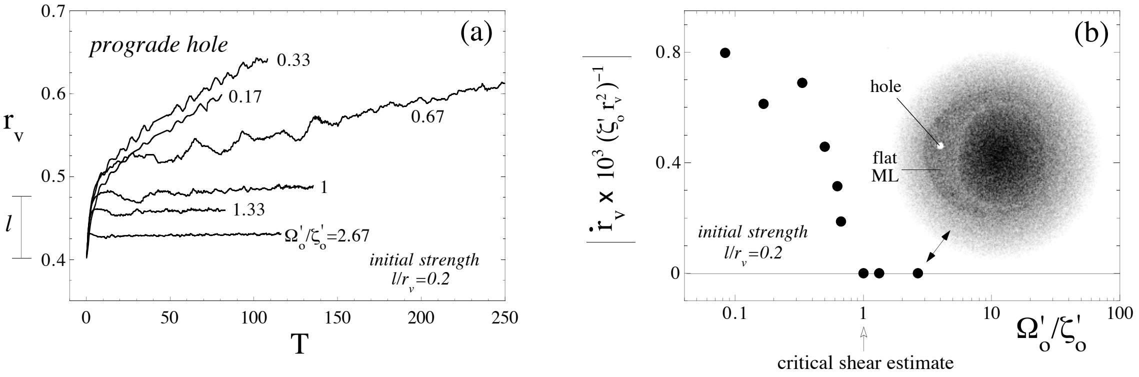

Figure 2.13: VIC simulations of the motion of a prograde hole in different levels of background shear. **(a)** r_v vs. T for different shear levels. **(b)** $\dot{r}_v$ vs. Ω'_o/ζ'_o. Inset: equilibrium obtained for $\Omega'_o/\zeta'_o = 2.67$.

is generally not consistent with Poisson's equation. Instead, the fluid particles in the VIC simulation are given an *additional* angular rotation frequency of the form $S \cdot r$, where the constant S is an adjustable parameter. The vortex strength l/r_v is kept fixed in this set of simulations by increasing Γ_v in proportion to the shear Ω'_o.

Figure 2.13.a shows r_v as a function of time for different shear levels. Here, $T \equiv |\Omega'_o| r_v(0) t$, with Ω'_o evaluated for the case of no additional shear ($S = 0$). Figure 2.13.b shows $\dot{r}_v$ vs. Ω'_o/ζ'_o. The value of $\dot{r}_v$ is obtained by a straight line fit to r_v vs. t, as the hole moves from $r_v = 0.5$ to 0.6. For $\Omega'_o/\zeta'_o < 1$, $\dot{r}_v$ is approximately constant, and equal to ~ 0.6 times the simple mix-and-move estimate, Eq. (2.33).[3] However, $\dot{r}_v$ drops to zero at $\Omega'_o/\zeta'_o \approx 1$, as predicted by Eq. (2.35). A velocity of zero means that the vortex stops drifting outward before a radial displacement of l.

The inset of Fig. 2.13.b is a contour plot of the equilibrium that forms when $\Omega'_o/\zeta'_o = 2.67$. Note that the ML has been flattened. The grey levels are the same

---

[3] To obtain the mix-and-move estimate, one must evaluate l at $r_v = 0.55$, not at the initial radial position, $r_v = 0.4$. At $r_v = 0.55$, the vortex strength l/r_v is 0.12, as opposed to the initial strength of 0.2.

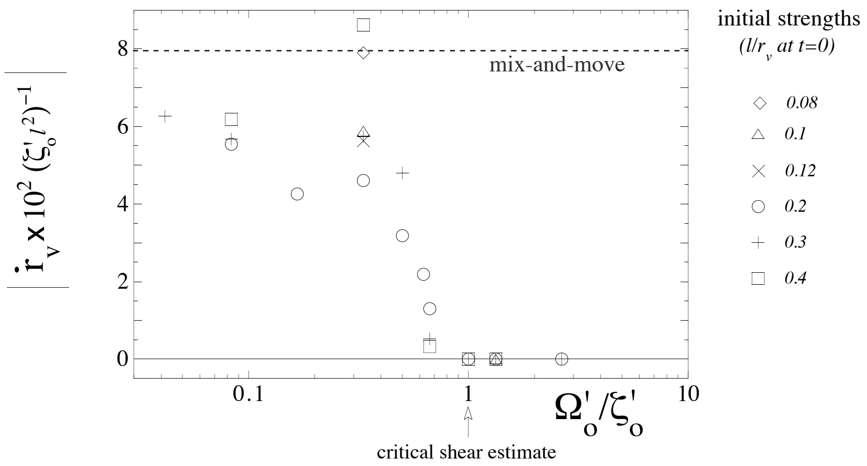

Figure 2.14: $\dot{r}_v$ vs. Ω'_o/ζ'_o for prograde holes with initial strengths l/r_v that range from 0.08 to 0.4. The critical shear for the suppression of radial drift seems independent of l, as predicted for prograde holes by Eq. (2.35).

as in Figs. 2.6 and 2.9. We note that the equilibration observed here is akin to the formation of a Bernstein-Greene-Kruskal mode in a nonlinear plasma wave [85].

Equation (2.35) suggests that, for prograde holes, the shear level required to suppress outward radial drift does not depend on l. This result is consistent with the VIC simulation data in Fig. 2.14. Here, the radial velocity is plotted as a function of shear strength Ω'_o/ζ'_o, for initial hole strengths l/r_v that range from 0.08 to 0.4. All cases show the same qualitative behavior. When $\Omega'_o/\zeta'_o \lesssim 1$, $\dot{r}_v$ is approximately given by the mix-and-move estimate. On the other hand, when $\Omega'_o/\zeta'_o \gtrsim 1$, $\dot{r}_v$ is zero.

A stronger shear is required to suppress the radial drift of a retrograde clump. The general criterion is presumably the same as for a prograde vortex, $\Delta t << t_l$. However, the mixing time Δt and escape time t_l both differ.

We show in Appendix VI that, for a retrograde vortex, $\Delta t \sim \dfrac{4\pi}{|\Omega'_o| l \sqrt{ln(r_v/l)}}$. Furthermore, we use the linear theory for $\dot{r}_v$ [Eq. (2.28), with $c = 1$] to estimate the escape velocity $t_l \equiv l/\dot{r}_v$. Then, the condition for an equilibrium to form

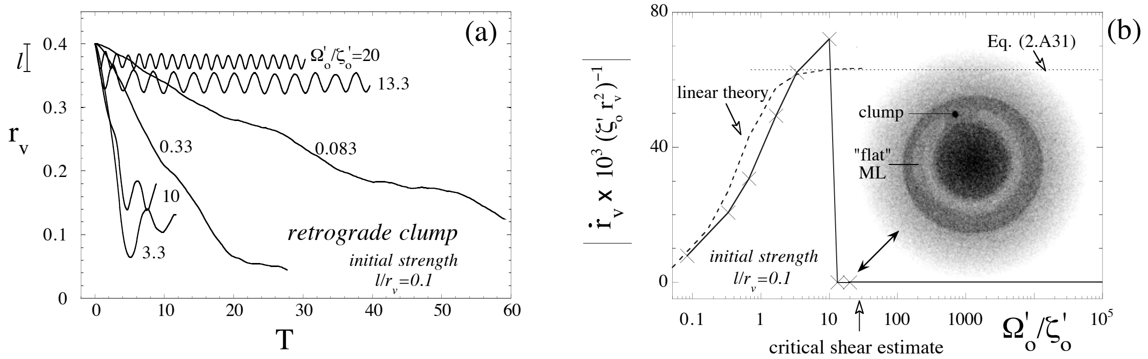

Figure 2.15: VIC simulations of the motion of a retrograde clump in different levels of background shear. **(a)** r_v vs. T for different shear levels. **(b)** $\dot{r}_v$ vs. Ω'_o/ζ'_o. X's: VIC simulations. The solid line connects points to aid the eye. Dashed line: Eq. (2.28), with c a function of Ω'_o. Inset: "equilibrium" obtained for $\Omega'_o/\zeta'_o = 20$.

($\Delta t << t_l$) becomes

$$\frac{\Omega'_o}{\zeta'_o} >> 2\pi^2\sqrt{ln(r_v/l)} \tag{2.36}$$

Eq. (2.36) is more stringent than Eq. (2.33) for prograde vortices. Here, as $l/r_v \to 0$, an infinite shear is required to suppress the radial drift.

Figure 2.15 illustrates how $\dot{r}_v$ changes with Ω'_o/ζ'_o for retrograde clumps, of initial strength $l/r_v = 0.1$. As before, the background vorticity is given by Eq. (2.29), and the shear is varied artificially. Figure 2.15.a shows r_v as a function of time for different shear levels. Fig. 2.15.b shows $\dot{r}_v$ as a function of Ω'_o/ζ'_o. The value of $\dot{r}_v$ is obtained from a straight line fit to r_v vs. t, as the clump descends from $r_v = 0.375$ to 0.35. As Ω'_o/ζ'_o increases, $\dot{r}_v$ increases and then drops to zero at $\Omega'_o/\zeta'_o \sim 10$. This transition point is just shy of the critical shear estimate, $2\pi^2\sqrt{ln(r_v/l)}$, which is indicated on the graph.

The inset of Fig. 2.15.b is a contour plot of the "equilibrium" that forms when $\Omega'_o/\zeta'_o = 20$. Here, we put "equilibrium" in quotes, because the ML is not fully mixed by the time the simulation was stopped ($T = 200$).

It is worth mentioning that linear theory still captures the initial increase in $\dot{r}_v$ with shear. The dashed curve in Fig. 2.15.b corresponds to linear theory, Eq. (2.28). Equation (2.28) for $\dot{r}_v$ depends explicitly on l, r_v and ζ_o' only. However, it can vary with shear because c depends implicitly on Ω_o'. Recall that c is obtained by summing the Green's functions in Eq. (2.26), which are profile dependent. Nevertheless, the value of c asymptotes to a fixed value c_* as $\Omega_o'/\zeta_o' \to \infty$. An equation for c_* is derived in Appendix III [Eqs. (2.A30-2.A32)].

Note that in Fig. 2.15.b, the curve for linear theory was calculated with $l/r_v = 0.116$, which is slightly greater than the initial vortex strength, $l/r_v = 0.1$. The larger vortex strength is due to the change in l/r_v from the initial vortex position ($r_v = 0.4$) to the point where the radial velocity is measured ($r_v = 0.363$).

2.8 Discussion: Gradient-Driven Drift as a Mechanism of Self-Organization in Natural Flows

Two-dimensional vortex motion driven by a background vorticity gradient has been examined numerically and analytically. Clumps (vorticity excesses) move up the gradient, whereas holes (vorticity deficits) move down the gradient. A linear analysis of the background vorticity evolution gives the motion of a retrograde vortex, under the condition that the vortex strength l/r_v is much less than one [Eq. (2.28)]. For prograde vortices, the background evolution is always nonlinear, and the vortices move at a slower rate. This rate is given by a simple mix-and-move estimate [Eq. (2.33)]. For both prograde and retrograde vortices, we found that there is a critical shear level, above which gradient-driven motion is suppressed [Eqs. (2.35,2.36)].

Our study of gradient-driven vortex motion was motivated by a 2D fluid experiment with a magnetized electron column [10]. The experiment by Huang,

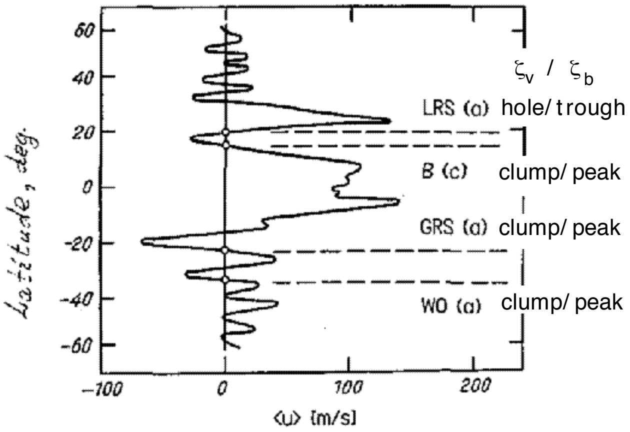

Figure 2.16: Location of long-lived storms in Jupiter's zonal flow [86]. LRS, B, GRS and WO denote Little Red Spot, Barges, Great Red Spot and White Ovals respectively. 'c' denotes cyclone and 'a' denotes anticyclone. The comments on ζ_v and ζ_b are mine.

Fine and Driscoll (Fig. 1.3) shows that holes are driven toward minima of the background vorticity. This experiment provides one example of a general principle that clumps and holes tend to migrate to (opposite) extremes in the background vorticity distribution. In particular, clumps move to peaks and holes move to troughs (Figs. 2.1,2.2).

It is natural to ask whether there is any evidence of clump/hole segregation on planets with strong zonal winds, where there may be significant background vorticity gradients. For an answer, we refer to Fig. 2.16, which shows the latitudes of long-lived storms in Jupiter's atmosphere, superposed on a sketch of the zonal velocity $\langle u \rangle$. This figure is taken directly from M.V. Nezlin et al (1994) [86]. Note that positive $\langle u \rangle$ corresponds to flow from west to east.

To understand Fig. 2.16 in terms of vorticity, we first translate $\langle u \rangle$ to background vorticity ζ_b. To obtain the vorticity ζ_b of the background zonal flow $\langle u \rangle$, we use the formula $\zeta_b = -\dfrac{d\langle u \rangle}{dy}$, where y is the local rectangular coordinate that is positive in the northward direction. Therefore, extrema in the background vorticity ζ_b correspond to regions where the shear strength is maximal. To identify a storm as a clump or a hole, we observe that in the northern hemisphere, an anticyclone rotates clockwise and is therefore a hole, whereas a cyclone rotates counter-clockwise and is therefore a clump. Contrarily, in the southern hemisphere, an anticyclone rotates counter-clockwise and is therefore a clump, whereas a cyclone rotates clockwise and is therefore a hole.

Our comments to the right of Fig. 2.16 indicate that the clumps (Barges, Great Red Spot, White Ovals) rest on peaks of background vorticity, whereas the single hole on the graph (the Little Red Spot) rests in a trough. This pattern is similar to the relaxed state of the simulated zonal flow in Fig. 2.2, in which a clump was guided to a peak in zonal vorticity, and a hole was guided to a minimum. It is not too far-fetched to speculate that the segregation of clumps and holes on Jupiter is in part due to zonal vorticity gradient; however, it is also possible that the vortices simply formed where they now reside.

The work presented in this chapter assumes that a background vorticity gradient already exists, and does not address the question of how a zonal flow is created. However, our results suggest that a pre-existing vorticity gradient may become steeper due to the gradient-driven separation of clumps and holes in the flow. Previously, we considered clumps, holes and background as separate entities, but in fact all contribute to the overall vorticity. As clumps and holes congregate at the peaks and troughs of the background, they steepen the overall vorticity distribution. The gradient driven separation of clumps and holes analyzed in this chapter provides a dynamical basis for calculating the rate at which such states are approached. In order to study this transport process, it is necessary to consider the interaction of many clumps and holes and their effect on background vorticity.

These subjects will be considered in future work.

2.9 Appendix I: Evaluation of the u-Integral

In this appendix, we evaluate the u-integral in Eq. (2.7), which gives the time dependence of the vortex's radial velocity $\dot{r}_v$.

Let $I(t)$ denote the integral:

$$I(t) \equiv \int_{-\infty}^{+\infty} du \frac{u}{u^2+1} ln \left[\frac{u^2+1}{(u-At)^2+1} \right]. \tag{2.A1}$$

To evaluate $I(t)$, we first expand the fraction $u/(u^2+1)$, using a sine transform. The expansion is given below:

$$\frac{u}{u^2+1} = \int_0^{\infty} dk e^{-k} sin(ku) \tag{2.A2}$$

Substituting Eq. (2.A2) into Eq. (2.A1) yields

$$I(t) = \int_0^{\infty} dk \int_{-\infty}^{\infty} d\nu ln \left[\frac{\left(\nu + \frac{At}{2}\right)^2 + 1}{\left(\nu - \frac{At}{2}\right)^2 + 1} \right] e^{-k} sin(k\nu) cos\left(k\frac{At}{2}\right). \tag{2.A3}$$

Here, we have made the transformation of variables $u \to \nu$, where $\nu = u - At/2$.

The ν integral in Eq. (2.A3) is tabulated in Gradshteyn and Ryzhik [87]:

$$\int_{-\infty}^{\infty} d\nu ln \left[\frac{\left(\nu + \frac{At}{2}\right)^2 + 1}{\left(\nu - \frac{At}{2}\right)^2 + 1} \right] sin(k\nu) = \frac{4\pi}{k} e^{-k} sin\left(k\frac{At}{2}\right). \tag{2.A4}$$

Substituting Eq. (2.A4) into Eq. (2.A3), we obtain

$$\begin{aligned} I &= 2\pi \int_0^{\infty} dk e^{-2k} \frac{sin(kAt)}{k} \\ &= 2\pi tan^{-1}(T/2) sgn(A), \end{aligned} \tag{2.A5}$$

where $T = |A|t$. The second equation in (2.A5) is the desired result.

2.10 Appendix II: Numerical Solution of the Green's Function

In this appendix, we describe the numerical method that we use for finding the Green's function $G(r|r_v, s)$ of the differential operator D_s [Eq. (2.22)], in the limit that s goes to zero along the positive real axis.

Since we are approaching the limit $s = 0$ along the positive real axis, we set $s \equiv \alpha$, where α is a *positive* real. Then, $D_s \rightarrow D_\alpha$, which is defined below:

$$D_\alpha \equiv \frac{\partial^2}{\partial r^2} + \frac{1}{r}\frac{\partial}{\partial r} - \frac{m^2}{r^2} - \frac{\zeta_o'(r)}{r\left[\Omega_o(r) - i\alpha/m\right]}. \tag{2.A6}$$

The Green's function $G(r|r_v, \alpha)$ satisfies the following equation:

$$D_\alpha[G(r|r_v, \alpha)] = \frac{\delta(r - r_v)}{r_v}. \tag{2.A7}$$

The solution for G has the form

$$G(r|r_v, \alpha) = \begin{cases} c f_\alpha(r) & r < r_v \\ \\ d h_\alpha(r) & r > r_v. \end{cases} \tag{2.A8}$$

Here, f_α and h_α satisfy the homogeneous equations

$$D_\alpha[f_\alpha, h_\alpha] = 0, \tag{2.A9}$$

and the boundary conditions

$$\begin{bmatrix} f_\alpha(0) \\ \\ h_\alpha(R_w) \end{bmatrix} = 0. \tag{2.A10}$$

Both boundary conditions in Eq. (2.A10) are due to the fact that G is proportional to the Laplace transform of the stream function $\tilde{\Psi}$ [Eq. (2.20)], which vanishes at both the origin and the wall.

The boundary conditions on G at $r = r_v$ are given below:

$$\begin{bmatrix} d h_\alpha(r_v) - c f_\alpha(r_v) \\ \\ d h_\alpha'(r_v) - c f_\alpha'(r_v) \end{bmatrix} = \begin{bmatrix} 0 \\ \\ 1/r_v \end{bmatrix}. \tag{2.A11}$$

These boundary conditions can be used to obtain the values of c and d. The solution yields the following equation for G:

$$G(r|r_v,\alpha) = \begin{cases} \dfrac{f_\alpha(r)h_\alpha(r_v)}{r_v W_\alpha(r_v)} & r < r_v \\ \\ \dfrac{f_\alpha(r_v)h_\alpha(r)}{r_v W_\alpha(r_v)} & r > r_v. \end{cases} \tag{2.A12}$$

Here, W_α is the Wronksian determinant:

$$W_\alpha(r) \equiv f_\alpha(r)h'_\alpha(r) - h_\alpha(r)f'_\alpha(r). \tag{2.A13}$$

The functions f_α and h_α are obtained as follows. First, we observe that D_α reduces to the radial part of the Laplacian L, as both $r \to 0$ and $r \to R_w$:

$$D_\alpha \to L \equiv \frac{\partial^2}{\partial r^2} + \frac{1}{r}\frac{\partial}{\partial r} - \frac{m^2}{r^2}. \tag{2.A14}$$

The term in D_α that is proportional to ζ'_o does not contribute as $r \to 0$, because it is subdominant to m^2/r^2. The same term does not contribute as $r \to R_w$, because $\zeta'_o = 0$ in the gap between the background radius R_b and the wall radius R_w.

From Eq. (2.A14), and the boundary conditions in Eq. (2.A10), we obtain

$$f_\alpha(r) \sim ar^m \qquad (r \to 0), \tag{2.A15}$$

and

$$h_\alpha(r) \sim b\left[r^m - \frac{R_w^{2m}}{r^m}\right] \qquad (r \to R_w). \tag{2.A16}$$

Our choice of a and b are arbitrary: they cancel in Eq. (2.A12) for the Green's function G.

Equation (2.A15) and Eq. (2.A16) provide boundary conditions for solving Eq. (2.A9) numerically. For f_α the boundary conditions are

$$\begin{bmatrix} f_\alpha(\varepsilon) \\ \\ f'_\alpha(\varepsilon) \end{bmatrix} = \begin{bmatrix} a\varepsilon^m \\ \\ am\varepsilon^{m-1} \end{bmatrix}. \tag{2.A17}$$

Here, ε is a parameter of the numerical integration. The value of ε must be sufficiently small that f_α has converged to its true functional form. For h_α, the boundary conditions are

$$\left[\begin{array}{c} h_\alpha(R_w) \\ \\ h'_\alpha(R_w) \end{array}\right] = \left[\begin{array}{c} 0 \\ \\ 2bm(R_w)^{m-1} \end{array}\right]. \tag{2.A18}$$

Finally, to obtain the radial drift of the vortex [Eq. (2.26)], we need $G(r|r_v,\alpha)$ in the limit that $\alpha \to 0$. Thus, we decrease α until $G(r|r_v,\alpha)$ converges to its limit.

2.11 Appendix III: Analytic Solutions for the Green's Function

In this appendix, we demonstrate that the imaginary part of $G(r_v|r_v,0^+)$ is given by Eq. (2.27) for large m. We will also argue that Eq. (2.27) is valid for all m in the limit of "infinite" shear.

2.11.1 Green's Function for Large m

For analysis, it is convenient to rewrite the differential equation for the Green's function, Eq. (2.21), as follows:

$$\left[L - \frac{im\zeta'_o(r)}{r\left[s + im\Omega_o(r)\right]}\right] G(r|r_v,s) = \frac{\delta(r-r_v)}{r_v}. \tag{2.A19}$$

Here, L is the radial part of the Laplacian, which is defined in Eq. (2.A14). Note that G has an implicit m-dependence.

We now decompose the Green's function into two parts:

$$G(r|r_v,s) \equiv g_o(r|r_v) + g_1(r|r_v,s). \tag{2.A20}$$

Here $g_o(r|r')$ is the standard Green's function of L

$$L[g_o(r|r')] = \frac{\delta(r-r')}{r'}, \tag{2.A21}$$

and $g_o(r|r_v)$ in Eq. (2.A20) accounts for the vortex stream function. The explicit functional form of $g_o(r|r_v)$ is given below:

$$g_o(r|r_v) \equiv -\frac{1}{2m}\left(\frac{r_<}{r_>}\right)^m \left[1 - \left(\frac{r_>}{R_w}\right)^{2m}\right], \tag{2.A22}$$

where $r_>(r_<)$ is the greater (smaller) of r and r_v.

The "correction" g_1 accounts for the response of the background to the vortex. Substituting Eq. (2.A20) into Eq. (2.A19) gives the following differential equation for g_1:

$$L[g_1(r|r_v,s)] = \frac{im\zeta_o'(r)}{r\left[s + im\Omega_o(r)\right]}\left\{g_o(r|r_v) + g_1(r|r_v,s)\right\}. \tag{2.A23}$$

A formal integral solution to Eq. (2.A23) is given below:

$$g_1(r|r_v,s) = \int_0^{R_b} dr' g_o(r|r')\frac{im\zeta_o'(r')}{\left[s + im\Omega_o(r')\right]}\left\{g_o(r'|r_v) + g_1(r'|r_v,s)\right\}, \tag{2.A24}$$

where R_b is the radius of the background. We can use the Plemelj formula (and some minor algebra) to evaluate the integral in the the limit $s \to 0^+$, yielding

$$\begin{aligned} g_1(r|r_v,0^+) = P\int_0^{R_b} dr'\frac{\zeta_o'(r')}{\Omega_o(r')}\left\{1 + \frac{g_1(r'|r_v,0^+)}{g_o(r'|r_v)}\right\} g_o(r|r')g_o(r'|r_v) \\ + \frac{i\pi\zeta_o'(r_v)}{|\Omega_o'(r_v)|}\left\{1 + \frac{g_1(r_v|r_v,0^+)}{g_o(r_v|r_v)}\right\} g_o(r_v|r_v)g_o(r|r_v). \end{aligned} \tag{2.A25}$$

Note that the Plemelj formula applies at $r = r_v$, since $\Omega_o(r_v) = 0$ in the rotating frame.

So far, we have made no approximations. However, for large m, we will assume that

$$\left|g_1(r|r_v,0^+)\right| << \left|g_o(r|r_v)\right|. \tag{2.A26}$$

Then, for large m, the terms involving g_1/g_o in Eq. (2.A25) can be neglected, yielding

$$g_1(r|r_v,0^+) \approx P\int_0^{R_b} dr'\frac{\zeta_o'(r')}{\Omega_o(r')} g_o(r|r')g_o(r'|r_v) + g_o(r|r_v)\frac{i\pi\zeta_o'(r_v)}{|\Omega_o'(r_v)|}g_o(r_v|r_v). \tag{2.A27}$$

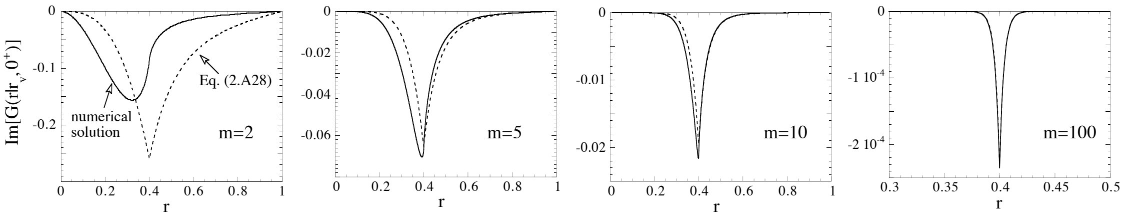

Figure 2.17: Convergence of $Im[G]$ to Eq. (2.A28) as $m \to \infty$.

Equation (2.A27) gives a solution that is consistent with our original assumption, Eq. (2.A26), in the limit of large m. From Eq. (2.A22), we have $g_o \sim 1/m$, and by inspection of Eq. (2.A27), we have $g_1 \sim 1/m^2$. Therefore, $|g_1| << |g_o|$ for large m.

We are interested primarily in the imaginary part of $G(r|r_v, 0^+)$, since it alone contributes to $\dot{r}_v$ [Eq. (2.26)]. Since g_o is real, the imaginary part of $G(r|r_v, 0^+)$ is equal to the imaginary part of $g_1(r|r_v, 0^+)$.

In the large m limit, we argued that $g_1(r|r_v, 0^+)$ is given by Eq. (2.A27). The integral in Eq. (2.A27) is real. So, in the large m limit, the imaginary part of $G(r|r_v, 0^+)$ is given solely by the second term on the right of Eq. (2.A27):

$$Im[G(r|r_v, 0^+)] \approx g_o(r|r_v) \frac{\pi \zeta_o'(r_v)}{|\Omega_o'(r_v)|} g_o(r_v|r_v). \tag{2.A28}$$

Equation (2.A28) is compared to a numerical solution in Fig. 2.17. Here, the background is given by Eq. (2.29), and $r_v = 0.4$. The numerical solution for $Im[G(r|r_v, 0^+)]$ is in good agreement with theory, for $m \gtrsim 10$.

We now use Eq. (2.A28) to evaluate $Im[G(r_v|r_v, 0^+)]$, which appears in Eq. (2.26) for $\dot{r}_v$. Substituting Eq. (2.A22) for g_o into Eq. (2.A28), we find that

$$Im\left[G(r_v|r_v, 0^+)\right] \approx \frac{\pi \zeta_o'(r_v)\left[1 - \left(\frac{r_v}{R_w}\right)^{2m}\right]^2}{4m^2|\Omega_o'(r_v)|}. \tag{2.A29}$$

For large m, $(r_v/R_w)^{2m}$ is negligible, and Eq. (2.A29) reduces to Eq. (2.27) of the main text.

2.11.2 Green's Function for Large Shear

In Section 2.7, we discussed the effect of large shear on $\dot{r}_v$. Our primary point was that large shear brings $\dot{r}_v$ to zero, by causing the mixing layer to flatten rapidly. However, this suppression of radial drift occurs only when Ω_o'/ζ_o' exceeds a critical level [Eqs. (2.35, 2.36)]. For weaker shear, we found that linear theory provides a good approximation for $\dot{r}_v$, in the case of a retrograde vortex. Moreover, we saw that in linear theory, $\dot{r}_v$ asymptotes to a finite value as $\Omega_o' \rightarrow \infty$, provided that l, ζ_o' and r_v are kept fixed [Fig. 2.15.b]. We now calculate this "infinite" shear limit of $\dot{r}_v$.

We first demonstrate that Eq. (2.A27) is valid for *all* m, as $\Omega_o' \rightarrow \infty$. In this limit, both terms on the right-hand-side of Eq. (2.A27) tend to zero, for all m. Therefore, for large shear and all m, Eq. (2.A27) gives a self-consistent solution: $|g_1| << |g_o|$.

This means that for all m we can use Eq. (2.A29), which gives an expression for $Im[G(r_v|r_v, 0^+)]$ based on Eq. (2.A27). Substituting Eq. (2.A29) into Eq. (2.26) for $\dot{r}_v$, we obtain

$$\begin{matrix} lim \\ t \rightarrow \infty \end{matrix} \; \dot{r}_v = \pm\frac{\pi}{2}\zeta_o'(r_v)l^2 \sum_{m=1}^{\sqrt{e}r_v/l} \frac{1}{m}\left[1-\left(\frac{r_v}{R_w}\right)^{2m}\right]^2. \qquad (2.A30)$$

Note that this expression for $\dot{r}_v$ depends only on l, ζ_o', r_v and R_w. If these quantities are held fixed as Ω_o' increases, there will be no change in $\dot{r}_v$.

For small l/r_v, Eq. (2.A30) has the following approximate form:

$$\begin{matrix} lim \\ t \rightarrow \infty \end{matrix} \; \dot{r}_v = \pm\frac{\pi}{2}\zeta_o'(r_v)l^2 ln(c_* r_v/l), \qquad (2.A31)$$

where c_* is defined below:

$$c_* = \begin{matrix} lim \\ l/r_v \rightarrow 0 \end{matrix} \; \frac{l}{r_v}\, exp\left\{\sum_{m=1}^{\sqrt{e}r_v/l} \frac{1}{m}\left[1-\left(\frac{r_v}{R_w}\right)^{2m}\right]^2\right\}. \qquad (2.A32)$$

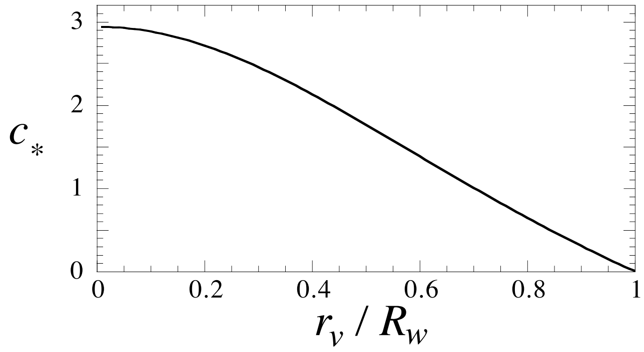

Figure 2.18: The "infinite" shear limit of c as a function of r_v/R_w.

The functional dependence of c_* on r_v/R_w was obtained numerically and is plotted in Fig. 2.18.

Figure 2.15.b of the main text demonstrates that Eq. (2.A31) gives the correct value for the "infinite" shear limit of $\dot{r}_v$, in linear theory.

2.12 Appendix IV: Time Asymptotic Limit of the ω-Integral

In this appendix, we evaluate the $t \to \infty$ limit of the ω-integral in Eq. (2.24), which is required to obtain the late time limit of $\dot{r}_v$.

Let $J(t)$ denote this integral:

$$J(t) \equiv P \int_{-\infty}^{\infty} d\omega \frac{G(r|r_v, 0^+ + i\omega)}{\omega} e^{i\omega t}. \qquad (2.A33)$$

We now make the change of variables $\omega \to \nu$, where $\nu \equiv \omega t$. In terms of ν, we have

$$J(t) = P \int_{-\infty}^{\infty} d\nu \frac{G(r|r_v, 0^+ + i\nu/t)}{\nu} e^{i\nu}. \qquad (2.A34)$$

In the $t \to \infty$ limit, Eq. (2.A34) becomes

$$\begin{matrix} lim \\ t \to \infty \end{matrix} \; J(t) = G(r|r_v, 0^+) \; P \int_{-\infty}^{\infty} d\nu \frac{cos\nu + isin\nu}{\nu}. \qquad (2.A35)$$

The cosine term in Eq. (2.A35) vanishes, since $cos\nu/\nu$ is odd. The sine term yields

$$\begin{array}{c} lim \\ t \to \infty \end{array} J(t) = i\pi G(r|r_v, 0^+). \tag{2.A36}$$

Equation (2.A36) is the desired result.

2.13 Appendix V: Stream Lines in the Mixing Layer

In this appendix, we examine the flow around a small vortex, which can be prograde or retrograde. In particular, we consider the flow at $t = 0$, before the vortex perturbs the background. The results derived here are used in Appendix VI to estimate the radial velocity of a prograde hole, which can not be calculated using linear theory. The results are also used in Appendix VI to estimate the critical shear [Eqs. (2.35, 2.36)] for the suppression of radial drift.

Up to an arbitrary constant, the stream function around a vortex of circulation Γ_v in a shear flow $\Omega_o(r)$ is

$$\psi = \int_0^r dr'r'\Omega_o(r') + \frac{\Gamma_v}{4\pi} ln\left[r^2 + r_v^2 - 2rr_v cos(\theta - \theta_v)\right]. \tag{2.A37}$$

Here, we have neglected the image of the vortex due to the wall. We now go into a rotating frame where $\Omega_o(r_v)$ is zero, and we set θ_v equal to zero. Furthermore, we assume that Ω_o' is approximately constant. Then, the stream function in Eq. (2.A37) simplifies to

$$\psi = \Omega_o'\left(\frac{r^3}{3} - \frac{r_v r^2}{2}\right) + \frac{\Gamma_v}{4\pi} ln\left(r^2 + r_v^2 - 2rr_v cos\theta\right). \tag{2.A38}$$

The important nonlinear dynamics occurs in the mixing layer (ML). Consequently, we focus on stream lines in this region. We refer the reader to Section 2.5, and in particular Fig. 2.10, for our definition of the ML.

All stream lines are contours along which $\psi(r,\theta)$ is constant. A stream line in the ML is parameterized by the angle θ_ψ ($0 \leq \theta_\psi \leq \pi$), where it passes through r_v (the radial position of the vortex). The stream line equation is $\psi(r,\theta) = \psi(r_v, \theta_\psi)$, or equivalently

$$\rho^2 + \frac{2}{3}\rho^3 \pm \left(\frac{l}{r_v}\right)^2 ln\left[\frac{2(1+\rho)\cdot(1-cos\theta)+\rho^2}{2(1-cos\theta_\psi)}\right] = 0. \qquad (2.A39)$$

Here, $\rho \equiv (r - r_v)/r_v$ and l is defined by Eq. (2.12). The sign of the third term is '+' for a prograde vortex ($\Gamma_v/\Omega_o' > 0$) and '$-$' for a retrograde vortex ($\Gamma_v/\Omega_o' < 0$).

For $l/r_v << 1$, and $\theta >> l/r_v$, we obtain the following approximation for ρ:

$$\rho(\theta) \approx \begin{cases} \pm\dfrac{l}{r_v}\sqrt{ln\left[\dfrac{1-cos\theta_\psi}{1-cos\theta}\right]} & prograde \quad (a) \\ \\ \pm\dfrac{l}{r_v}\sqrt{ln\left[\dfrac{1-cos\theta}{1-cos\theta_\psi}\right]} & retrograde \quad (b) \end{cases} \qquad (2.A40)$$

2.14 Appendix VI: Analysis of Nonlinear Motion

2.14.1 Detailed Mix-and-Move Estimate for $\dot{r}_v$

We now carry out a detailed mix-and-move estimate for the radial velocity $\dot{r}_v$ of a prograde hole in an initially axisymmetric background, where $\zeta_o', \Omega_o' < 0$. This detailed estimate yields the same expression for $\dot{r}_v$ as our simple estimate, Eq. (2.33).

As in the main text, we assume that the hole levels the ML (shaded region in Fig. 2.10.b) and has a negligible effect on fluid outside the ML. Then, a reasonable estimate for $\dot{r}_v$ is given by

$$\dot{r}_v \sim \left\langle \frac{-\Delta P_{\theta,b}}{2\Gamma_v r_v \tau} \right\rangle_\psi . \qquad (2.A41)$$

Here, $\Delta P_{\theta,b}$ is the change in the background's angular momentum that occurs upon flattening the coarse-grained vorticity distribution inside a stream line that

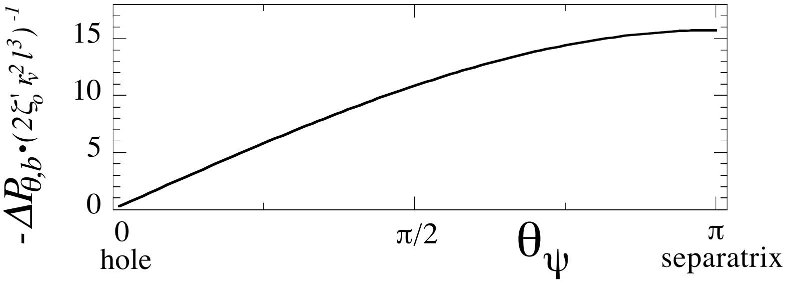

Figure 2.19: $\Delta P_{\theta,b}$ vs. θ_ψ for a prograde hole.

encircles the hole, τ is the orbital period of a fluid particle on that stream line, and $<>_\psi$ denotes an average over the stream lines in the ML. We have used conservation of P_θ [Eq. (2.2)] to relate the change in r_v to the change in $P_{\theta,b}$. Note that the orbital period τ is infinite on the separatrix. Therefore, if we used the particle orbit on the separatrix to evaluate $\dot{r}_v$, instead of an average, we would obtain $\dot{r}_v = 0$.

The change in $P_{\theta,b}$ that occurs due to mixing is given by the following integral:

$$\Delta P_{\theta,b}(\theta_\psi) = -\zeta_o' r_v^5 \int_{-\theta_\psi}^{\theta_\psi} d\theta \int_{-\rho_\psi(\theta)}^{\rho_\psi(\theta)} d\rho \, (1+\rho)^3 \rho. \tag{2.A42}$$

Here, $\rho \equiv (r - r_v)/r_v$, and $(\rho, \theta) = 0$ gives the location of the hole. The function $\rho_\psi(\theta)$ is the (positive) value of ρ at the polar angle θ on a stream line given by a particular value of ψ. The angle θ_ψ is the maximum angle reached by a fluid particle on that stream line. For example, $\theta_\psi = \pi$ for the separatrix, which can be seen in Fig. 2.10.b. Equation (2.A42) assumes that ζ_o' is constant over the ML, and that the stream lines in the ML are approximately symmetric about r_v ($\rho = 0$).

The function $\rho_\psi(\theta)$ is approximately given by Eq. (2.A40.a). Substituting Eq. (2.A40.a) into Eq. (2.A42), we obtain

$$\Delta P_{\theta,b}(\theta_\psi) = -2\zeta_o' r_v^2 l^3 \int_{-\theta_\psi}^{\theta_\psi} d\theta \; ln^{3/2} \left[\frac{1 - cos\theta_\psi}{1 - cos\theta} \right] \tag{2.A43}$$

to lowest order in l. Figure 2.19 shows $\Delta P_{\theta,b}$ as a function of θ_ψ. Here, we see that

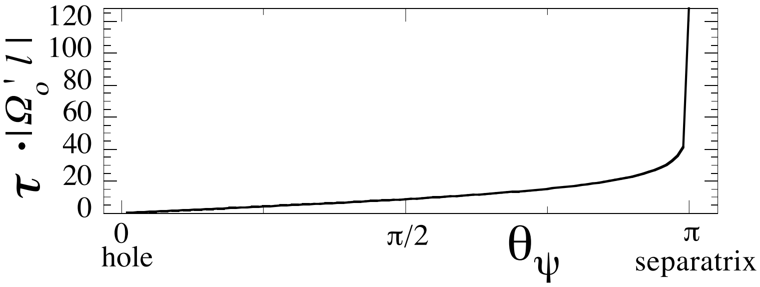

Figure 2.20: Orbital period τ vs. θ_ψ for a prograde hole.

$\Delta P_{\theta,b}$ increases monotonically with θ_ψ, due to the fact that the area enclosed by the stream line increases with θ_ψ.

The orbital period of a fluid particle is given by

$$\tau(\theta_\psi) = 4\int_{-\theta_\psi}^{0} d\theta/\dot{\theta}. \tag{2.A44}$$

Here, $\dot{\theta}$ is the angular velocity of the fluid particle along the stream line. This angular velocity has contributions from the background shear and the vortex field, and can be written as follows:

$$\dot{\theta} = \Omega_o' r_v \cdot \left[\rho_\psi + \left(\frac{l}{r_v}\right)^2 \frac{1}{1+\rho_\psi} \cdot \frac{1+\rho_\psi - cos\theta}{2(1+\rho_\psi)(1-cos\theta)+\rho_\psi^2}\right]. \tag{2.A45}$$

For the most part, ρ_ψ is $O(l/r_v)$ [see Eq. (2.A40)]; therefore, it is a reasonable approximation to drop the second term in Eq. (2.A45). Then, using Eq. (2.A40.a) for ρ_ψ, we have

$$\dot{\theta} = \pm\Omega_o' l \sqrt{ln\left[\frac{1-cos\theta_\psi}{1-cos\theta}\right]}, \tag{2.A46}$$

where $+$ is for $\rho_\psi > 0$ and $-$ is for $\rho_\psi < 0$. The expression for τ becomes

$$\tau(\theta_\psi) = \frac{4}{|\Omega_o'|l}\int_{-\theta_\psi}^{0} d\theta\, ln^{-1/2}\left[\frac{1-cos\theta_\psi}{1-cos\theta}\right]. \tag{2.A47}$$

Figure 2.20 shows τ as a function of θ_ψ. Note that τ becomes infinite near the separatrix ($\theta_\psi = \pi$).

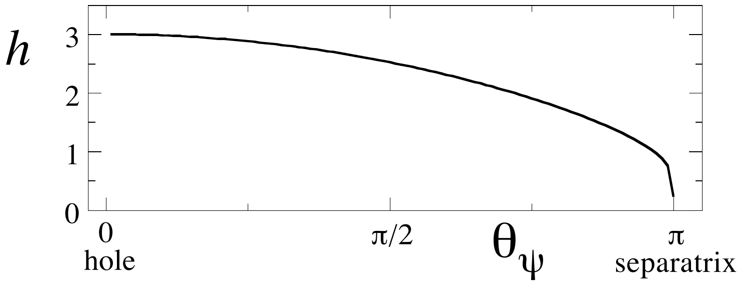

Figure 2.21: h vs. θ_ψ.

Substituting Eqs. (2.A43) and (2.A47) into Eq. (2.A41), we obtain the following expression for $\dot{r}_v$:

$$\dot{r}_v \sim -\frac{1}{4\pi} l^2 \zeta_o' \left\langle h(\theta_\psi) \right\rangle_\psi , \tag{2.A48}$$

where the function $h(\theta_\psi)$ is defined below:

$$h(\theta_\psi) \equiv \frac{1}{2} \frac{\displaystyle\int_{-\theta_\psi}^{\theta_\psi} d\theta \; ln^{3/2} \left[\frac{1 - cos\theta_\psi}{1 - cos\theta} \right]}{\displaystyle\int_{-\theta_\psi}^{0} d\theta \; ln^{-1/2} \left[\frac{1 - cos\theta_\psi}{1 - cos\theta} \right]} . \tag{2.A49}$$

The function $h(\theta_\psi)$ is plotted in Fig. 2.21. The values of h range from 0 to 3. Moreover, h is of order unity everywhere except in a thin layer near the separatrix ($\theta_\psi = \pi$). Therefore, it is reasonable to choose an averaging scheme such that $\langle h \rangle_\psi = 1$. Then, Eq. (2.A48) is equivalent to our simple estimate, Eq. (2.33).

2.14.2 Mixing Times

We now estimate the time Δt for a vortex to level the surrounding mixing layer (ML). This time was used in Section 2.7 to estimate the critical shear for the suppression of radial drift. Recall that radial drift is suppressed when $\Delta t << t_l \equiv l/\dot{r}_v$.

We first determine the mixing time for the ML that surrounds a prograde vortex [Fig. 2.10.b]. This mixing time Δt_p corresponds to a typical orbital period of a fluid particle in the ML. These orbital periods are shown as a function of θ_ψ in Fig. 2.20. Unfortunately, the orbital periods range from zero to infinity, so that a "typical" value is not obvious.

However, a better definition for Δt_p is the time for most of the area in the ML to be mixed. Of course, the entire ML takes infinitely long to mix, since the orbital period on the separatrix ($\theta_\psi = \pi$) is infinite. So, rather than set Δt_p equal to $\tau(\pi)$, we set it equal to $\tau(\pi/2)$. That is,

$$\Delta t_p \equiv \tau(\pi/2) = \frac{4}{|\Omega_o'|l} \int_{-\pi/2}^{0} d\theta \; ln^{-1/2} \left[\frac{1}{1 - cos\theta} \right]. \tag{2.A50}$$

Here we have used Eq. (2.A47) for the orbital period τ. Note that there is nothing special about $\theta_\psi = \pi/2$, besides the fact that it is $O(1)$.

In Section 2.7, we gave a rough estimate for the mixing time of a prograde hole:

$$\Delta t_p \sim 4\pi/|\Omega_o'|l \qquad (2.A51).$$

Equation (2.A50) gives a value of Δt_p that, for all l/r_v, is 0.68 times this rough estimate.

We now calculate the mixing time Δt_r for the ML that surrounds a retrograde vortex [Fig. 2.10.a]. As for the prograde case, we require that most of the ML is mixed by the time Δt_r. Therefore, we will estimate that Δt_r is the orbital period τ of a fluid particle, whose radial position at $\theta = \pi$ is midway between r_v and the separatrix. A straight-forward calculation shows that the orbit of this particle intersects r_v at

$$\theta_\psi = \alpha \left(\frac{l}{r_v} \right)^{1/4}, \tag{2.A52}$$

where $\alpha \equiv 4^{3/8} e^{-1/8}$.

In analogy to Eq. (2.A47), which gives τ for particles orbiting a prograde vortex, the following equation gives τ for particles in the ML that surrounds a

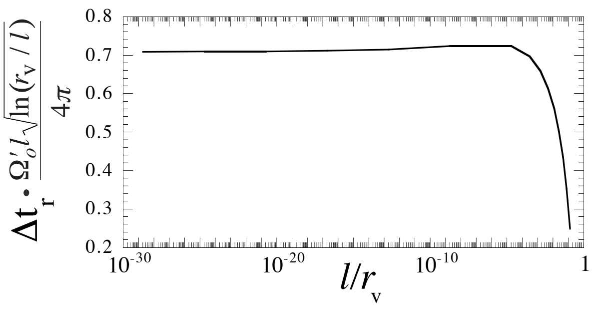

Figure 2.22: The mixing time for the retrograde case.

retrograde vortex:

$$\tau(\theta_\psi) = \frac{4}{|\Omega_o'|l} \int_{-\pi}^{-\theta_\psi} d\theta\ ln^{-1/2} \left[\frac{1 - cos\theta}{1 - cos\theta_\psi}\right]. \tag{2.A53}$$

Using Eq. (2.A52) for θ_ψ gives the mixing time Δt_r:

$$\Delta t_r \equiv \tau\left(\alpha(l/r_v)^{1/4}\right) = \frac{4}{|\Omega_o'|l} \int_{-\pi}^{-\alpha(l/r_v)^{1/4}} d\theta\ ln^{-1/2} \left[\left(\frac{r_v}{l}\right)^{1/2} \frac{2}{\alpha^2}(1 - cos\theta)\right]. \tag{2.A54}$$

Here, we have used $cos\theta_\psi \approx 1 - \theta_\psi^2/2$. Note that in contrast to the prograde case [Eq. (2.A50)], the integral in Eq. (2.A54) depends on l.

In Section 2.7, we gave a rough estimate for the mixing time:

$$\Delta t_r \sim \frac{4\pi}{|\Omega_o'|l\sqrt{ln(r_v/l)}} \tag{2.A55}$$

Figure 2.22 shows that Eq. (2.A54) converges to 0.71 times this rough estimate as $l/r_v \to 0$.

Part of this chapter has been published in Physical Review Letters, David A. Schecter and Daniel H. E. Dubin, **83**, 2191-2194 (1999). David A. Schecter was the primary investigator and author of this paper.

Chapter 3

An Eigenmode Analysis of the Excitation and Inviscid Damping of Small Perturbations on a 2D Vortex

3.1 Introduction

Two-dimensional flows are often dominated by a single vortex or by a group of interacting vortices. Although the vortex dynamics can be complicated, it is possible to gain a precise understanding of certain elementary processes. One example is the evolution of asymmetric perturbations on an initially circular vortex.

The evolution of elliptical perturbations on a circular vortex has been studied in recent experiments, where the working 2D fluid is a magnetized electron plasma [11, 43]. These experiments are carried out at high Reynolds numbers, so that viscous effects are negligible. In some experiments the elliptical perturbation persists, but more often it decays. We refer to this decay as "inviscid damping." The excitation and inviscid damping of asymmetries (primarily elliptical) on a 2D vortex are the main topics of this chapter.

Figure 3.1 shows an experiment where inviscid damping occurs. At $t = 0$, an elliptical perturbation is created on the vortex. Subsequently, the vortex

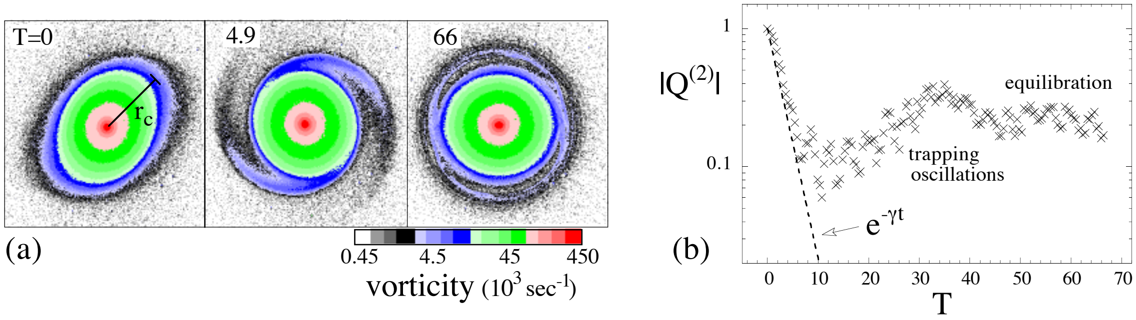

Figure 3.1: Experiment. **(a)** The evolution of vorticity after an elliptical perturbation is applied to an initially circular vortex. As filamentation occurs at r_c, the vorticity contours relax back to circular form for $r \lesssim r_c$. **(b)** The relaxation of the quadrupole moment (ellipticity). The dashed line indicates that the initial decay is exponential. Time is measured in central rotation periods, $T \equiv t\,\Omega_o(0)/2\pi$, and the quadrupole moment $Q^{(2)}$ is normalized to its initial value.

relaxes toward an axisymmetric state. During the relaxation, filaments are shed at a critical radius r_c, and vorticity contours become circular in the core of the vortex. Moreover, the ellipticity of the vortex decays *exponentially* by one order of magnitude before reaching a terminal value. Here, the ellipticity is measured by the amplitude of the $m = 2$ multipole moment (the quadrupole moment).

The decay process observed experimentally (e.g. Fig. 3.1) resembles previous numerical simulations of the 2D Euler equations [39, 40, 41, 42]. We show, in Section 3.6, that the initial exponential decay in the experiments is actually governed by the *linearized* Euler equations.

To study the linear excitation and evolution of perturbations on a vortex, we use an eigenmode formalism [44, 45, 46, 47]. In this formalism, the perturbation is viewed as a sum of independent eigenmodes. We demonstrate that the eigenmodes of a monotonic vortex are neutrally stable, and form an orthogonal basis. Next, we derive a general formula for the response of each eigenmode to a flow field that is briefly superimposed on the vortex. We then study how the total excitation relaxes through the dispersion, or "phase-mixing" of these modes.

We first examine the evolution of initial conditions that model the experiments. These perturbations are formed by a brief application of a flow field that compresses the vortex along a minor axis and expands the vortex along a major axis, thereby creating an ellipse. The applied flow is generated by sources at the wall of a confinement cylinder. We refer to this applied flow as an "external impulse," because the sources are outside the vortex, and act only for a brief period. We find in general that after an external impulse, the quadrupole moment of the vortex has an early stage of exponential decay, in accord with the experiments. This result is significant, since arbitrary perturbations need not decay exponentially.

However, the possibility of exponential decay has been known for some time [48, 49, 50]. A Laplace transform solution to the initial value problem shows that any perturbation will have a contribution from a "Landau pole". This Landau pole contribution behaves exactly like an exponentially damped mode, but can never represent a complete solution to the initial value problem, since at late times the decay turns algebraic [48, 88, 89, 90, 91]. The frequency ω_q and decay rate γ of a Landau pole depends only on the azimuthally symmetric equilibrium profile of the vortex. We will show that a Landau pole correctly gives the observed exponential decay of the quadrupole moment that follows an external impulse.

Next, we turn our attention from the quadrupole moment to the vorticity perturbation $\Delta\zeta(r, \theta, t)$. Here, (r, θ) is a polar coordinate system that has its origin at the center of the vortex. When $\gamma/\omega_q << 1$, we find that the vorticity perturbation (in addition to the quadrupole moment) decays exponentially with time for all radii less than a critical radius r_c, where filamentation occurs.

That is, the vorticity perturbation acts like an exponentially damped eigenmode: $\Delta\zeta(r,\theta,t) \approx \xi(r)e^{-\gamma t}cos(2\theta-\omega_q t)$ for $r \lesssim r_c$. The critical radius r_c occurs where the fluid rotation frequency $\Omega_o(r)$ is resonant with the perturbation, and satisfies the equation $2\Omega_o(r_c) = \omega_q$.

These weakly damped excitations are referred to as "quasi-modes", since they are not exact eigenmodes of the linearized Euler equations. We will show that a quasi-mode is actually a wave-packet of neutral eigenmodes, which occupy a narrow frequency band. Exponential decay occurs due to phase-mixing and interference of these neutrally stable modes.

We then analyze the case of strong damping ($\gamma/\omega_q \sim 1$), using a Gaussian vortex as an example. Here, we find that the narrow wave-packet occurring in weakly damped quasi-modes is replaced by a broad band wave-packet. Because the wave-packet is broad, the vorticity perturbation forms filaments over the entire radial extent of the vortex, rather than in a thin critical layer. Thus, even though the quadrupole moment behaves like an exponentially damped mode, the vorticity perturbation does not.

We now provide an outline of the main text. In Section 3.2, we review the eigenmode theory of linear perturbations on a circular vortex [46, 47]. In Section 3.3, we discuss the eigenmodes of monotonic vortices, which are stable to small perturbations [48]. Examples are given for a vortex with a discrete mode, and a vortex with a quasi-mode.

In Section 3.4, we show that the excitation of an eigenmode due to an external impulse is proportional to the (scaled) multipole moment of that eigenmode. Therefore, the system exhibits reciprocity: the eigenmodes with the strongest influence on the external flow are also the most sensitive to a brief flow field that is created by an external source.

In Section 3.5, we examine in detail the response of several stable vortices to an external $m = 2$ impulse. In all cases, we show that the quadrupole moment of the induced asymmetry decays exponentially at a rate given by a Landau pole of the vortex. In Section 3.6, we demonstrate that linear theory properly describes the initial evolution of perturbations in the experiments with magnetized electron columns. In Section 3.7, we examine the importance of Landau poles in the evolution of arbitrary perturbations, which need not be generated by an external impulse. We find that the exponential decay of a Landau pole commonly dominates an intermediate stage of the evolution when $\gamma/\omega_q << 1$ (weak damping), but rarely dominates when $\gamma/\omega_q \sim 1$ (strong damping).

In Section 3.8, we briefly discuss eigenmode theory for non-monotonic profiles, which can be unstable [48]. Several equations that were derived strictly for monotonic vortices are here generalized. In Section 3.9, we carry out a numerical stability analysis of a "hollow" vortex, with the primary goal of illustrating pitfalls in the numerical technique. In Section 3.10, we discuss conservation of energy, angular momentum and the moments of vorticity during inviscid damping.

In Appendix I, we explain how inviscid damping is a consequence of angular momentum conservation. In Appendix II, we discuss an analogy between the eigenmode problem of the 2D Euler equations and the eigenmode problem of the 1D Vlasov Poisson equations, which are used in the kinetic theory of plasma waves. In Appendix III, we review how to calculate Landau poles numerically [50].

3.2 Linear Eigenmode Theory

In this section, we outline a numerical technique for calculating the eigenmodes of a 2D vortex [46, 47]. An eigenmode expansion will be used in later sections to calculate the linear evolution of small perturbations.

3.2.1 The Eigenvalue Equation

We consider a vortex that is governed by the 2D Euler equations, which assume incompressibility and zero viscosity:

$$\begin{aligned}&(a)\ \ \partial\zeta/\partial t+\vec{v}\cdot\nabla\zeta=0,\\ &(b)\ \ \vec{v}=\hat{z}\times\nabla\psi, \qquad (3.1)\\ &(c)\ \ \nabla^2\psi=\zeta.\end{aligned}$$

Here, $\vec{v}(r,\theta,t)$ is the velocity field, $\zeta(r,\theta,t)\equiv\hat{z}\cdot\nabla\times\vec{v}$ is the vorticity and $\psi(r,\theta,t)$ is a stream function. We also assume that the fluid is bounded by a circular wall at which there is free-slip; i.e., $\psi=0$ at the wall radius R_w.

The vorticity distribution can be decomposed into an axisymmetric equilibrium $\zeta_o(r)$ and a perturbation $\Delta\zeta(r,\theta,t)$,

$$\zeta(r,\theta,t)\equiv\zeta_o(r)+\Delta\zeta(r,\theta,t). \qquad (3.2)$$

If the perturbation is small, we can approximate its evolution with the linearized Euler equations,

$$\frac{\partial\Delta\zeta}{\partial t}+\Omega_o\frac{\partial\Delta\zeta}{\partial\theta}-\frac{1}{r}\zeta_o'\frac{\partial\Delta\psi}{\partial\theta}=0 \qquad (3.3)$$

$$\left(\frac{\partial^2}{\partial r^2}+\frac{1}{r}\frac{\partial}{\partial r}+\frac{1}{r^2}\frac{\partial^2}{\partial\theta^2}\right)\Delta\psi=\Delta\zeta. \qquad (3.4)$$

Here, $\Delta\psi(r,\theta,t)$ is the perturbation to the stream function, $\zeta_o'(r)$ is the radial derivative of $\zeta_o(r)$ and $\Omega_o(r)$ is the angular rotation frequency of the unperturbed circular flow,

$$\Omega_o(r)=\frac{1}{r^2}\int_0^r dr'r'\zeta_o(r'). \qquad (3.5)$$

The present aim is to express an arbitrary perturbation as a superposition of eigenmodes. We will look for eigenmodes of the form

$$\begin{aligned}\Delta\zeta &= \xi(r)e^{\mathrm{i(m\theta-\omega t)}}\\ \Delta\psi &= \Psi(r)e^{\mathrm{i(m\theta-\omega t)}},\end{aligned} \tag{3.6}$$

where $m = 1, 2, \ldots \infty$. In Eq. (3.6), the radial eigenfunctions ξ and Ψ depend implicitly on the azimuthal wave-number m and the eigenfrequency ω. Substituting this ansatz into Eq. (3.3) and Eq. (3.4), we find that the radial eigenfunctions must satisfy the following pair of equations:

$$(\omega - m\Omega_o)\,\xi + \frac{m}{r}\zeta_o'\Psi = 0 \tag{3.7}$$

$$\left(\frac{d^2}{dr^2} + \frac{1}{r}\frac{d}{dr} - \frac{m^2}{r^2}\right)\Psi = \xi. \tag{3.8}$$

Equations (3.7) and (3.8) can be transformed into a single integral equation for the vorticity eigenfunction ξ. First Eq. (3.8) is solved with a Green's function,

$$\Psi(r) = \int_0^{R_w} dr'r'G_m(r|r')\xi(r'). \tag{3.9}$$

The Green's function G_m incorporates the boundary conditions that $\Psi = 0$ at R_w and that Ψ is finite (zero) at the origin. Specifically,

$$G_m(r|r') = -\frac{1}{2m}\left(\frac{r_<}{r_>}\right)^m\left[1 - \left(\frac{r_>}{R_w}\right)^{\mathrm{2m}}\right]. \tag{3.10}$$

Here, $r_>$ is the larger of r and r', and $r_<$ is the smaller of r and r'. Substituting Eq. (3.9) into Eq. (3.7), we obtain the following integral eigenvalue equation:

$$[\omega - m\Omega_o(r)]\,\xi(r) + \frac{m}{r}\zeta_o'(r)\int_0^{R_w} dr'r'G_m(r|r')\xi(r') = 0. \tag{3.11}$$

It is convenient to introduce a compact notation and rewrite the eigenvalue equation as follows:

$$I\left[\xi\right] = \omega\xi. \tag{3.12}$$

Here, I denotes the linear integral operator defined below

$$I\left[\xi\right] \equiv m\Omega_o(r)\xi(r) - \frac{m}{r}\zeta_o'(r)\int_0^{R_v} dr'r'G_m(r|r')\xi(r'). \tag{3.13}$$

Note that I is determined by m and the equilibrium distribution $\zeta_o(r)$ (through Ω_o and ζ_o'). Equation (3.13) assumes that the vorticity perturbation is restricted to r less than the vortex radius R_v, beyond which the equilibrium vorticity $\zeta_o(r)$ is zero. This restriction is not necessary, but it will simplify our discussion in what follows. It is straight-forward to generalize to perturbations that extend past R_v by increasing the upper limit of integration in Eq. (3.13).

Equation (3.12) produces two kinds of eigenmodes: discrete modes and continuum modes. A general linear perturbation, of the form $\delta\zeta(r,t)e^{im\theta}$, can be expanded into a sum of the discrete modes plus an integral of the continuum modes [44, 45, 46, 47]:

$$\delta\zeta(r,t) = \sum_d A(\omega_d)\xi_d(r)e^{-i\omega_d t} \ + \int d\omega A(\omega)\xi_\omega(r)e^{-i\omega t} \tag{3.14}$$

The discrete modes have eigenfunctions $\xi(r)$ that are spatially smooth. Therefore, a discrete mode is a physical solution to the linearized Euler equations. On the other hand, the radial eigenfunction of a continuum mode has a singular point where the fluid rotation is resonant with that mode [44, 45, 47, 50]. In Section 3.3, we discuss continuum modes in greater detail. For now, let it suffice to say that only integrals of the continuum modes have physical meaning.

3.2.2 A Numerical Solution to the Eigenvalue Equation and the Initial Value Problem

In general, the integral eigenvalue equation must be solved numerically. To do so, we consider ξ and I on a radial grid:

$$r_i \in \{\Delta r, 2\Delta r, \ldots, N\Delta r\}. \tag{3.15}$$

Then, the eigenvalue equation for I is approximated by a system of N linear equations:

$$\sum_{j=1}^{N} M_{ij}\xi(r_j) = \omega\xi(r_i). \tag{3.16}$$

Here, the index i runs from 1 to N. The matrix elements of M are real, and they are given below:

$$M_{ij} = m\Omega_o(r_i)\delta_{ij} - m\frac{r_j}{r_i}\zeta_o'(r_i)G_m(r_i|r_j)\Delta r. \tag{3.17}$$

In deriving this expression for M_{ij}, we have used trapezoidal integration to approximate the integral operator I.

So, the eigenmodes of an ideal axisymmetric vortex can be found numerically by solving the eigenvalue problem of the matrix M. The solution gives N eigenmodes of the form $\xi_k(r_i)e^{i(m\theta-\omega_k t)}$, where $k = 1, 2, \ldots N$. These eigenmodes include the discrete modes and a finite set that represents the continuum.

A linear perturbation on the vortex is approximated by a superposition of these eigenmodes. Specifically, $\Delta\zeta$ and $\Delta\psi$ can be expanded as follows:

$$\begin{aligned} \Delta\zeta(r_i,\theta,t) &= \sum_{\mathrm{m}=1}^{+\infty} \delta\zeta^{(m)}(r_i,t)e^{im\theta} + c.c. \\ &\approx \sum_{\mathrm{m}=1}^{+\infty}\sum_{k=1}^{N} A_k^{(m)}\xi_k^{(m)}(r_i)e^{\mathrm{i(m\theta-\omega_k^{(m)}t)}} + c.c. \end{aligned} \tag{3.18}$$

$$\begin{aligned} \Delta\Psi(r_i,\theta,t) &= \sum_{m=1}^{+\infty} \delta\psi^{(m)}(r_i,t)e^{im\theta} + c.c. \\ &\approx \sum_{m=1}^{+\infty}\sum_{k=1}^{N} A_k^{(m)}\Psi_k^{(m)}(r_i)e^{\mathrm{i(m\theta-\omega_k^{(m)}t)}} + c.c. \end{aligned} \tag{3.19}$$

Here, the approximation symbol refers to the fact that the expansion is numerical (finite N). The superscript m denotes the azimuthal wave-number and A_k is a constant expansion coefficient that is obtained from the initial perturbation (explicit formulas for A_k are provided in later sections). If the perturbation consists of multiple wave-numbers, then separate sets of ξ_k and ω_k must be obtained for each value of m.

The numerical expansion [Eq. (3.18)] breaks down after a finite time τ, due to the finite number ($\leq N$) of eigenmodes that represent the continuum. This time τ increases as the frequency spacing $\Delta\omega$ between neighboring eigenfrequencies decreases. As a rule, we find that the maximum difference between neighboring eigenfrequencies in the discretized continuum is proportional to the maximum shear and to the radial grid-point spacing Δr ($= R_v/N$). That is,

$$\Delta\omega_{max} \approx max\{|m\Omega_o'\Delta r|\}. \tag{3.20}$$

It is reasonable to expect that after a time

$$\tau \sim 2\pi/\Delta\omega_{max}, \tag{3.21}$$

artificial bouncing should occur in the amplitude of the vorticity perturbation. This artificial bouncing is typically observed. However, it is possible that the expansion will be valid for longer times if the eigenmodes are excited in a narrow frequency band. Specifically, if this frequency band is centered at $\bar{\omega} \equiv m\Omega_o(\bar{r})$, then the time scale for accurate results should extend to $\tau \sim 2\pi/\left|m\Omega_o'(\bar{r})\Delta r\right|$.

For this thesis, the eigenvalue problem was solved numerically using the double precision LAPACK routine, DGEEV. This routine computes the eigenfrequencies and the left and right eigenvectors of a general matrix. Typically, N is between 10^3 and 10^4, and the computations take between one minute and one hour of cpu time on the present (1999) DEC ALPHA workstations.

3.3 The Eigenmodes of a Monotonic Vortex

We define a "monotonic vortex" as a vortex whose equilibrium profile decreases monotonically with r until reaching zero at R_v:

$$\begin{aligned} \zeta_o'(r) < 0 \qquad & for \qquad 0 < \; r \le R_v, \; and \\ \zeta_o(r) = 0 \qquad & for \qquad \qquad r \ge R_v. \end{aligned} \tag{3.22}$$

In Sections 4-7, we study the excitation and decay of asymmetries on monotonic vortices. In preparation, we now examine the eigenmodes of a monotonic vortex.

3.3.1 General Results

The eigenmodes of all monotonic vortices have several common features. For example, all eigenfrequencies of a monotonic vortex are real. Therefore, all eigenmodes of a monotonic vortex are neutrally stable.[1]

To verify the neutral stability of eigenmodes, we define the following inner-product:

$$\begin{aligned} \langle f,h\rangle \;\; & \equiv \int_0^{R_v} \frac{r^2}{|\zeta_o'(r)|} f^*(r)h(r)dr \\ & = \sum_{i=1}^{N} \frac{r_i^2}{|\zeta_o'(r_i)|} f^*(r_i)h(r_i)\Delta r. \end{aligned} \tag{3.23}$$

Here, the asterisk denotes the complex conjugate and the second equality is the discretized (i.e. working) definition of the inner-product.

The matrix M is Hermitian (self-adjoint) with respect to the inner-product in Eq. (3.23). That is,

$$\langle f, Mh\rangle = \langle h, Mf\rangle^* . \tag{3.24}$$

Equation (3.24) can be verified in a straight-forward manner, when two conditions are kept in mind: (1) that the Green's function $G_m(r_i|r_j)$ is symmetric with respect

---

[1] For a cylindrical analogue to Rayleigh's inflection point theorem that proves the stability of monotonic profiles, see Ref.[48].

to interchange of r_i and r_j, and (2) that $\zeta_o' < 0$ for *all* $r_i \leq R_v$. Because M is Hermitian, its eigenfrequencies $\{\omega_k\}$ are real.

In addition, Hermiticity assures us that M has N linearly independent eigenvectors $\{\xi_k\}$. Assuming that the eigenfrequencies are distinct, the eigenvectors are orthogonal:

$$\langle \xi_k, \xi_{k'} \rangle = \begin{cases} \text{positive real} & k = k' \\ 0 & k \neq k'. \end{cases} \tag{3.25}$$

The orthogonality relations in Eq. (3.25) can be used to derive a formula for the coefficients $\{A_k\}$ of the eigenmode expansion. The formula is given below:

$$A_k^{(m)} = \frac{\left\langle \xi_k^{(m)}, \delta\zeta^{(m)}(r,0) \right\rangle}{\left\langle \xi_k^{(m)}, \xi_k^{(m)} \right\rangle}. \tag{3.26}$$

Here, $\delta\zeta^{(m)}(r,0)$ is the m^{th} Fourier-coefficient of the vorticity perturbation at time $t = 0$. The inner-product is the weighted sum that is defined by Eq. (3.23).

3.3.2 The Eigenmodes of a Top-Hat Vortex

As an example, we consider a vortex for which the equilibrium vorticity ζ_o slowly decreases from the center and then rapidly drops to zero in a transition layer of width δr centered about the radius r_o. This vortex is shown in Fig. 3.2.a, and will be referred to as *Top-Hat 1.* The exact functional form of Top-Hat 1 is not important; nevertheless, it is given below:

$$\zeta_o(r) = \begin{cases} .485\left[1 - 1.01\tanh\left(\frac{r-r_o}{\delta r}\right)\right]\left[1 + .025\left(\frac{R_v - r}{R_v}\right)\right] & r < R_v \\ 0 & r \geq R_v, \end{cases} \tag{3.27}$$

where $\delta r = 0.01$, $r_o = 0.3$ and $R_v = 0.327$. Here, and throughout this chapter, all lengths are given in units of R_w. In addition, all frequencies are given in units of $\zeta_o(0)$. Thus, $\zeta_o(0) = 1$ in Eq. (3.27).

The $m = 2$ eigenmodes of Top-Hat 1 typify the eigenmodes for all m. Figure 3.2.b shows a selection of eigenfunctions $\{\xi_k\}$ from the $m = 2$ spectrum. The eigenfunctions are labelled by their eigenfrequencies. Some of the corresponding stream functions $\{\Psi_k\}$ are shown in Fig. 3.2.c. Note that each eigenfunction ξ_k is normalized so that its peak amplitude is 1. This normalization will be used for all numerical results.

In the $m = 2$ spectrum, we find that there exist $N-1$ eigenfrequencies that fall in the range $2\Omega_o(R_v) < \omega_k < 2\Omega_o(0)$. As the number of radial grid-points N increases, this subset of eigenfrequencies becomes increasingly dense. In the limit as N goes to infinity, the distance between neighboring eigenfrequencies becomes zero. Therefore, this subset represents the continuum of $I^{(2)}$. For an arbitrary wave-number m, a similar continuum will exist. The upper and lower limits of this continuum are given below:

$$m\Omega(R_v) < \omega_k < m\Omega(0). \tag{3.28}$$

The radial eigenfunction ξ_k of a continuum mode has a singular point at its critical radius $r_{c,k}$. The critical radius of an eigenmode is the radius at which the unperturbed fluid corotates with that eigenmode. It is defined by the following equation:

$$\omega_k \equiv m\Omega_o(r_{c,k}). \tag{3.29}$$

On one side of $r_{c,k}$, the radial eigenfunction ξ_k tends toward positive infinity. On the other side of $r_{c,k}$, ξ_k tends toward negative infinity [45, 47, 50]. The $N-1$ critical radii of the continuum modes are distributed with approximate uniform spacing across the vortex.

In the $m = 2$ spectrum of Top-Hat 1, there also exists a discrete eigenfrequency ω_d that lies outside the continuum. The critical radius $r_{c,d}$ of this discrete mode, defined by $\omega_d = m\Omega_o(r_{c,d})$, lies in a gap of zero vorticity between the vortex radius R_v and the wall radius R_w. As a result, the eigenfunction of the discrete

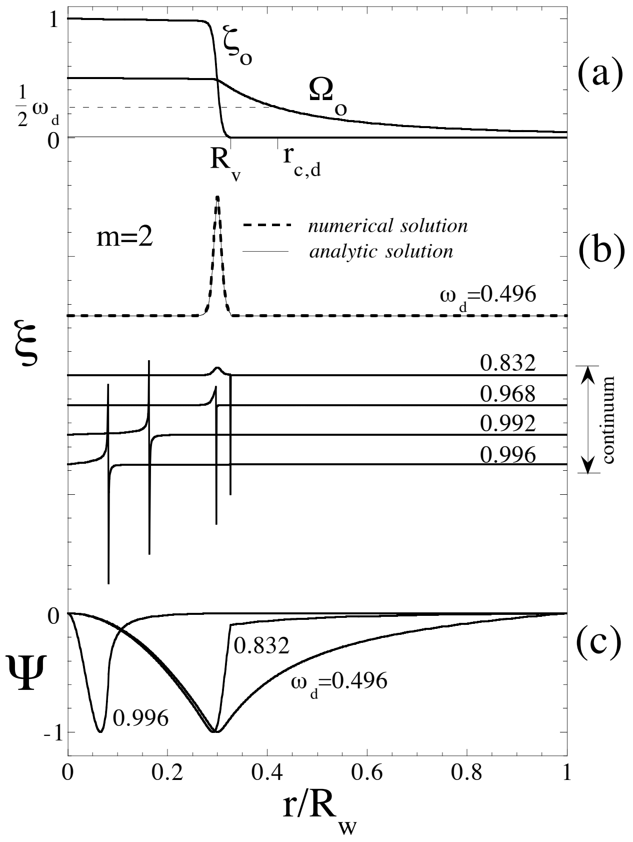

Figure 3.2: Top-Hat 1. **(a)** Equilibrium profile: ω_d and $r_{c,d}$ denote the frequency and critical radius of the $m = 2$ discrete mode. **(b)** $m = 2$ eigenfunctions (eigenvectors of the matrix M). All eigenfunctions are zero at $r = 0$. To aid the eye, opposite extremes are connected at the singular point of each continuum eigenfunction. **(c)** Stream functions for several eigenmodes: each stream function is divided by its peak amplitude.

mode (top of Fig. 3.2.b) has no singular point.

It is straight-forward to derive an approximate analytic expression for this discrete mode. The analytic solution is best understood if we first consider the discrete modes of a uniform circular vortex-patch:

$$\zeta_o(r) = \begin{cases} 1 & r \leq r_o \\ 0 & r > r_o. \end{cases} \tag{3.30}$$

In 1880, Kelvin derived a dispersion relation for waves that propagate along the edge of this patch [92]. Formally, these waves are delta-function disturbances at

r_o:

$$\Delta\zeta = \delta(r - r_o)e^{i(m\theta - \omega_* t)}. \tag{3.31}$$

Substituting Eq. (3.31) into the linearized Euler equations, one finds that

$$\omega_* = \frac{1}{2}\left[m - 1 + \left(\frac{r_o}{R_w}\right)^{2m}\right]. \tag{3.32}$$

An additional calculation shows that the critical radius of each wave is given by

$$r_* = r_o\left[\frac{m}{m - 1 + (r_o/R_w)^{2m}}\right]^{1/2}. \tag{3.33}$$

This critical radius lies outside the vortex-patch for all m; therefore, the modes studied by Kelvin are discrete eigenmodes.

Because Top-Hat 1 resembles a uniform vortex-patch, the discrete modes of Top-Hat 1 are similar to those of a uniform vortex-patch. Of course, the discrete modes of Top-Hat 1 are not delta-functions. Replacing $\delta(r - r_o)$ in Eq. (3.31) is a sharply peaked but finite eigenfunction,

$$\xi_d(r) \propto \frac{G_m(r|r_o)}{m\Omega_o(r) - \omega_d}\frac{1}{r}\zeta_o'(r). \tag{3.34}$$

This approximate result is obtained from the integral eigenvalue equation [Eq. (3.11)] under the assumption that $\zeta_o'(r)$ is sharply peaked at r_o. At the top of Fig. 3.2.b, Eq. (3.34) is compared to the $m = 2$ discrete eigenfunction of Top-Hat 1. The two are in excellent agreement. In addition, we can use the Kelvin frequency ω_* as an estimate for ω_d. Numerically, we find that $\omega_d = .496$. This value differs by less than two percent from $\omega_* = .504$. Here, we have used $r_o = 0.3R_w$ to evaluate ω_*.

Although we have focused on a monotonic vortex with a single sharp edge at r_o, it is important to note that discrete modes exist on monotonic vortices of all kinds. For example, discrete modes can exist even when the vorticity gradient ζ_o' is roughly constant across the entire vortex. If there are multiple peaks in ζ_o', then there can be multiple peaks in the radial eigenfunction of the discrete mode. In short, discrete modes can be found in a wide variety of forms; but in all cases, the discrete modes are extended versions of the "edge-waves" that can propagate on a uniform vortex-patch.

3.3.3 Discrete Mode to Quasi-Mode

In this subsection, we compare the undamped discrete mode, which exists when $\zeta_o'(r_{c,d}) = 0$, to the exponentially damped quasi-mode, which exists when $\zeta_o'(r_{c,d}) < 0$.

The discrete mode of Top-Hat 1 can be "merged" with the continuum by stretching the vortex radius R_v past $r_{c,d}$. *Top-Hat 2* in Fig. 3.3.a is equivalent to Top-Hat 1, except for a skirt of vorticity that tapers past $r_{c,d}$. As expected, all eigenmodes of Top-Hat 2 are continuum modes: all eigenfrequencies lie inside the continuum [Eq. (3.28)], and all eigenfunctions have singular points at their respective critical radii [Eq. (3.29)].

However, the discrete eigenmode of Top-Hat 1 has not disappeared entirely. This can be seen by inspection of the continuum modes. Figure 3.3.b shows a selection of eigenfunctions from the $m = 2$ continuum. The dashed continuum modes have eigenfrequencies near ω_d, the discrete eigenfrequency of Top-Hat 1. They closely resemble the discrete mode of Top-Hat 1, except that each continuum mode has a singular point near $r_{c,d}$ (the critical radius of the discrete mode).

These "exceptional" continuum modes have an important physical significance: they combine to form a quasi-mode. Consider the discrete mode of Top-Hat 1 as an initial condition on Top-Hat 2. This initial condition will now evolve as a superposition of continuum modes. Figure 3.3.c shows the expansion coefficients A_k versus ω_k. The distribution is sharply peaked near the eigenfrequency ω_d; therefore, the perturbation consists primarily of the exceptional continuum modes.

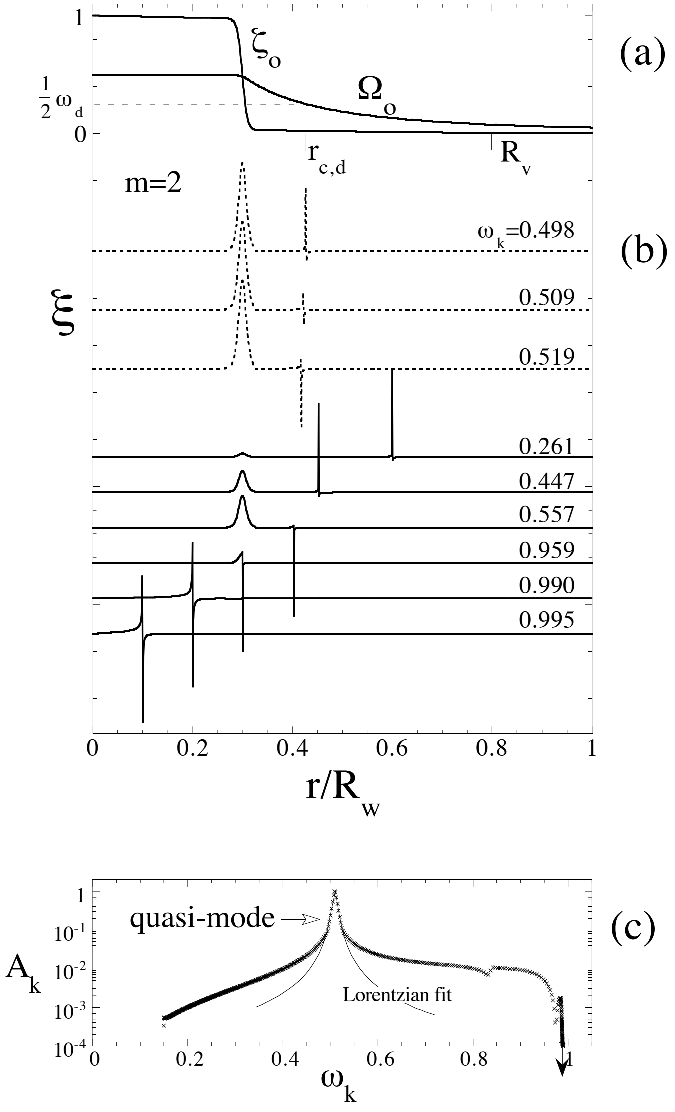

Figure 3.3: Top-Hat 2. **(a)** Equilibrium profile; $r_{c,d}$ and ω_d denote the frequency and critical radius of the $m = 2$ discrete mode of Top-Hat 1. **(b)** $m = 2$ eigenfunctions (eigenvectors of the matrix M). All eigenfunctions are zero at $r = 0$. The dashed curves correspond to exceptional eigenmodes. **(c)** Expansion coefficients A_k for the discrete eigenfunction ξ_d of Top-Hat 1, expanded in the continuum eigenfunctions of Top-Hat 2.

A Lorentzian distribution gives an accurate description of the peak,

$$A_k \sim \frac{1}{(\omega_k - \omega_q)^2 + \gamma^2} \tag{3.35}$$

A least-squares fit in the peak region (solid line) gives $\omega_q = 0.509$ and $\gamma = 5 \times 10^{-3}$. Note that the central eigenfrequency ω_q is slightly greater than the eigenfrequency of the original discrete mode ($\omega_d = 0.496$).

As the continuum modes disperse, their superposition will behave like an exponentially damped version of the original discrete mode. To see this, first recall that the eigenfunctions $\{\xi_k\}$ of the exceptional continuum modes are roughly equivalent to the eigenfunction ξ_d of the original discrete mode, for $r \lesssim r_{c,d} = 0.42$. Second, the sharp peak in A_k involves only these exceptional continuum modes. Consequently, for $r \lesssim .42$, the eigenmode expansion [Eq. (3.18)] of the excitation simplifies to

$$\delta\zeta(r,t) \approx \xi_d(r) \sum_k A_k e^{-i\omega_k t}. \tag{3.36}$$

Substituting the Lorentzian form of A_k [Eq. (3.35)] into Eq. (3.36), we obtain the desired result: $\delta\zeta \sim \xi_d(r) e^{-(\gamma + i\omega_q)t}$ for $r \lesssim 0.42$.

As a final remark, quasi-modes (like discrete modes) exist on vortices of all kinds. Here, we have focused on a top-hat vortex, in which case the radial eigenfunction of the quasi-mode has a single sharp peak. The main reason for giving this example is to make clear the connection between quasi-modes and the discrete modes of a uniform vortex-patch [92]. However, on different vortices, quasi-modes can have broad "eigenfunctions" with multiple peaks: the variety of quasi-modes is infinite, just as the variety of discrete modes is infinite.

3.4 Eigenmode Excitability

In this section, we determine how the eigenmodes respond to an external impulse. These results are used in the next section to examine the linear evolution of impulse-generated perturbations. We focus on 2D fluid experiments with strongly magnetized electron columns. These experiments were discussed briefly in the introduction (Fig. 3.1) of this chapter.

3.4.1 2D Fluid Experiments with Strongly Magnetized Electron Columns

The experiment consists of a long column of electrons in a uniform axial magnetic field [8]. A diagram of the experimental apparatus is shown in Fig. 3.4. The electrons are enclosed by a hollow cylindrical conductor. Large DC voltages are applied on rings at both ends of the cylinder to keep the electrons from escaping in the axial direction. The strong (1 Tesla) magnetic field $B\hat{z}$ counters the outward radial force of the electric field ($\vec{E}$), and prevents the electrons from escaping to the wall.

In these experiments, the time period over which electrons bounce from one end of the trap to the other (along the z-axis) is much less than the characteristic time scale for the flow of electrons in the r-θ plane (i.e. an eddy turn-over time).

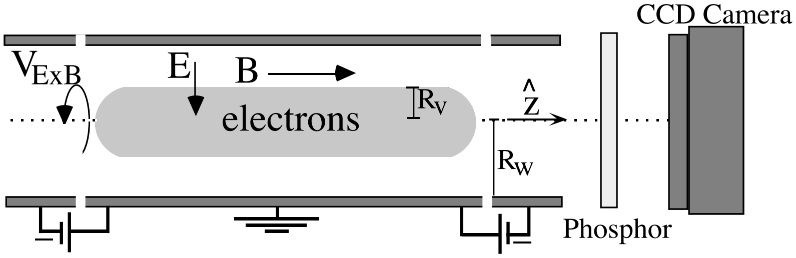

Figure 3.4: Side view of a Penning-Malmberg apparatus that is used for studying 2D Euler Dynamics.

As a result, the “instantaneous” r-θ velocity of an electron can be approximated by its average velocity over a bounce period. The 2D fluid equations obtained from this bounce-averaging scheme are known as the drift-Poisson equations [48],

$$\begin{aligned} &(a)\ \ \partial n/\partial t + \vec{v}\cdot\nabla n = 0,\\ &(b)\ \ \vec{v} = \hat{z}\times c\nabla\phi/B, \qquad (3.37)\\ &(c)\ \ \nabla^2\phi = 4\pi e n. \end{aligned}$$

Above, $\vec{v}(r,\theta,t)$ is the $\vec{E}\times\vec{B}$ drift velocity field, $n(r,\theta,t)$ is the z-averaged electron density, and $\phi(r,\theta,t)$ is the electrostatic potential. The boundary condition is $\phi = 0$ at R_w, since the wall of the trap is grounded.

The equations for the vorticity of the r-θ flow can be obtained directly from Eq. (3.37). They are the 2D Euler equations [Eq. (3.1)]. The stream function relates to the electrostatic potential by the the relation $\psi \equiv c\phi/B$, and the vorticity relates to the electron density by the equation $\zeta = 4\pi ecn/B$. The vacuum between the electron column and the conducting wall corresponds to a region of zero vorticity. The boundary condition $\phi = 0$ at the conducting wall corresponds to free-slip at the wall of a circular container.

Because ζ is proportional to n, vorticity measurements are (theoretically) equivalent to density measurements [8]. Thus, vorticity is measured by dumping the electrons onto a phosphor screen, and recording the density (vorticity) image with a CCD camera [8]. Although this imaging is destructive, the initial conditions are reproducible, so that the time evolution of flows can be studied.

The experiments start with a symmetric monotonic vortex of electrons. An external electric field is then applied for a short time. The electric field varies with both r and θ, and deforms the vortex. We now calculate the eigenmode expansion of this vorticity perturbation.

3.4.2 Eigenmode Excitability and the Reciprocity Principle

In order to determine the extent to which each eigenmode is excited by an external impulse, it is convenient to break the stream function perturbation into an "internal" part and an "external" part:

$$\delta\psi^{(m)}(r,t) = \delta\psi^{(m)}_{int}(r,t) + \delta\psi^{(m)}_{ext}(r,t). \tag{3.38}$$

The internal part is due to the vorticity perturbation $\delta\zeta$ inside the vortex. Specifically, the internal part is the following integral of vorticity:

$$\delta\psi_{int}(r,t) = \int_0^{R_v} dr' r' G_m(r|r')\delta\zeta(r',t). \tag{3.39}$$

Here, $G_m(r|r')$ is the Green's function given by Eq. (3.10), and we have suppressed the superscript '(m)' to avoid cumbersome notation. The "external" stream function corresponds to the electric field that is is applied briefly in the experiments to deform the vortex. The source of $\delta\psi_{ext}$ is at the wall radius R_w. So, $\delta\psi_{ext}$ satisfies Laplace's equation for $r < R_w$, and has the form

$$\delta\psi_{ext}(r,t) = f(t)\left(\frac{r}{R_w}\right)^m. \tag{3.40}$$

The linearized Euler equation for the evolution of vorticity is given below:

$$\frac{\partial\delta\zeta}{\partial t} + im\Omega_o(r)\delta\zeta - \frac{im}{r}\left(\delta\psi_{ext} + \delta\psi_{int}\right)\zeta_o' = 0. \tag{3.41}$$

Substituting Eq. (3.39) and Eq. (3.40) into Eq. (3.41), we obtain

$$\frac{\partial\delta\zeta}{\partial t} + iI\left[\delta\zeta\right] = \frac{im}{(R_w)^m}\, f(t)\; r^{m-1}\zeta_o'. \tag{3.42}$$

Here, I is the integral operator defined previously in Eq. (3.13).

The vorticity perturbation $\delta\zeta$ can be expanded in the eigenfunctions of I,

$$\delta\zeta(r,t) = \sum_k a_k(t)\xi_k(r). \tag{3.43}$$

Here, '$\sum_k$' is a formal sum that includes an integral over the continuum modes plus the discrete mode. We use a "discrete" notation since in practice our expansion is numerical. Substituting Eq. (3.43) into Eq. (3.42) gives a first order ODE for the time evolution of a_k,

$$\frac{da_k}{dt} + i\omega_k a_k = -\frac{im}{(R_w)^m} X_k f(t). \tag{3.44}$$

In Eq. (3.44), X_k denotes the eigenmode "excitability", which is defined by the equation

$$X_k \equiv -\frac{\langle \xi_k, r^{m-1}\zeta_o' \rangle}{\langle \xi_k, \xi_k \rangle} = \frac{\displaystyle\int_0^{R_v} r^{m+1}\xi_k(r)dr}{\langle \xi_k, \xi_k \rangle}. \tag{3.45}$$

For the second equality, we have used Eq. (3.23), which defines the inner product.

Equation (3.44) can be solved easily for general $f(t)$:

$$a_k(t) = -\frac{im}{(R_w)^m} X_k \, e^{-i\omega_k t} \int_0^t dt' f(t') e^{i\omega_k t'}. \tag{3.46}$$

We are concerned only with times t after the impulse, during which the perturbation is free to relax. Since the forcing function f vanishes after the impulse, and before $t = 0$, the upper and lower limits of integration in Eq. (3.46) can be set to positive and negative infinity. Thus, Eq. (3.46) reduces to

$$a_k(t) = -\frac{im}{(R_w)^m} X_k F_k^* \, e^{-i\omega_k t}, \tag{3.47}$$

where F_k^* is the complex conjugate of the Fourier transform of $f(t)$, evaluated at ω_k.

In the experiments with electron columns, the electric impulse is typically applied over a time interval much less than the turnover time of the vortex ($\sim 2\pi/\Omega_o$). It is therefore reasonable to approximate the applied flow field as a delta-function impulse of strength ε, i.e. $f(t) = \varepsilon\delta(t)$. Then, $F_k^* = \varepsilon$ for all ω_k and Eq. (3.47) yields

$$a_k(t) = -\frac{im\varepsilon}{(R_w)^m} X_k \, e^{-i\omega_k t}. \tag{3.48}$$

It is of interest to note that the excitability X_k is proportional to the (normalized) multipole moment of the eigenmode. We define the m^{th} multipole moment of a vorticity perturbation by the equation

$$Q^{(m)}(t) \equiv \int_0^{R_v} dr\, r^{m+1} \delta\zeta^{(m)}(r,t). \tag{3.49}$$

For an eigenmode, we have $\delta\zeta \propto \xi_k$.

The amplitude of the multipole moment measures the influence of the vorticity perturbation on the external flow. This is because $\delta\psi^{(m)}$ varies like $Q^{(m)}/r^m$ for $r > R_v$ (when there is no wall). Since the eigenmode excitability X_k is proportional to the (normalized) multipole moment of the eigenmode, the system exhibits reciprocity: the eigenmodes with the strongest influence on the external flow are also the most sensitive to a brief flow field that is created by an external source.

3.5 The Inviscid Damping of Impulse-Generated Perturbations

In this section, we examine the linear response of a monotonic vortex to an external, $m = 2$, $\delta(t)$ impulse. After the impulse, the quadrupole moment of the perturbation generally oscillates at a frequency ω_q, and decays at an exponential rate γ. Both ω_q and γ are given by a Landau pole of the equilibrium profile.

As the quadrupole moment decays exponentially, the vorticity perturbation can behave like a damped mode (i.e. a quasi-mode), or undergo a more complicated evolution that involves spiral wind-up [88, 93, 89, 94]. We will demonstrate that the vorticity perturbation is a damped quasi-mode when $\gamma/\omega_q << 1$, and that spiral wind-up occurs when $\gamma/\omega_q \sim 1$.

3.5.1 The Excitation of a Quasi-Mode on a Top-Hat Vortex

We first examine the response of Top-Hat 2. The equilibrium profile and the eigenmodes of this vortex are shown in Fig. 3.3. Suppose that at time $t = 0$ the vortex is perturbed by an $m = 2$, $\delta(t)$ impulse, as described in the previous section. Figure 3.5.a shows the excitability spectrum X_k, which gives the amplitude of each eigenmode after the impulse. The excitability spectrum is sharply peaked near the exceptional continuum modes of the vortex (dashed modes in Fig. 3.3). In fact, this peak has the same Lorentzian structure (solid line) as the quasi-mode perturbation that was described in Section 3.3 [Eq. (3.35)].

We now demonstrate that this excitation behaves like an exponentially damped mode, as we explained it should in Section 3. Figure 3.5.b shows the vorticity perturbation at $T = 0$ and at $T = 30$ rotation periods. During this time interval, the vorticity perturbation (for $r \lesssim .33$) rotates with constant phase velocity and decays an order of magnitude.

Figure 6 shows the evolution of the perturbation's quadrupole moment $Q^{(2)}(t)$ on a log-linear plot. The initial decay is exponential, and a least-squares fit to the early time data gives a decay rate of $\gamma = 5 \times 10^{-3}$. This decay rate agrees with our earlier prediction that was obtained by fitting the expansion coefficients of the quasi-mode to a Lorentzian function of ω_k [Eq. (3.35)].

We now compare the observed decay rate of the quasi-mode to the decay rate given by the Landau pole of the equilibrium profile. The Landau pole for a Top-Hat vortex was calculated analytically by Briggs, Daugherty and Levy [48]. This Landau pole has the following decay rate:

$$\gamma_{BDL} \approx \frac{-\pi}{4m} r_o \zeta_o'(r_*) \left(\frac{r_o}{r_*}\right)^{2m-3} \left[1 - \left(\frac{r_*}{R_w}\right)^{2m}\right]^2 . \tag{3.50}$$

Here, r_o is the radius where $|\zeta_o'(r)|$ is maximal, and r_* is given by Eq. (3.33).

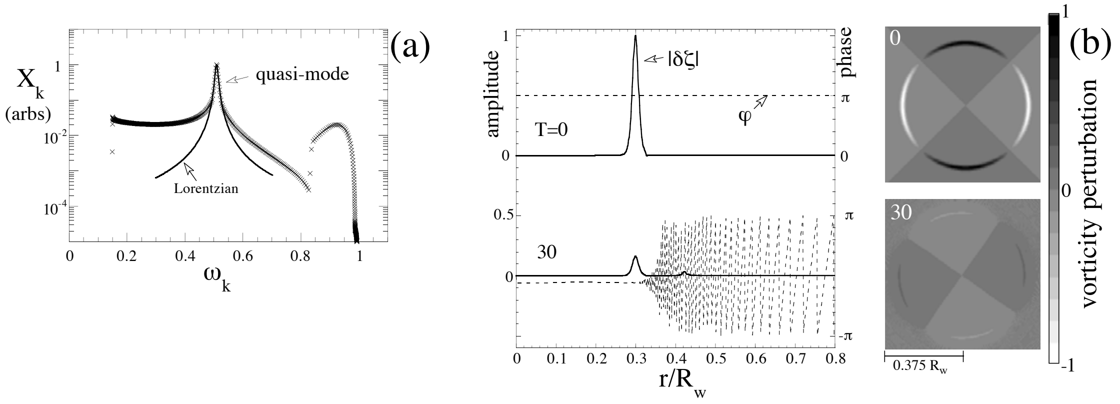

Figure 3.5: The excitation and decay of an $m = 2$ quasi-mode on Top-Hat 2. **(a)** The excitability spectrum. The solid line corresponds to the Lorentzian fit of the quasi-mode's frequency spectrum, which was obtained in Section 3.3.3. **(b)** The vorticity perturbation at $T = 0$ and at $T = 30$ rotation periods. The left graph in (b) shows the amplitude (solid line) and phase (dashed line) of the Fourier coefficient $\delta\zeta = |\delta\zeta|e^{i\varphi}$. The right figures in (b) are contour plots of $\Delta\zeta$ in the plane of the vortex.

Note that r_* is the critical radius of a Kelvin mode on a uniform vortex patch that extends out to r_o [Eq. (3.30)]. The actual critical radius of the quasi-mode approximately equals r_*.

The dashed line in Fig. 3.6 corresponds to the exponential decay that is given solely by the Landau pole [Eq. (3.50)]. Clearly, the Landau pole gives the correct decay rate of an impulse-generated perturbation on a top-hat vortex. It is worth noting that the decay rate γ_{BDL} is proportional to the vorticity gradient at the critical radius. This indicates that the damping is due to a resonant interaction with co-rotating fluid. A qualitative explanation of this resonance damping is given in Appendix I.

There are two notable features that distinguish the quasi-mode from a genuine exponentially damped eigenmode. First, $Q^{(2)}$ makes a transition toward algebraic decay at approximately 100 rotation periods. Second, as the original vorticity perturbation decays, a smaller perturbation grows in a thin layer about the critical radius. Eventually, the amplitude of this smaller perturbation saturates, but its phase continues to evolve.

The structure of this bump is analytically tractable. During its growth, the stream function is approximately that of a Kelvin mode at r_o that is exponentially damped,

$$\Delta\psi \approx -im\varepsilon \left(\frac{r_o}{R_w}\right)^m \zeta_o(0) G_m(r|r_o) e^{-(\gamma_{BDL}+i\omega_*)t} e^{im\theta} + c.c. \tag{3.51}$$

Here, G_m is the Green's function defined by Eq. (3.10), $\zeta_o(0)$ is the equilibrium vorticity at $r = 0$, ω_* is defined in Eq. (3.32) and γ_{BDL} is defined in Eq. (3.50). The amplitude of the stream function depends on the strength of the impulse that created the initial perturbation, $\delta\psi_{ext} = \varepsilon\delta(t)\left(\frac{r}{R_w}\right)^m$.

Substituting Eq. (3.51) into the linearized Euler equation for the evolution of vorticity [Eq. (3.3)], it is simple to show that, near the critical radius,

$$\lim_{t \to \infty} |\delta\zeta| = -\frac{1}{2} \frac{|\varepsilon| \zeta_o'(r_*) \left(\frac{r_o}{R_w}\right)^m \left(\frac{r_o}{r_*}\right)^{m-2} \left[1 - \left(\frac{r_*}{R_w}\right)^{2m}\right]}{\sqrt{\left(\frac{\gamma_{BDL}\, r_*^3}{m\zeta_o(0) r_o^2}\right)^2 + (r - r_*)^2}}. \tag{3.52}$$

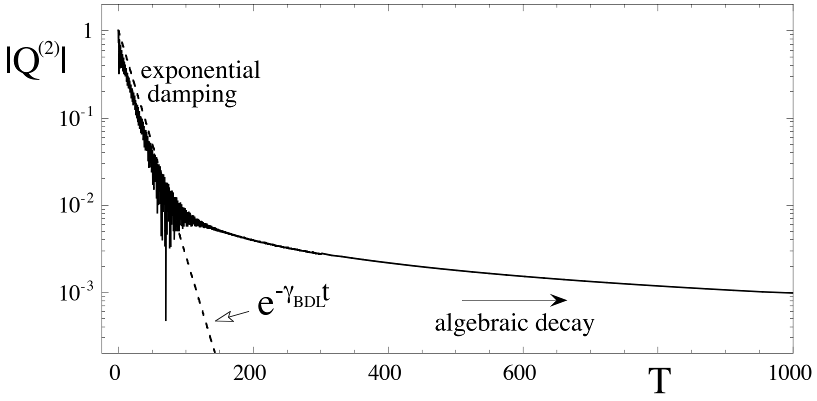

Figure 3.6: Evolution of the quadrupole moment of Top-Hat 2 after an external impulse. The dashed line indicates exponential damping, with decay rate given by Eq. (3.50).

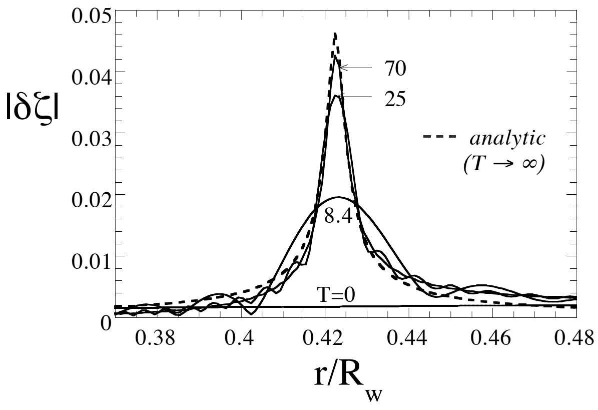

Figure 3.7: Growth of $|\delta\zeta|$ in the critical layer.

Equation (3.52) indicates that the width of the bump is proportional to the decay rate $\gamma \approx \gamma_{BDL}$ of the quasi-mode. This relationship is simple to understand when the quasi-mode is viewed as a wave-packet of continuum modes. The decay rate γ is the peak-width of the wave-packet's frequency spectrum, X_k. The peak-width defines a critical layer in the vortex, where the continuum modes are resonant with the fluid rotation and have singular spikes: the thickness of this critical layer is proportional to γ. As the continuum modes disperse, the singular spikes unravel, forming a bump across the critical layer.

Equation (3.52) is compared to the numerical solution in Fig. 3.7, for the case where $\zeta_o'(r_*) = 6.07 \times 10^{-2}\zeta_o(0)/R_w$. There is good agreement between the two, and we find that the agreement improves as $\zeta_o'(r_*)$ decreases.

We have seen that an external impulse excites a quasi-mode on a top-hat vortex, and we have studied the evolution of this quasi-mode in detail. We now explain why the quasi-mode is excited. The simplest explanation is obtained in the limit of zero vorticity gradient in the critical layer, in which case the quasi-mode is actually an undamped discrete mode.

Figure 3.8.a shows the excitability spectrum X_k of an impulse-generated perturbation on Top-Hat 1 (Fig. 3.2). Top-Hat 1 has zero gradient in the criti-

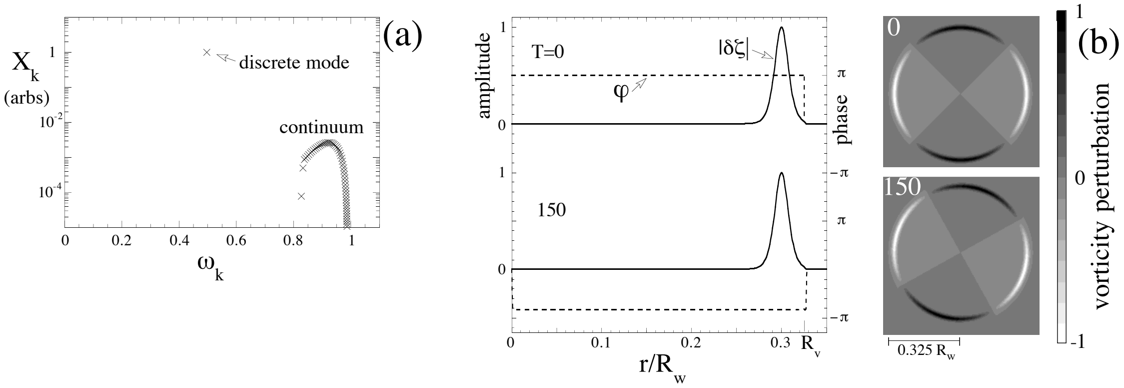

Figure 3.8: The excitation of an $m = 2$ discrete mode on Top-Hat 1. **(a)** The excitability spectrum. **(b)** The vorticity perturbation at $T = 0$ and at $T = 150$ rotation periods. The left graph in (b) is the amplitude (solid line) and phase (dashed line) of the Fourier coefficient, $\delta\zeta = |\delta\zeta|e^{i\varphi}$. The right figures in (b) are contour plots of $\Delta\zeta$ in the plane of the flow.

cal layer, and therefore supports a discrete mode. The discrete mode is excited approximately $2\frac{1}{2}$ orders of magnitude higher than any of the continuum modes. Figure 3.8.b verifies that the excitation behaves as though it consists only of a discrete eigenmode. The vorticity perturbation is plotted at $T = 0$ and at $T = 150$. The phase of the perturbation remains uniform in r (increasing linearly with time), and the amplitude remains constant.

The discrete mode is excited far above the continuum, because its eigenfunction $\xi_d(r)$ [Eq. (3.34)] is approximately the same as the initial state of the impulse-generated perturbation, $\delta\zeta(r, 0) \propto r^{m-1}\zeta_o'(r)$. By orthogonality, the continuum eigenfunctions have a much smaller overlap with the initial perturbation. Physically, the discrete mode dominates the excitation because its multipole moment is much greater than the multipole moments of the continuum modes, which tend to be self-shielding. By reciprocity, the discrete mode is much more sensitive to an external impulse than any of the continuum modes.

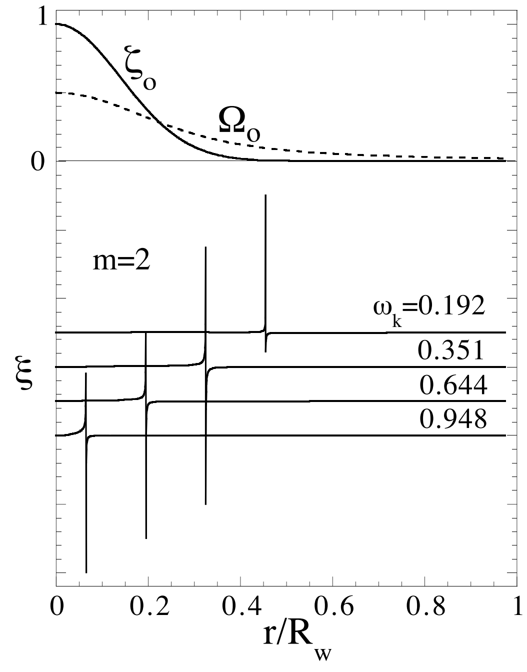

Figure 3.9: Gaussian vortex. Equilibrium profile and $m = 2$ eigenfunctions (eigenvectors of the matrix M). All eigenfunctions are zero at $r = 0$.

3.5.2 The Excitation of a Gaussian Vortex

Figure 3.9 shows the equilibrium profile of a Gaussian vortex,

$$\zeta_o(r) = e^{-\left(\frac{5r}{R_w}\right)^2}. \tag{3.53}$$

Here, the Gaussian extends to $r = .975R_w$, beyond which ζ_o is constant. Below the equilibrium profile is a selection of the Gaussian's $m = 2$ eigenfunctions $\{\xi_k\}$. There are no discrete modes, and there is no small group of continuum modes that seem more exceptional than the others. We now examine the linear response of this Gaussian to an externally applied, $m = 2$, $\delta(t)$ impulse.

Figure 10 shows how the quadrupole moment evolves after the impulse is applied to the Gaussian. Before 10 rotation periods, the quadrupole moment oscillates with a constant frequency and decays four orders of magnitude, at an exponential rate. After 10 rotation periods, the frequency decreases and $Q^{(2)}$ begins to decay at a much slower rate.

Also shown in Fig. 3.10 is the evolution of the quadrupole moment, were it given solely by a Landau pole of the equilibrium profile (dashed lines). For a Gaussian profile, Eq. (3.50) is no longer a good approximation to the imaginary frequency of the Landau pole. Instead, the Landau pole was calculated numerically using the method of Spencer and Rasband. This calculation is outlined in Appendix III. The Landau pole gives a frequency $\omega_q = 0.226$ and a decay rate $\gamma = 0.079$. It is clear from Fig. 3.10 that there is excellent agreement between pure Landau damping and the initial decay that is given by the full eigenmode expansion.

However, the excitation does not fit our definition of a quasi-mode: the *vorticity* perturbation is at no place and at no time closely approximated by a function of the form $z(r)e^{-\gamma t}e^{i(m\theta-\omega_q t)}$. Instead, the vorticity perturbation under-

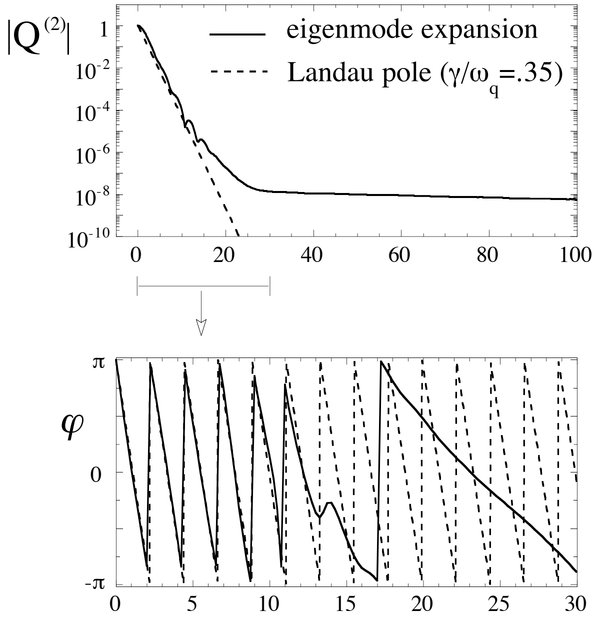

Figure 3.10: Evolution of the quadrupole moment of a Gaussian vortex after an external impulse ($Q^{(2)} = |Q^{(2)}|e^{i\varphi}$). The dashed lines correspond to the evolution that is given solely by the Landau pole.

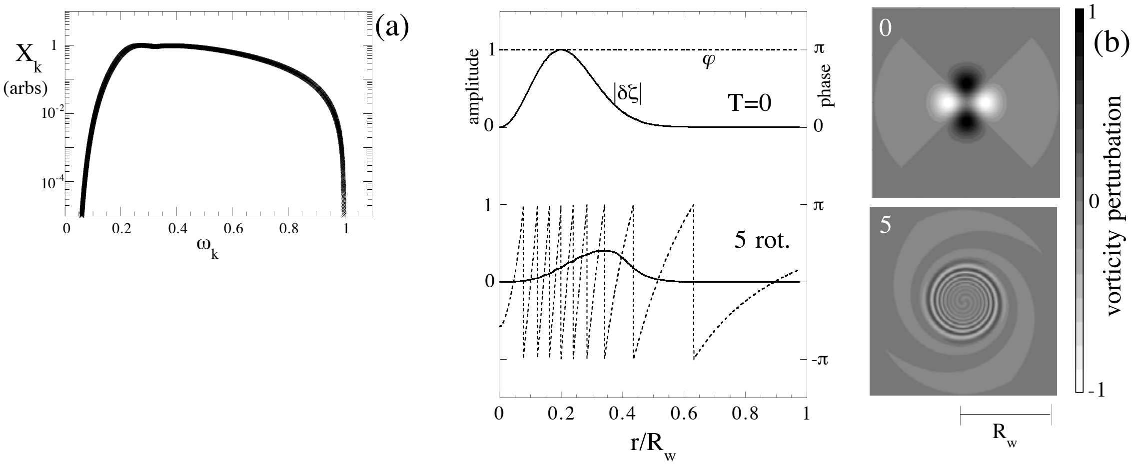

Figure 3.11: Response of the Gaussian to an external impulse. **(a)** The excitability spectrum. **(b)** The vorticity perturbation at $T = 0$ and at $T = 5$ rotation periods. The left graph in (b) shows the amplitude (solid line) and phase (dashed line) of the Fourier coefficient $\delta\zeta = |\delta\zeta|e^{i\varphi}$. The right figures in (b) are contour plots of $\Delta\zeta$ in the plane of the flow.

goes a complicated evolution that includes the formation of thin striations across the entire vortex (spiral wind-up). This can be seen in Fig. 3.11.b, which shows the amplitude and phase of the vorticity perturbation at $T = 0$ and at $T = 5$.

Global filamentation of vorticity is characteristic of strongly damped ($\gamma/\omega_q \sim 1$) excitations. Strong damping implies a broad peak in the frequency spectrum of the excitation. This broad peak is evident in Fig. 3.11.a, which shows the excitability X_k as a function of ω_k. The continuum modes in the peak region have critical radii than span a large portion of the vortex. As the continuum modes disperse, their singular spikes at the critical radii unravel. This accounts for the observed filamentation across the vortex.

We now demonstrate that exponential damping can be removed on a Gaussian by setting ζ_o' equal to zero at the critical radius of the Landau pole. By setting ζ_o' equal to zero at the critical radius, we remove the mechanism for resonant damping. Therefore, a discrete mode should appear in the eigenspectrum. Figure 3.12.a shows the partially flattened Gaussian. Directly below the equilibrium profile is the eigenfunction of the expected discrete mode.

The critical radius of this discrete mode lies inside the flattened layer, and its eigenfrequency is degenerate with the continuum. This degeneracy can occur because the vortex is not strictly monotonic. However, we are justified in calling the mode "discrete" for the following two reasons: (1) it has no singular spike at its critical radius, and (2) it corresponds to a discrete point in the excitability spectrum (Fig. 3.12.b). In contrast, all continuum modes have singular spikes. Furthermore the continuum modes with critical radii in the region of zero vorticity gradient have exactly zero excitability ($X_k = 0$). Physically, these continuum modes are not excitable because they correspond to vorticity perturbations where

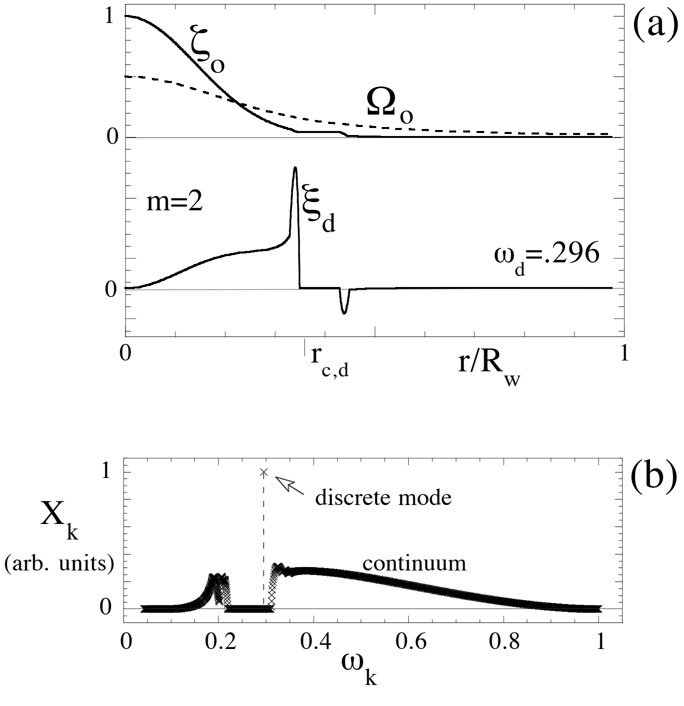

Figure 3.12: Gaussian vortex with a flat interval. **(a)** Equilibrium profile and the $m = 2$ discrete mode. **(b)** Excitability of the $m = 2$ eigenmodes.

ζ_o' equals zero, and the application of an incompressible flow field can not produce a (linear) vorticity perturbation where ζ_o' equals zero.

3.6 Comparison of Linear Theory to Experiments

In the introduction, we mentioned that exponential decay is commonly observed in 2D fluid experiments with magnetized electron columns (e.g. Fig. 3.1). This behaviour is consistent with the linear response theory of Section 3.5, which gave exponential decay for both Top-Hat and Gaussian vortices. We now directly compare linear response theory to the early evolution of the experimental vortices. We find that the exponential decay predicted by linear theory is in good agreement with the experiments.

We examine two experimental vortices, which are both shown in Fig. 3.13. Here, the '+' markers are experimental data, and the solid lines are analytic functions that approximate the equilibrium profiles. These analytic functions are used to calculate the Landau poles of the vortices. Note that Fig. 3.13.b corresponds to the vortex in Fig. 3.1.

In the experiments, the vortices (electron columns) are perturbed by an asymmetric electrostatic potential, applied to the wall for a short time interval, as described in Section 3.4. The applied potential is dominated by the $m = 2$ azimuthal wave-number, and therefore deforms the vortex into an ellipse.

Figure 3.14 shows how the quadrupole moments evolve in both experiments. The X's correspond to the experimental data. The diamonds give the predicted linear evolution. Here, linear theory is calculated by expanding the the initial vorticity perturbation in continuum modes. Specifically, each eigenmode evolves according to Eq. (3.48), which assumes that the perturbation was generated by a $\delta(t)$ impulse.

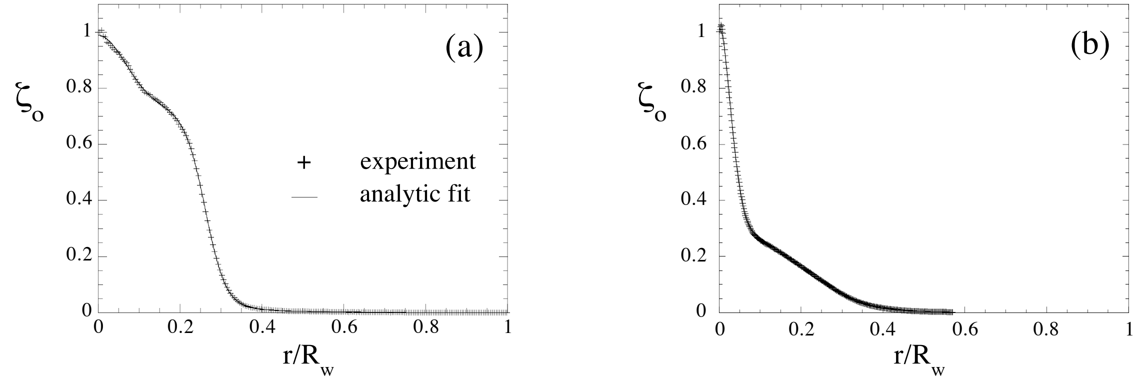

Figure 3.13: Equilibrium profiles for two experimental vortices. The profile in (b) corresponds to the vortex in Fig. 3.1.

In both experiments, linear response theory is in good agreement with the initial evolution of the quadrupole moment. Furthermore, in both experiments, $Q^{(2)}(t)$ behaves like an exponentially damped mode, with frequency ω_q and decay rate γ. We note that in Figure 3.14.b, there is some discrepancy between the experimental value of ω_q and linear theory. This frequency difference may indicate that the early evolution in the experiment is slightly nonlinear. Another possibility is that a $\delta(t)$ impulse approximation is not sufficiently accurate.

As expected from Section 3.5, ω_q and γ are given by Landau poles of the equilibrium profiles. To obtain a Landau pole of an experimental vortex requires an analytic continuation of $\zeta_o(r)$ in the complex r-plane (see Appendix III, or Refs. [48, 49, 50]). To obtain this continuation, we approximate the experimental profile with a combination of analytic functions, such as Gaussians, hyperbolic tangents and polynomials. To obtain a Landau pole also requires a continuation of $\Omega_o(r)$. This continuation is obtained from Eq. (3.5), which says that $\Omega_o(r)$ is proportional to the integral of $r\zeta_o(r)$. Of course, the integral is now in the complex plane. The

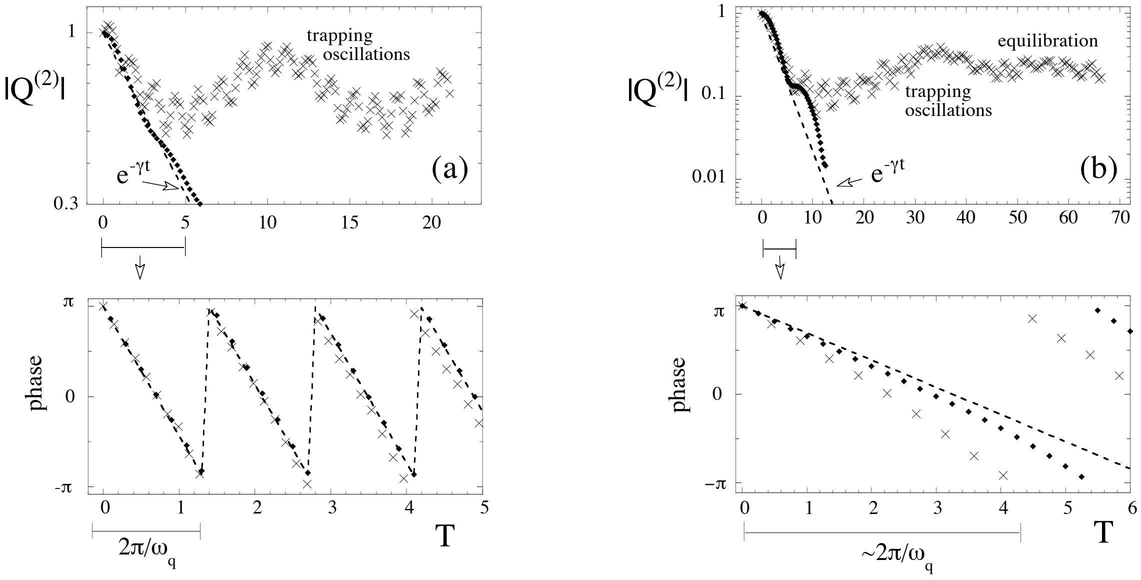

Figure 3.14: Evolution of $Q^{(2)}$ in two typical experiments. The equilibrium profiles for experiments (a) and (b) are shown in Figs. 3.13.a and 3.13.b, respectively. The X's are experimental data. The diamonds correspond to linear response theory. The dashed lines show the evolutions that are given solely by the Landau poles. In both (a) and (b), $|Q^{(2)}|$ is normalized to its initial value.

solid lines in Fig. 3.13 show our analytic approximations (evaluated on the real r-axis) of $\zeta_o(r)$ for both experiments. Using these analytic approximations, we obtain the following Landau poles. For experiment (a), the Landau pole is $\omega_q = 0.35$, $\gamma = 0.018$. For experiment (b), the Landau pole is $\omega_q = 0.077$, $\gamma = 0.030$.

The dashed lines in Fig. 3.14 are the Landau pole contributions to $Q^{(2)}(t)$. These contributions vary with time exactly like $e^{-\gamma t}e^{-i\omega_q t}$. It is apparent from Fig. 3.14 that the Landau pole contribution provides a good approximation for the initial evolution of $Q^{(2)}$ in both experiments.

After about 5 rotation periods, the experiments diverge from linear theory, and the amplitude of $Q^{(2)}$ begins to oscillate. These nonlinear oscillations are due to mixing of trapped vorticity at the critical radius r_c. Eventually the amplitude becomes constant, as the vortex relaxes to a rotating "cat's eyes" equilibrium (e.g. Fig. 3.1.a, far right).

The nonlinear stages of the vortex evolution are beyond the scope of this thesis. However, we mention that the linear stage can be made arbitrarily long by decreasing the amplitude of the initial perturbation [11, 43, 48].

3.7 The Role of the Landau Pole in Non-Impulse-Generated Perturbations

3.7.1 The Early and Intermediate Evolution of the Multipole Moment

Linear perturbations that are not generated by an external impulse do not necessarily have an early or intermediate stage of exponential decay, given by a Landau pole. This becomes clear if one puts the origin of time after the transition toward algebraic decay that was observed in the previous section (e.g. Fig. 3.6). Here, we examine whether exponential decay is common (in a practical sense) to arbitrary perturbations, or special to excitations that are generated by an external impulse. We will demonstrate that exponential decay, given by a Landau pole, is common when the Landau pole satisfies $\gamma/\omega_q << 1$, but rare when $\gamma/\omega_q \sim 1$.

We first consider decay on Top-Hat 2 (Fig. 3.3), which supports a weakly damped ($\gamma/\omega_q << 1$) quasi-mode. Figure 3.15.a shows the amplitude of $Q^{(2)}$ as a function of time for a variety of $m = 2$ perturbations on Top-Hat 2. Curve A serves as a reference for the exponential decay of a quasi-mode that is excited by an external impulse at time $t = 0$. The dashed lines correspond to exponential decay at the rate given by the Landau pole, Eq. (3.50).

Curves B-D correspond to initial perturbations that each have a single peak in a thin strip (of width $\lambda = 0.04$):

$$\delta\zeta(r,0) \propto \begin{cases} 1 + cos\left[\frac{2\pi}{\lambda}(r-d)\right] & |r-d| < \lambda/2 \\ 0 & |r-d| \geq \lambda/2. \end{cases} \tag{3.54}$$

The values of d (the center of the peak) for curves B, C and D are 0.1, 0.43 and 0.6 respectively. Curve E corresponds to an initial vorticity perturbation that increases linearly with r until dropping rapidly to zero at R_v,

$$\delta\zeta(r,0) \propto \begin{cases} r \cdot \left[1 - e^{100\frac{r-R_v}{R_v}}\right] & r < R_v \\ 0 & r \geq R_v. \end{cases} \tag{3.55}$$

Finally, curve F gives the evolution of a complex ripple,

$$\delta\zeta(r,0) \propto \begin{cases} sin^2\left(\frac{10\pi r}{0.3}\right) e^{i\frac{40\pi}{0.3}} & r < L \\ 0 & r \geq L, \end{cases} \tag{3.56}$$

with L=0.6.

In E and F, there are no clear signs of a quasi-mode or exponential decay. On the other hand, the quasi-mode contributes to an intermediate stage of D, as indicated by the dashed line. Moreover, the quasi-mode dominates two or more decades of decay in A, B and C. Note that in C, the initial bump, centered at the critical radius, resonantly drives the quasi-mode for a short period of time, increasing the amplitude of the quadrupole moment by a factor of five. Thus, the weakly damped ($\gamma/\omega_q << 1$) quasi-mode plays an important role in the evolution of most of the perturbations considered here.

When considering similar perturbations on a Gaussian vortex (Fig. 3.9), we find that exponential decay, given by a Landau pole, is less common. Figure 3.15.b shows the evolution of the quadrupole moment as a function of time for a variety of $m = 2$ initial conditions. Curve A serves as a reference for the exponential decay of a perturbation that is excited by an external impulse at time $t = 0$. The dashed line corresponds to exponential decay, at a rate given by the Landau pole,

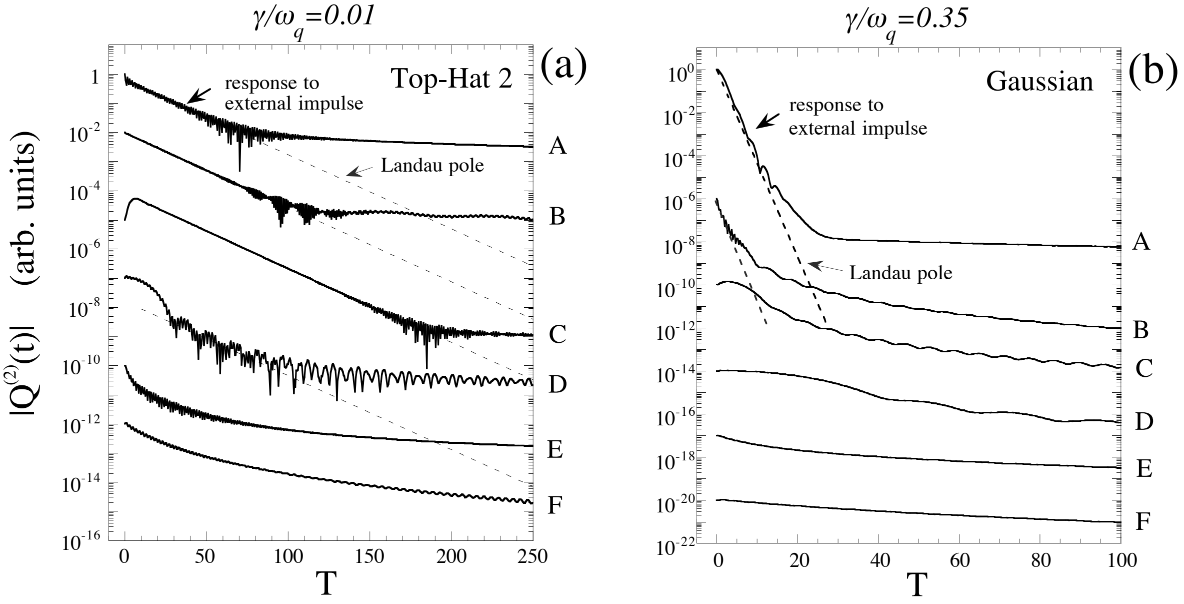

Figure 3.15: Evolution of the quadrupole moments for arbitrary $m = 2$ perturbations on **(a)** Top-Hat 2 and **(b)** a Gaussian vortex. The dashed lines show the damping of $Q^{(2)}$ determined by the Landau poles, with $\gamma = 5 \times 10^{-3}\zeta_o(0)$ in (a) and $\gamma = 7.9 \times 10^{-2}\zeta_o(0)$ in (b).

which was determined numerically (see Appendix III). Curves B-D correspond to initial conditions that are given by Eq. (3.54), with $\lambda = 0.08$. The values of d for curves B, C and D are 0.05, 0.42 (the critical radius) and 0.65 respectively. Curve E corresponds to an initial condition that increases linearly with r [Eq. (3.55)]. Curve F shows the decay of a complex ripple [Eq. (3.56), with $L = 0.6$].

Besides A, only curve B shows a possible stage of exponential damping. Thus, it appears that when $\gamma/\omega \sim 1$, the Landau pole plays a lesser role in the evolution of arbitrary perturbations.

3.7.2 Late-Time Decay

Even when the Landau pole has some role in the early stages of inviscid decay, exponential damping eventually succumbs to algebraic decay. Late-time algebraic decay is well known from various analyses [48, 88, 89, 90, 91]. Here, we use eigenmode theory to construct a simple proof that the multipole moment decays algebraically in the late-time limit. We assume only that there are no discrete modes, that the continuum has a finite frequency range, and that the Fourier transform of $Q^{(m)}(t)$ has no singularities.

If there exist no discrete modes, then the multipole moment can be written as a finite Fourier integral over the continuum,

$$Q(t) = \int_{\omega_{min}}^{\omega_{max}} d\omega \tilde{Q}(\omega) e^{-i\omega t}. \tag{3.57}$$

Here, $\omega_{max} \equiv m\Omega_o(0)$ and $\omega_{min} = m\Omega_o(R_v)$. For convenience, we have dropped the superscript (m) on the multipole moment.

Assuming that $\tilde{Q}(\omega)$ is a smooth function of ω, Eq. (3.57) can be expanded using integration by parts (twice),

$$Q(t) \;=\; \frac{i}{t}\tilde{Q}(\omega)e^{-i\omega t}\Big|_{\omega_{min}}^{\omega_{max}} \;+\; \frac{1}{t^2}\cdot\left[\frac{d\tilde{Q}(\omega)}{d\omega}e^{-i\omega t}\Big|_{\omega_{min}}^{\omega_{max}} - \int_{\omega_{min}}^{\omega_{max}} d\omega \frac{d^2\tilde{Q}(\omega)}{d\omega^2}e^{-i\omega t}\right]. \tag{3.58}$$

The expression in square brackets is finite for all times so that the second term on the right-hand-side of Eq. (3.58) decays at least as fast as t^{-2}. If $Q(\omega)$ does not vanish at atleast one end point, Eq.(58) implies that $Q \sim t^{-1}$ in the late time limit; otherwise, $Q \sim t^{-n}$, where n is a positive integer greater than one.

The particular structure of $\tilde{Q}(\omega)$ determines the time scale before the leading order term dominates the expansion. A sharp peak in $\tilde{Q}(\omega)$ prevents the expansion from converging rapidly. For a quasi-mode, the velocity spectrum is approximately Lorentzian $\left(\tilde{Q}(\omega) \sim \frac{1}{(\omega-\omega_q)^2+\gamma^2}\right)$, and the period before algebraic decay is much greater than the e-folding time γ^{-1}.

3.8 Generalization of the Eigenmode Expansion to Non-Monotonic Equilibria

When the equilibrium vorticity varies non-monotonically with radius, exponentially growing and algebraic instabilities can dominate the linear evolution. The exponential instabilities are immediately apparent as eigenvalues of M with positive imaginary parts. An algebraic instability will appear as a singularity in the expansion coefficients A_k of an arbitrary perturbation. In Sections 2 and 3 we outlined a procedure for obtaining the eigenmode expansion of a perturbation on a monotonic vortex. In this section, we generalize the procedure to cover all possible equilibria.

The expansion formula is made more inclusive by introducing "right-handed" and "left-handed" eigenvectors. Let ξ_R denote an eigenvector of the real matrix M, and let ω_R denote its eigenfrequency. Furthermore, let ξ_L and ω_L denote an eigenvector and eigenfrequency of M^T, the transpose of M. ξ_R will be called a right-handed eigenvector and ξ_L will be called a left-handed eigenvector. Although M and M^T have the same set of eigenvalues, the right-handed eigenvectors do not generally equal the left-handed eigenvectors.

However, from basic linear algebra we know that ξ_L and ξ_R satisfy the following orthogonality equation:

$$\langle \xi_L, \xi_R \rangle_s = 0 \quad if \quad \omega_L \neq \omega_R^*. \tag{3.59}$$

The standard inner-product that is used in Eq. (3.59) is defined below:

$$\langle f, h \rangle_s \equiv \sum_{i=1}^{N} f^*(r_i) h(r_i). \tag{3.60}$$

In what follows, we will assume that a vorticity perturbation is well approximated by a sum over right-handed eigenmodes,

$$\Delta\zeta(r_i,\theta,t) \approx \sum_{\mathrm{m}=1}^{+\infty}\sum_{k=1}^{N} A_k^{(m)}\xi_{R,k}^{(m)}(r_i)e^{\mathrm{i}(\mathrm{m}\theta-\omega_\mathrm{k}^{(\mathrm{m})}\mathrm{t})} + c.c. \tag{3.61}$$

Equation (3.59) can be used to derive the expansion coefficients A_k. The result is given below:

$$A_k^{(m)} = \frac{\left\langle \xi_{L,k}^{(m)}, \delta\zeta^{(m)}(r,0)\right\rangle_s}{\left\langle \xi_{L,k}^{(m)}, \xi_{R,k}^{(m)}\right\rangle_s}. \tag{3.62}$$

Here $\delta\zeta^{(m)}(r,0)$ is the m^{th} Fourier coefficient of the vorticity perturbation at $t=0$, and $\xi_{L,k}$ is the eigenvector of M^T that corresponds to the eigenfrequency $\omega_{R,k}^*$.

When ζ_o' does not equal zero at any radial grid-point, the left-handed eigenvectors are proportional to the right-handed eigenvectors. Specifically, one can verify that

$$\xi_L(r_i) = \frac{r_i^2}{\zeta_o'(r_i)}\xi_R^*(r_i) \quad for \quad \omega_L = \omega_R^*. \tag{3.63}$$

When the vortex is monotonic, $\zeta_o' < 0$ for all r_i and Eq. (3.63) is valid. Then, Eq. (3.63) can be substituted into Eq. (3.62) and we arrive at our previous formula for the expansion coefficients, Eq. (3.26).

In the case of a monotonic vortex, we were able to prove that M has N linearly independent eigenvectors, where N is the order of the matrix M. We have given no proof of completeness for the general case. However, for all cases we have studied, we find that M has N linearly independent eigenvectors.

3.9 A Hollow Vortex

A simple example of a non-monotonic vortex is the hollow vortex that is shown in Fig. 3.16.a (taken directly from Ref. [95]). The radial profile of this vortex is given by the following equation:

$$\zeta_o(r) = \begin{cases} 1 + 2\left(\frac{r}{R_v}\right)^2 - 7\left(\frac{r}{R_v}\right)^4 + 4\left(\frac{r}{R_v}\right)^6 & r < R_v \\ 0 & r \geq R_v, \end{cases} \tag{3.64}$$

where $R_v = 0.6R_w$. It is well known that this vortex behaves much differently than a monotonic vortex: an arbitrary $m = 1$ perturbation will grow like $t^{1/2}$, and perturbations with $m \geq 2$ will grow exponentially.

However, there is some concern that discretization can lead to misleading results in a numerical stability analysis. In this section, we discuss the possibility of finding spurious instabilities, which are artifacts of the discretization [47]. These instabilities disappear as the radial grid-point spacing goes to zero. We also demonstrate that the numerical eigenmode expansion accurately captures the $m = 1$ algebraic instability, and that this instability is associated with a "singu-

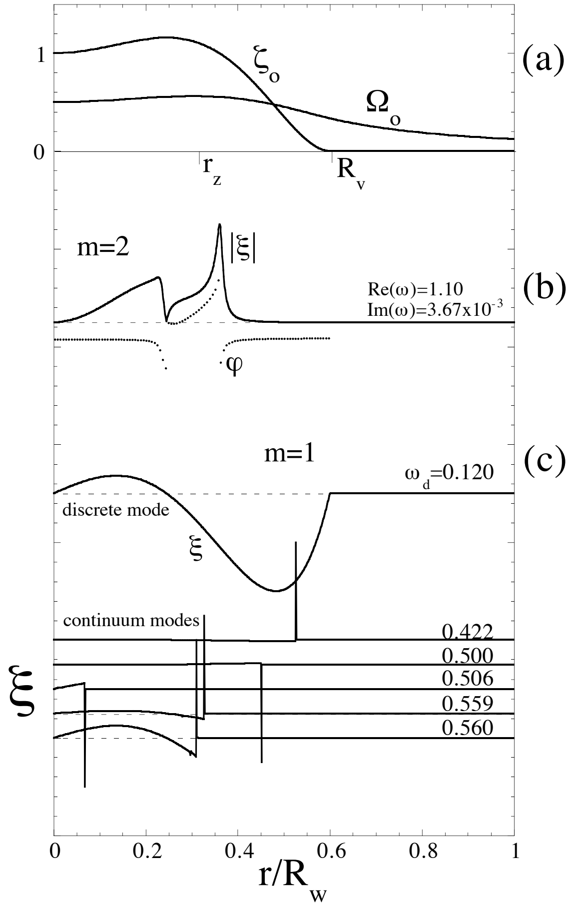

Figure 3.16: Hollow vortex. **(a)** Equilibrium Profile. **(b)** Unstable $m = 2$ eigenmode ($\xi = |\xi|e^{i\varphi}$). **(c)** $m = 1$ eigenfunctions.

larity" in the expansion coefficient A_k.

3.9.1 The Eigenmodes

Figure 3.17.b shows the numerical eigenspectrum for $m = 2$ perturbations on the hollow vortex. There exists one complex conjugate pair of eigenfrequencies that stand far away from the real axis, $Im[\omega_k] = \pm 3.67 \times 10^{-3}$. These eigenfrequencies stay fixed as the grid-point spacing Δr goes to zero. They are genuine exponentially damped and growing eigenmodes of the vortex. The imaginary parts of the additional complex eigenfrequencies disappear as Δr goes to zero. Therefore, these eigenmodes are spurious: their imaginary parts exist only in the discretized problem. The genuine unstable eigenmode is shown in Fig. 3.16.b.

Figure 3.17.a shows the numerical eigenspectrum for $m = 1$ perturbations on the hollow vortex. A selection of the (right-handed) radial eigenfunctions is shown in Fig. 3.16.c. The eigenmodes consist of a genuine discrete mode, continuum modes and a complex conjugate pair of spurious modes. The eigenfunction of the discrete mode (top) is proportional to ζ_o' and its eigenfrequency is equal to $\Omega_o(R_w)$. The growth/decay rates ($Im[\omega_k]$) of the spurious modes go to zero as the grid-point spacing Δr goes to zero (see Fig. 3.17.c). For $\Delta r = .001$, the e-folding time is 8.7×10^3 central rotation periods. This e-folding time far exceeds any time-scale that we will consider. So, the spurious eigenmodes are effectively neutral.

3.9.2 The Algebraic Growth of an m=1 Perturbation

Although the eigenmodes are neutrally stable, Smith and Rosenbluth [95] showed that a generic m=1 perturbation on a hollow vortex will grow asymptoti-

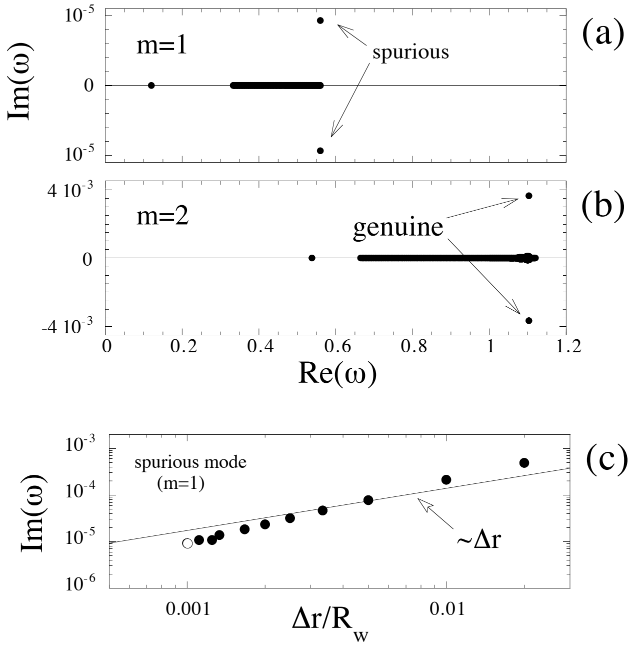

Figure 3.17: Eigenspectra of a hollow vortex. **(a)** $m = 1$. **(b)** $m = 2$. **(c)** Growth rate ($Im[\omega]$) of the spurious $m = 1$ eigenmode vs. the grid-point spacing (Δr).

cally with time like $t^{1/2}$. Specifically, the late-time growth is given by

$$\delta\zeta^{(1)}_{SR}(r,t) \sim -e^{-i\left(\Omega_o(r_z)t-\frac{3\pi}{4}\right)}\left|\frac{2\pi t}{\Omega''_o(r_z)}\right|^{1/2} h(r_z)H(r-r_z)\zeta'_o(r). \tag{3.65}$$

Here, r_z is the radius at which the shear is zero,

$$\Omega'_o(r_z) \equiv 0, \tag{3.66}$$

H is the heaviside step function,

$$H(r-r_z) = \begin{cases} 1 & r < r_z \\ 0 & r > r_z, \end{cases} \tag{3.67}$$

and h is the following integral over the initial vorticity perturbation,

$$h(r) = \frac{1}{r^3}\int_o^r dr' r'^2 \delta\zeta^{(1)}(r',0). \tag{3.68}$$

Note that the asymptotic perturbation is proportional to to $\zeta_o'(r)$ for $r < r_z$. In addition, the asymptotic perturbation [Eq. (3.65)] can grow to infinity for $r < r_z$ without affecting the vorticity distribution for $r > r_z$. This is because the stream function of the asymptotic perturbation vanishes for $r > r_z$.

We have tested the accuracy of the numerical eigenmode expansion by comparing it to the algebraic growth that is predicted by Smith and Rosenbluth. At $t = 0$, the hollow vortex was given a sinusoidal $m = 1$ perturbation:

$$\delta\zeta^{(1)}(r, 0) = \sin\left(\frac{\pi r}{R_v}\right). \tag{3.69}$$

The perturbation was decomposed into eigenmodes with expansion coefficients determined by Eq. (3.62). At later times, the perturbation is obtained from a

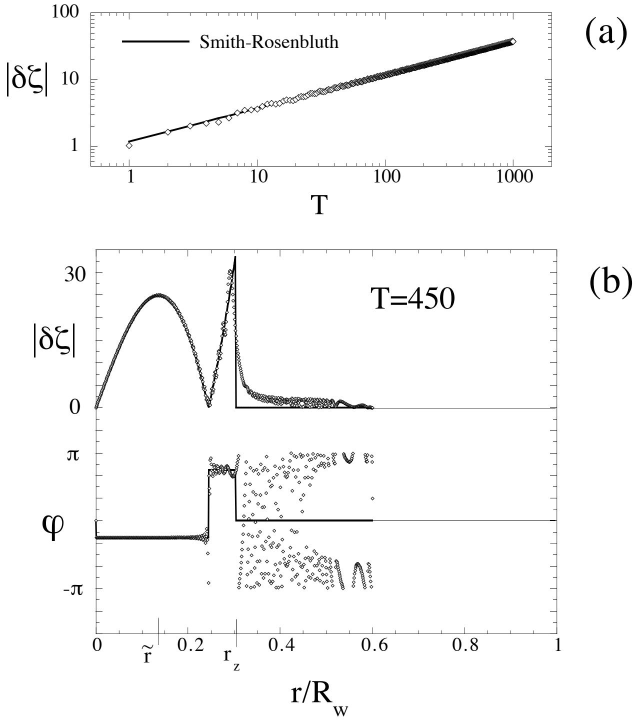

Figure 3.18: Evolution of an $m = 1$ perturbation on a hollow vortex. **(a)** $t^{1/2}$ growth of $|\delta\zeta|$ at $\tilde{r}$. **(b)** Vorticity perturbation at 450 rotation periods. Diamonds: numerical eigenmode expansion. Solid line: Smith-Rosenbluth theory.

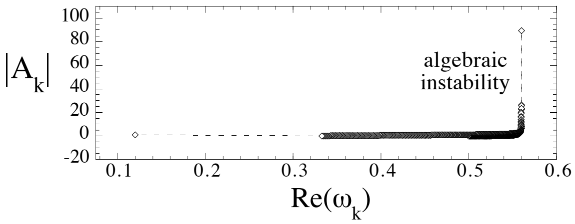

Figure 3.19: Expansion coefficients A_k for a sinusoidal $m = 1$ perturbation on a hollow vortex. The divergence at the largest eigenfrequency accounts for the algebraic instability.

sum over these eigenmodes, with their appropriate time-dependent phase-shifts (Eq. 61). Figure 3.18.a shows the amplitude of the perturbation as a function of time on a log-log plot. The amplitude is measured at the arbitrary radius $\tilde{r}$. As expected, the perturbation grows like $t^{1/2}$. Figure 3.18.b shows the amplitude and phase of the computed perturbation compared to $\delta\zeta_{SR}^{(1)}$ after 450 rotation periods: the two are in excellent agreement.

The algebraic growth of an $m = 1$ perturbation presents a paradox. For the case of a monotonic vortex, a perturbation consisting of neutral eigenmodes eventually decays as the eigenmodes disperse and "phase-mix". Here, we are faced with the unsettling result that an $m = 1$ perturbation on a hollow vortex will grow infinitely large due to a similar dispersion of neutral continuum modes.

Figure 3.19 provides the answer to this paradox. Figure 3.19 shows that the expansion coefficients A_k of our initial perturbation [Eq. (3.69)] diverge near the largest eigenfrequency. At $t = 0$, the eigenmodes with "infinite" amplitude are hidden through destructive interference. Dispersion *unmixes* these eigenmodes and causes the perturbation to grow like $t^{1/2}$, in accord with the theory of Smith and Rosenbluth.

3.10 Conservation of Energy, Angular Momentum and the Moments of Vorticity

The 2D Euler equations conserve the bulk kinetic energy E, the total circulation Γ and all higher moments of the vorticity Z_n, $n = 2, 3, \ldots, \infty$. With cylindrically symmetric boundary conditions, the 2D Euler equations also conserve the canonical angular momentum P_θ. These invariants are defined below:

$$\begin{aligned} &E \equiv -\tfrac{1}{2} \textstyle\int d^2r \ \psi\zeta, \\ &P_\theta \equiv \textstyle\int d^2r \ r^2\zeta, \\ &\Gamma \equiv \textstyle\int d^2r \ \zeta, \\ &Z_n \equiv \tfrac{1}{n} \textstyle\int d^2r \ \zeta^n \quad n \geq 2. \end{aligned} \tag{3.70}$$

Note that our definitions of energy and angular momentum are simplified for convenience. The actual bulk kinetic energy (per unit length in the z-direction) of the flow is ρE, where ρ is the uniform mass density of the fluid. The actual angular momentum (per unit length) is $\frac{1}{2}\rho\,(\Gamma R_w^2 - P_\theta)$.

So far, we have encountered perturbations that in linear theory can decay to zero or grow to infinity. It is of interest to understand how the invariants in Eq. (3.70) are conserved during this process.

We first consider the conservation of energy E. The energy decomposes into contributions from each azimuthal wave-number m. Specifically,

$$E \ = \ E_o \ - \ 2\pi \int_0^{R_v} drr \left[\psi_o \delta\zeta^{(0)} \ + \ \frac{1}{2}\delta\psi^{(0)}\delta\zeta^{(0)}\right] - 2\pi \sum_{m=1}^{\infty} \int_0^{R_v} drr\delta\zeta^{(m)}\delta\psi^{(m)*}. \tag{3.71}$$

Here E_o is the energy of the unperturbed circular flow. The term to the far right of Eq. (3.71) accounts for the energy of all components with $m \geq 1$. The middle term is the energy of the $m = 0$ component (ψ_o is the equilibrium stream function). It is second order in the perturbation amplitude since $\delta\zeta^{(0)}$ is a second order quantity,

$$\frac{\partial \delta\zeta^{(0)}}{\partial t} = -\frac{2}{r} Im\left[\sum_{m=1}^{\infty} m \frac{\partial}{\partial r}\left(\delta\psi^{(m)}\delta\zeta^{(m)*}\right)\right]. \tag{3.72}$$

Although it is possible to associate an energy with each azimuthal wavenumber m, it is not generally possible to assign an energy to an individual eigenmode. This is because the eigenmodes of an ideal 2D vortex do not "diagonalize E". This can be seen explicitly for the case of a monotonic vortex, where the energy of the m^{th} component of vorticity has the following expansion in the complex eigenmode amplitudes $\{a_k(t)\}$:

$$\begin{aligned} \delta E^{(m)} &\equiv -2\pi\int_0^{R_v} drr\delta\zeta^{(m)}\delta\psi^{(m)*} \\ &= 2\pi\sum_k |a_k|^2 \left\langle \xi_k, \left[\Omega_o - \frac{\omega_k}{m}\right]\xi_k \right\rangle + 2\pi\sum_{k\neq k'} a_k^* a_{k'} \left\langle \xi_k, \Omega_o \xi_{k'}\right\rangle. \end{aligned} \tag{3.73}$$

Equation (3.73) was derived using the relationship between ξ_k and Ψ_k that is given by Eq. (3.7). The inner product $<,>$ is that defined by Eq. (3.23). We have used a discrete notation for the eigenmode expansion since in practice it is numerical.

In the familiar case of a string or a drumhead, cross-terms do not appear in the eigenmode expansion of energy. Instead, the energy is a sum of terms that are proportional to $|a_k|^2$. In linear theory, these terms will stay constant, provided that the eigenfrequencies are real. On the other hand, the real eigenfrequencies of a monotonic vortex do not ensure conservation of energy for an individual m-number. The cross-terms in Eq. (3.73) permit interference that can lead to the growth or decay of $\delta E^{(m)}$. For example, when a quasi-mode with $m = 2$ decays, $\delta E^{(2)}$ goes to zero.

Of course, the energy of the quasi-mode does not vanish. A few steps of algebra show that the second order change in $\delta E^{(0)}$ exactly cancels the second order change in $\delta E^{(m)}$ that occurs through phase-mixing. In other words, the

$m = 0$ component of vorticity provides a source or sink of energy for linear flow with $m \geq 1$.

Unlike energy, the canonical angular momentum P_θ and the total circulation Γ have no direct contributions from wave-numbers with $m \geq 1$. Only the $m = 0$ component of vorticity contributes to these quantities,

$$\begin{aligned} P_\theta &= P_{\theta,o} + 2\pi \textstyle\int_0^{R_v} drr^3 \delta\zeta^{(0)}, \text{ and} \\ \Gamma &= \Gamma_o + 2\pi \textstyle\int_0^{R_v} drr \delta\zeta^{(0)}. \end{aligned} \tag{3.74}$$

In time, a perturbation with $m \geq 1$ will change $\delta\zeta^{(0)}$ according to Eq. (3.72). However, this change will conserve P_θ and Γ.

Conservation of Z_n occurs much like the conservation of E. For the case of small amplitude perturbations, it is possible to approximate Z_n as a second order integral,

$$Z_n \approx Z_n(\zeta_o) + 2\pi \int_0^{R_v} drr\,(\zeta_o)^{n-1}\,\delta\zeta^{(0)} + 2\pi(n-1)\int_0^{R_v} drr\zeta_o^{n-2} \sum_{m=1}^{\infty} \delta\zeta^{(m)}\delta\zeta^{(m)*} \tag{3.75}$$

In Eq. (3.75) it is evident that the $m = 0$ component of vorticity provides a source or sink of Z_n for the linear evolution of perturbations with $m \geq 1$.

3.11 Summary

In this chapter we examined the excitation and inviscid damping of small perturbations on a circular vortex. We showed that after an external impulse deforms the vortex, the multipole moment $Q^{(m)}$ of the perturbation oscillates at a constant frequency ω_q, and decays at an exponential rate γ. Furthermore, we found that both ω_q and γ are given by a Landau pole of the equilibrium profile. This result is significant, since perturbations that are not generated by an external impulse need not decay exponentially (see Section 3.6).

During exponential damping, the vorticity perturbation can be a quasi-mode, or undergo a complicated evolution that involves spiral wind-up. These different behaviors can be understood with an eigenmode analysis. When $\gamma/\omega_q << 1$, the excitation is dominated by a small group of exceptional continuum modes, which occupy a narrow frequency band of width γ, centered at ω_q. This wave-packet of exceptional continuum modes behaves like an exponentially damped discrete mode (for $r \lesssim r_c$). On the other hand, strong damping ($\gamma/\omega_q \sim 1$) corresponds to a more uniform excitation of the continuum modes. The critical radii (singular points) of these continuum modes span the entire vortex. Consequently, as the continuum modes disperse, their singular spikes "dephase" across the entire vortex. This accounts for the observed spiral wind-up.

For a top-hat vortex, we were able to explain why the Landau-pole dominates after an external impulse is applied to the vortex. Here, the Landau-pole was clearly associated with a quasi-mode (or a single discrete mode in the limit that $\gamma \to 0$). As mentioned in the previous paragraph, this quasi-mode is a small group of exceptional eigenmodes. We showed that, for $r \lesssim r_c$, the eigenfunctions of these modes are approximately equal to the radial perturbation that is generated by the impulse. By orthogonality, the other modes of the vortex have a much smaller overlap with the initial condition; therefore, the the other modes are not excited.

Physically, the excitation of a quasi-mode on a top-hat vortex is due to the exceptionally large multipole moments of the eigenmodes in the wave-packet. Because these eigenmodes have large multipole moments, they have the strongest influence on the external flow. By reciprocity, they are also the most easily excited by an external impulse (as discussed in Section 3.4).

We did not provide an explanation for why the Landau pole dominates the response of a Gaussian vortex. This result came as a surprise, since on the

Gaussian, there is no small group of eigenmodes (quasi-mode wave-packet) with exceptional large multipole moments. This is evident in the the strong damping ($\gamma/\omega_q \sim 1$) of the excitation, which implies a broad peak in the excitability spectrum.

In addition to our study of inviscid damping, we outlined the eigenmode method for solving the initial value problem. While this technique is not new [46, 47], we provided details which, to our knowledge, have not been discussed elsewhere [e.g. the orthogonality relations in Eq. (3.25)]. We have also verified explicitly that the numerical eigenmode expansion gives accurate results (e.g. Fig. 3.18). Of course, the expansion generally breaks down for lengths less than the radial grid-point spacing Δr, and times greater than the minimum value of $\sim 2\pi/m\Omega_o'(r)\Delta r$.

3.12 Appendix I: A Physical Explanation of Inviscid Damping.

In this appendix, we explain inviscid damping using conservation of canonical angular momentum, $P_\theta \equiv \int d^2r \;\; r^2\zeta$. Note that P_θ is a convenient simplification of the actual angular momentum $\mathcal{L}$, which is given by the equation $\mathcal{L} \equiv \hat{z} \cdot \int_0^{R_w} d^2r \;\; \vec{r} \times \rho\vec{v} = \frac{1}{2}\rho\,(\Gamma R_w^2 - P_\theta)$. Here, ρ is the uniform mass density of the fluid, and Γ is the total circulation of the flow [Eq. (3.70)].

3.12.1 The Angular Momentum of a Mode

For simplicity, we consider a uniform circular vortex patch of radius r_o and vorticity $\sigma > 0$. Suppose that a ripple of azimuthal wave-number m is created on the edge of the vortex patch, in such a way that the area of the (incompressible)

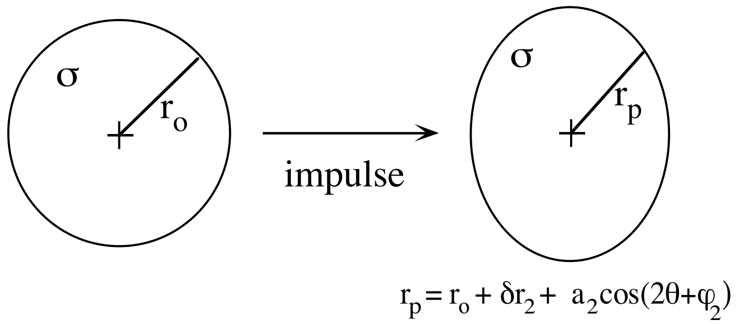

Figure 3.20: Elliptical deformation of a uniform circular vortex patch.

vortex patch is conserved. Figure 3.20 illustrates this perturbation for the case of $m = 2$. Here, the ripple corresponds to an elliptical deformation.

Let $r_p(\theta, t)$ describe the radius of the perturbed vortex patch. With the ripple,

$$r_p(\theta, t) = r_o + \delta r_m(t) + a_m(t) cos\left[m\theta + \varphi_m(t)\right]. \tag{3.A1}$$

Here $a_m(t)$ and $\varphi_m(t)$ are the amplitude and phase of the asymmetric part of the ripple. The symmetric part $\delta r_m(t)$ is required to conserve the area of the vortex patch. To lowest order, δr_m is related to a_m by the following equation:

$$\delta r_m = -\frac{a_m^2}{4r_o}. \tag{3.A2}$$

When the vortex patch is isolated, the ripple behaves like an undamped mode [92]. Specifically, $a_m(t)$ is constant and $\varphi_m(t) = -\omega t$. Here, ω is approximately (σ times) the Kelvin frequency ω_* that is defined in Eq. (3.32).

The angular momentum $P_\theta^{(m)}$ of the mode is defined as the difference in P_θ between the vortex patch with and without the mode. That is,

$$P_\theta^{(m)} \equiv \int_0^{2\pi} d\theta \int_0^{r_p} dr\ r^3\sigma - \int_0^{2\pi} d\theta \int_0^{r_o} dr\ r^3\sigma. \tag{3.A3}$$

Using Eq. (3.A1) for r_p, Eq. (3.A2) for δr_m, and carrying out the integrals in Eq. (3.A3), we obtain the following expression (to lowest order in a_m) for the

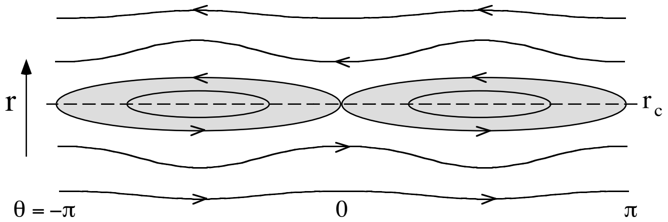

Figure 3.21: Kelvin's cat's eyes at the critical radius r_c.

angular momentum of the mode:

$$P_\theta^{(m)} = \pi\sigma r_o^2 a_m^2. \tag{3.A4}$$

3.12.2 Inviscid Damping

Now suppose that there is a low level ($<< \sigma$) of vorticity outside the vortex patch. If this low level of vorticity decreases monotonically with r, it will cause the mode to decay.

To see this, we examine the flow at the critical radius r_c ($> r_o$), where the fluid rotation is resonant with the mode ($m\Omega_o(r_c) = \omega$). In a frame that rotates with the mode, the streamlines near r_c form cat's eyes [96]. These cat's eyes (grey) are illustrated in Fig. 3.21, for the case of $m = 2$.

In time, the vorticity in the cat's eyes is mixed. Since $\zeta_o'(r_c) < 0$, this mixing increases the mean-square-radius of the flow (i.e. P_θ). The only way for the system to conserve total P_θ is for the mode amplitude a_m to decay. We refer to this process as "inviscid damping."

The rate of change of the mode angular momentum is equal and opposite to the rate of change of P_θ in the skirt of low-level vorticity that is outside the vortex patch. Let $P_\theta^{(s)}$ denote the angular momentum in the skirt. The time derivative of

$P_\theta^{(s)}$ can be expressed as the following integral:

$$\dot{P}_\theta^{(s)} = 2\pi \int_0^{R_w} dr\ r^3 \frac{\partial \delta\zeta_s^{(0)}}{\partial t}. \qquad (3.A5)$$

Here, $\delta\zeta_s^{(0)}(r,t)$ is the $m = 0$ vorticity perturbation in the skirt. Using Eq. (3.72) for the time derivative of $\delta\zeta_s^{(0)}$, and integrating by parts, we obtain

$$\dot{P}_\theta^{(s)} = 8\pi m \int_0^{R_w} dr\ r\ Im\left[\delta\psi^{(m)}\delta\zeta_s^{(m)*}\right]. \qquad (3.A6)$$

We will assume that the stream function $\delta\psi^{(m)}(r,t)$ is dominated by the mode. That is,

$$\delta\psi^{(m)}(r,t) \simeq \frac{a_m(t)}{2}\sigma r_o G_m(r|r_o)e^{-i\omega t}. \qquad (3.A7)$$

Here, G_m is the Green's function that is defined by Eq. (3.10). In Eq. (3.A7), the phase of the mode is simply $-\omega t$. This neglects any phase perturbation due to the low-vorticity skirt.

The evolution of $\delta\zeta_s^{(m)}$ is obtained from the linearized Euler equation,

$$\frac{\partial \delta\zeta_s^{(m)}}{\partial t} + im\Omega_o(r)\delta\zeta_s^{(m)} - i\frac{m}{r}\zeta_o'(r)\delta\psi^{(m)} = 0. \qquad (3.A8)$$

Here, $\delta\psi^{(m)}$ is given by Eq. (3.A7), and is proportional to the mode amplitude a_m. The solution to Eq. (3.A8) is given by

$$\delta\zeta_s^{(m)}(r,t) = a_m \frac{m\sigma r_o}{2r}\frac{\zeta_o'(r)G_m(r|r_o)}{m\Omega_o(r) - \omega}\left[e^{-i\omega t} - e^{-im\Omega_o(r)t}\right], \qquad (3.A9)$$

provided that $\delta\zeta_s^{(m)}$ is initially zero, and that a_m is approximately constant over the integration period t.

Substituting Eq. (3.A7) and Eq. (3.A9) into Eq. (3.A6) gives the following expression for the time derivative of the angular momentum in the skirt:

$$\dot{P}_\theta^{(s)} = -2\pi a_m^2 m^2 \sigma^2 r_o^2 \int_o^{R_w} dr G_m^2(r|r_o)\zeta_o'(r)\frac{sin\left[(m\Omega_o(r) - \omega)t\right]}{m\Omega_o(r) - \omega}. \qquad (3.A10)$$

After a few cycles (i.e. $m\Omega_o t \simeq \omega t >> 1$), the integrand in Eq. (3.A10) becomes sharply peaked at the critical radius r_c, and the integral asymptotes to a fixed value. This asymptotic value is given below:

$$\dot{P}_\theta^{(s)} = -2\pi^2\sigma^2 r_o^2 m G_m^2(r_c|r_o)\frac{\zeta_o'(r_c)}{|\Omega_o'(r_c)|}\; a_m^2 \qquad (3.A11)$$

By conservation of angular momentum, the time derivative of the mode angular momentum must balance the time derivative of the angular momentum in the skirt. That is,

$$\dot{P}_\theta^{(m)} = -\dot{P}_\theta^{(s)}. \qquad (3.A12)$$

We will use Eq. (3.A11) for the time derivative of $P_\theta^{(s)}$, with a_m now a function of time. This approximation is good, provided that the mode amplitude a_m varies slowly compared to the rate at which $\dot{P}_\theta^{(s)}$ equilibrates, under the condition of fixed a_m. That is, the decay rate γ of the mode must satisfy $\gamma/\omega << 1$.

Substituting Eq. (3.A4) and Eq. (3.A11) into Eq. (3.A12), we obtain

$$\frac{d}{dt}a_m^2 = \frac{\pi}{2m} r_o \zeta_o'(r_c)\left(\frac{r_o}{r_c}\right)^{2m-3}\left[1-\left(\frac{r_c}{R_w}\right)^{2m}\right]^2 \; a_m^2. \qquad (3.A13)$$

Here, we have used $\Omega_o' = -\sigma r_o^2/r^3$ $(r > r_o)$, and Eq. (3.10) for the Green's function G_m. The solution to Eq. (3.A13) is $a_m(t) = a_m(0)e^{-\gamma t}$, where the decay rate γ is given below:

$$\gamma = \frac{-\pi}{4m} r_o \zeta_o'(r_c)\left(\frac{r_o}{r_c}\right)^{2m-3}\left[1-\left(\frac{r_c}{R_w}\right)^{2m}\right]^2. \qquad (3.A14)$$

This decay rate is equal to the decay rate [Eq. (3.50), with $r_* \equiv r_c$] that was calculated by Briggs, Daugherty and Levy [48].

Note that when $\zeta_o'(r_c) > 0$, mixing at r_c decreases P_θ in the skirt. In this case, the amplitude (a_m) of the mode must increase to conserve angular momentum. In other words, positive vorticity gradient at r_c leads to an instability. This instability is evident in Eq. (3.A14), which gives a positive growth rate (negative

γ) when $\zeta_o'(r_c) > 0$.

3.13 Appendix II: Analogy to Plasma Kinetic Theory

In this appendix, we briefly mention some similarities between the eigenmodes of an inviscid 2D vortex and the eigenmodes of a neutral plasma that is governed by the 1D Vlasov-Poisson equations.

3.13.1 Linearized Vlasov-Poisson System

Consider a gas of electrons that is immersed in a neutralizing background of positively charged ions. Let $F(x, v, t)$ denote the electron distribution in x-v phase-space, where x is the position of an electron and v is its velocity. F can be written as a sum of two parts:

$$F(x, v, t) = f_o(v) + f(x, v, t). \tag{3.A15}$$

Here, f_o is the equilibrium distribution and f is a perturbation. We will assume that the evolution of f is given by the linearized Vlasov-Equation,

$$\frac{\partial f}{\partial t} + v\frac{\partial f}{\partial x} + \frac{e}{m_e}\frac{\partial \phi}{\partial x}\frac{\partial f_o}{\partial v} = 0. \tag{3.A16}$$

Here, $-e$ is the charge of an electron, m_e is the mass of an electron and $\phi(x, t)$ is the electrostatic potential. The electrostatic potential satisfies Poisson's equation,

$$\frac{\partial^2 \phi}{\partial x^2} = 4\pi e \int dv f. \tag{3.A17}$$

3.13.2 The Eigenmodes of the Distribution Function

The evolution of f will be constructed from eigenmodes of the form

$$f = g(v)e^{i(kx-\omega t)}. \tag{3.A18}$$

Substituting Eq. (3.A18) into Eq. (3.A16) and Eq. (3.A17), we find that the velocity eigenfunctions must satisfy the integral equation

$$(\omega - kv)\, g(v) + \frac{4\pi e^2}{m_e k} f_o'(v) \int dv' g(v') = 0. \tag{3.A19}$$

Equation (3.A19) has the same form as the eigenvalue equation for an ideal axisymmetric vortex [Eq. (3.11)]. The structure of the eigenmodes is completely determined by $f_o(v)$, just as the vortex eigenmodes are determined by $\zeta_o(r)$.

However, there are several differences worth mentioning. First, the "shear-factor" is always the linear function kv. In contrast, the shear-factor in the vortex eigenmode equation is $m\Omega_o(r)$, which is generally not linear with r. Second, the integral over the distribution function g has a weight factor of 1. In the vortex eigenmode problem, the weight factor is $r'G_m(r|r')$.

A complete solution to the eigenmode problem [Eq. (3.A19)] was derived by Van Kampen (1955) and Case (1959) [55, 56]. Their solution consists of continuum modes of the form

$$g(v) = -P\left(\frac{4\pi e^2}{m_e k^2}\frac{f_o'(v)}{(v-\omega/k)}\right) + \lambda(\omega/k)\delta\left(v - \omega/k\right). \tag{3.A20}$$

Here, P denotes the "principal part" and $\lambda(\omega/k)$ is a normalization factor. Note the singularity at the critical velocity $v_c = \omega/k$, which is analogous to the singularity at the critical radius of a vortex continuum mode.

In some cases, the equilibrium distribution f_o supports a discrete mode. For example, consider a monotonic distribution, where f_o decreases to zero in both directions from $v = 0$ to $v = \pm v_{max}$. The distribution f_o can have a discrete mode of the form

$$g_d(v) = \begin{cases} \dfrac{4\pi e^2}{m_e k^2}\dfrac{f_o'(v)}{v - \omega/k} & |v| < v_{max} \\ 0 & |v| \geq v_{max}, \end{cases} \tag{3.A21}$$

provided that $v_{max} < v_c \equiv \omega/k$. A cold plasma ($v_{max} \to 0$) is guaranteed to have a discrete mode with ω equal to the "plasma frequency", $\omega_p \equiv \sqrt{4\pi e^2 n_o/m_e}$. Here, n_o is the equilibrium electron density defined by the equation, $n_o = \int f_o dv$.

Now suppose that a tail is added to the "cold" distribution function. If this tail extends past the critical velocity v_c, the discrete mode will fracture into a wave-packet of continuum modes. According to Landau, this wave-packet should produce an electrostatic potential that damps exponentially with time [52]. This scenario is very similar to the transformation of a discrete mode into a quasi-mode by attaching a skirt to a vortex.

3.13.3 Numerical Solution

For a numerical solution, we can discretize the continuous velocity coordinate v. In particular, we will choose an evenly spaced grid,

$$v_i \in \{-N\Delta v, -(N-1)\Delta v, \ldots, (N-1)\Delta v, N\Delta v\}. \tag{3.A22}$$

The integral eigenvalue equation [Eq. (3.A19)] is now approximated by a system of $2N + 1$ linear equations:

$$\sum_{j=-N}^{N} M_{ij}^{(k)} g(v_j) = \omega g(v_i). \tag{3.A23}$$

Here, the index i runs from $-N$ to N. The matrix elements of $M^{(k)}$ are real and given below:

$$M_{ij}^{(k)} = k v_i \delta_{ij} - \frac{4\pi e^2}{m_e k} f_o'(v_i)\Delta v. \tag{3.A24}$$

In deriving this expression for $M_{ij}^{(k)}$, we have used trapezoidal integration to approximate the integral that appears in Eq. (3.A19).

The eigenvalues of $M^{(k)}$ will inform us of any exponential instabilities. Moreover, we can use the eigenmodes of $M^{(k)}$ to solve any initial value problem,

$$f\left(x, v_i, t\right) \approx \sum_k \sum_{l=-N}^{N} A_l^{(k)} g_l^{(k)}(v_i) e^{i\left(kx-\omega_l^{(k)}t\right)}. \tag{3.A25}$$

The expansion coefficients are obtained by projecting the initial perturbation onto the left handed eigenvectors of $M^{(k)}$.

The evolution of the electrostatic potential ϕ is of more practical value than the evolution of f. This potential can be written as a sum over contributions from each eigenmode

$$\phi(x,t) = \sum_k \sum_{l=-N}^{N} \Phi_l^{(k)} e^{i\left(kx-\omega_l^{(k)}t\right)}. \tag{3.A26}$$

The expansion coefficient $\Phi_l^{(k)}$ is an integral over the eigenmode $g_l^{(k)}(v)$:

$$\Phi_l^{(k)} = -\frac{4\pi e}{k^2} A_l^{(k)} \int dv g_l^{(k)}(v). \tag{3.A27}$$

3.14 Appendix III: Landau Poles

In this appendix, we review how to calculate numerically the Landau poles of a monotonic vortex. We present a brief summary (without derivations) of the main points in Refs. [48, 49, 50], and refer the reader to these articles for greater detail, and a more precise treatment.

Note that Refs. [48, 49, 50] concern themselves primarily with the evolution of $\frac{\partial \delta\psi}{\partial r}(R_w, t)$. In this thesis, we examine the evolution of the multipole moment $Q(t)$, which is defined in Eq. (3.49). These two quantities differ only by a constant of proportionality. Specifically, $Q(t) = (R_w)^{m+1} \frac{\partial \delta\psi}{\partial r}(R_w, t)$.

3.14.1 The Laplace Transform of the Multipole Moment

The multipole moment $Q(t)$, of a perturbation that varies like $e^{im\theta}$ can be written formally as a contour integral in the complex ω plane:

$$Q(t) = -\frac{1}{2\pi}\int_{+\infty+i\alpha}^{-\infty+i\alpha} d\omega\tilde{Q}(\omega)e^{-i\omega t}, \tag{3.A28}$$

where α is a positive real number. We will refer to the contour of integration in Eq. (3.A28) as the "inversion contour." The function $\tilde{Q}(\omega)$ is the usual Laplace transform, defined by $\tilde{Q}(\omega) = \int_0^\infty dtQ(t)e^{i\omega t}$.

A solution for $\tilde{Q}(\omega)$, in terms of the initial vorticity perturbation $\delta\zeta(r,0)$, can be extracted from the literature [48, 49]:

$$\begin{aligned}\tilde{Q}(\omega) = {} & \frac{i(R_w)^{m+1}}{\Psi_1(R_w,\omega)}\int_0^{R_w} dr\frac{r}{R_w}\frac{\Psi_1(r,\omega)\delta\zeta(r,0)}{\omega - m\Omega_o(r)} \\ & \equiv \frac{\mathcal{N}(\omega)}{\Psi_1(R_w,\omega)}.\end{aligned} \tag{3.A29}$$

Here, the function $\Psi_1(r,\omega)$ is a smooth solution to the equation

$$\left[\frac{1}{r}\frac{\partial}{\partial r}r\frac{\partial}{\partial r} - \frac{m^2}{r^2} + \frac{m}{r}\frac{\zeta_o'(r)}{\omega - m\Omega_o(r)}\right]\Psi_1(r,\omega) = 0, \tag{3.A30}$$

and is regular at the origin. By "regular at the origin", we mean specifically that $\Psi_1(0,\omega) = 0$.

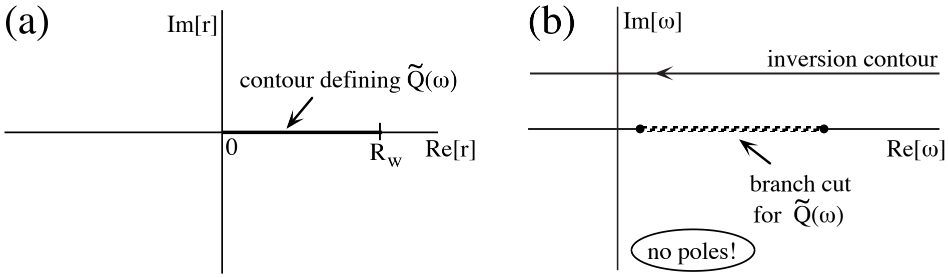

Figure 3.22: **(a)** When the radial integration contour is along the real r-axis, **(b)** there are no poles in $\tilde{Q}(\omega)$ that correspond to zeros of $\Psi_1(R_w,\omega)$.

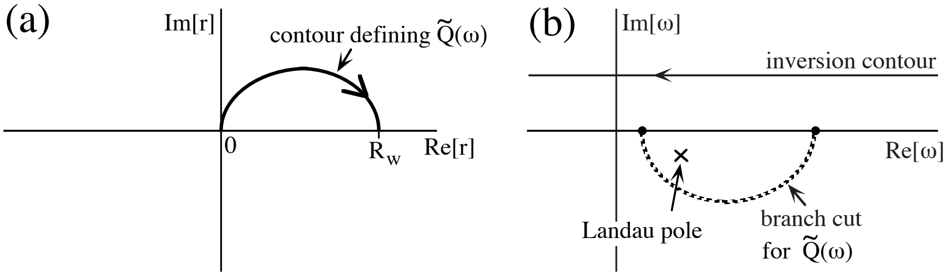

Figure 3.23: (a) When the radial integration contour is deformed into the upper half-plane, **(b)** a Landau pole appears in $\tilde{Q}(\omega)$.

Note that Eq. (3.A30) is nothing more than the eigenmode equation for stream function perturbations ($\Delta\psi$) that vary like $\Psi(r)e^{i(m\theta-\omega t)}$. The only difference is that Ψ_1 need not vanish at $r = R_w$, and therefore (nontrivial) solutions exist for arbitrary ω.

Suppose that the vortex extends to the wall (i.e. $R_v = R_w$), so that there are no discrete modes [48]. Then, there are no values of ω, for which $\Psi_1(R_w, \omega) = 0$. The analytic properties of $\tilde{Q}(\omega)$ for this case are shown schematically in Fig. 3.22. There are no poles in $\tilde{Q}(\omega)$, but there is a branch-cut along the real axis, in the interval $m\Omega_o(R_w) < \omega < m\Omega_o(0)$. This branch-cut arises from the singularity in the integrand that defines $\mathcal{N}(\omega)$.

It is possible to deform the branch-cut below the real-ω axis, by deforming the radial contour, in $\mathcal{N}(\omega)$, above the real-r axis. The new branch-cut, defined by $m\Omega_o\left(Re[r] + i\, Im[r]\right) = \omega$, is sketched in Fig. 3.23. If the branch-cut in the complex ω-plane bends sufficiently far below the real-axis, a Landau pole ($\omega = \omega_q - i\gamma$) will appear in the analytic continuation of $\tilde{Q}(\omega)$, between the branch-cut and the real ω-axis.

The Landau pole corresponds to a zero of $\Psi_1(R_w, \omega)$. This zero is now possible, since $\Psi_1(r, \omega)$ is defined along the deformed radial contour (Fig. 3.23.a),

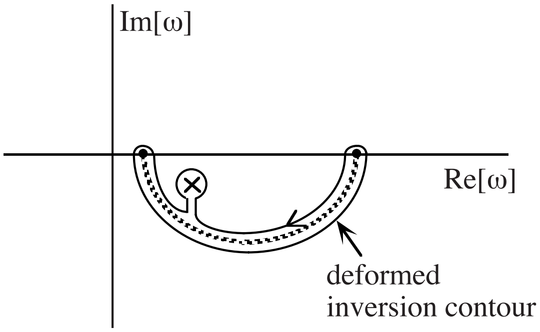

Figure 3.24: The inversion contour can be deformed to wrap around the branch-cut and the Landau pole. The contribution from the Landau pole gives a term in $Q(t)$ that decays exponentially.

and not the real r-axis. So, the Landau pole can be calculated by finding a discrete mode of Eq. (3.A30), along the deformed radial contour. The boundary conditions on this unphysical discrete mode are $\Psi_1(0,\omega) = \Psi_1(R_w,\omega) = 0$.

The inversion integral [Eq. (3.A28)] can be deformed around the Landau pole and the branch-cut, as illustrated in Fig. 3.2 The contribution from the Landau pole gives a term in $Q(t)$ that is proportional to $e^{-\gamma t}e^{-i\omega_q t}$. As we have seen, this term dominates the early evolution of $Q(t)$, when the initial perturbation is caused by an external impulse.

Note that the locations of Landau poles in the complex ω-plane are determined solely by the equilibrium profile $\zeta_o(r)$, and have no relation to the initial perturbation.

3.14.2 Numerical Computation of a Landau Pole

In Section 3.5, we examined the response of a Gaussian vortex to an external $m = 2$ impulse. We showed that the initial evolution of the quadrupole moment was dominated by the Landau pole. In this subsection, we discuss specifically how this pole was computed. A similar procedure was used to calculate the Landau poles of the experimental profiles.

As mentioned previously, a Landau pole is a solution to the mode equation [Eq. (3.A30)] along a deformed contour in the complex r-plane. The specific contour that we used to calculate the Landau pole of the Gaussian vortex [Eq. (3.53)] is the following parabola:

$$r(s) = R_w \left[s + i(s - s^2) \right], \tag{3.A31}$$

where s is a real parameter, which satisfies $0 \leq s \leq 1$.

The mode equation (3.A30) can be rewritten as a differential equation in s,

$$\left[\frac{\partial}{\partial s} \frac{r(s)}{r'(s)} \frac{\partial}{\partial s} - \frac{r'(s)\; m^2}{r(s)} + \frac{m\; r'(s)\; \zeta_o'[r(s)]}{\omega - m\Omega_o[r(s)]} \right] \hat{\Psi}_1(s,\omega) = 0, \tag{3.A32}$$

where $\hat{\Psi}_1(s,\omega) \equiv \Psi_1(r(s),\omega)$, and $r'(s) = R_w\left[1 + i(1-2s)\right]$. The asymptotic form of the $\Psi_1(r,\omega)$ is r^m, as $r \to 0$. This implies that $\hat{\Psi}_1(s,\omega)$ must satisfy the following boundary conditions at $s \equiv \varepsilon << 1$:

$$\begin{aligned} &(i) \quad \hat{\Psi}_1(\varepsilon,\omega) = r^m(\varepsilon), \quad \textit{and} \\ &(ii) \quad \frac{\partial \hat{\Psi}_1}{\partial s}(\varepsilon,\omega) = m\; r'(\varepsilon)\; r^{m-1}(\varepsilon). \end{aligned} \tag{3.A33}$$

The value of ε is typically $\sim 10^{-3}$, and the accuracy of the solution improves as $\varepsilon \to 0$.

The Landau pole is the complex value of ω that yields $\hat{\Psi}_1(1,\omega) = 0$. This value of ω is found using a standard shooting technique. For the Gaussian vortex in Eq. (3.53), we obtained the following value for the Landau pole: $\omega = 0.226 - 0.079\, i$.

Part of this chapter will appear in the AIP Proceedings of the 1999 Non-neutral Plasmas Workshop, D. A. Schecter, D. H. E. Dubin, A. C. Cass, C. F. Driscoll, I. M. Lansky and T. M. O'Neil, ed. J. J. Bollinger. D. A. Schecter was the primary investigator and author of this paper.

Chapter 4

Vortex Crystals from 2D Euler Flow: Experiment and Simulation

4.1 Introduction

Experiments and numerical simulations have shown that the free relaxation of 2D turbulence typically involves the chaotic advection and merger of intense vortices and the production of vorticity filaments that evolve to increasingly small length scales. In the past, variational principles have been used to predict the final state of the coarse-grained vorticity distribution. In some cases, the final states are seen to maximize entropy functionals [61-72], but different initial conditions can lead to states of minimum enstrophy [61, 73, 74, 75].

Strongly magnetized electron columns have recently been used to study the relaxation of 2D turbulence experimentally. One of the first of these experiments showed that certain hollow vortices relax to minimum enstrophy states after they experience a Kelvin-Helmholtz instability [75]. More recent experiments on electron columns [9] suggest that ideal 2D turbulence can self-organize into states where enstrophy is not globally minimized and entropy is not globally maximized. In these experiments, the chaotic advection of intense vortices “cools”, mergers cease and the vortices settle into a lattice that rotates rigidly in a lower vorticity

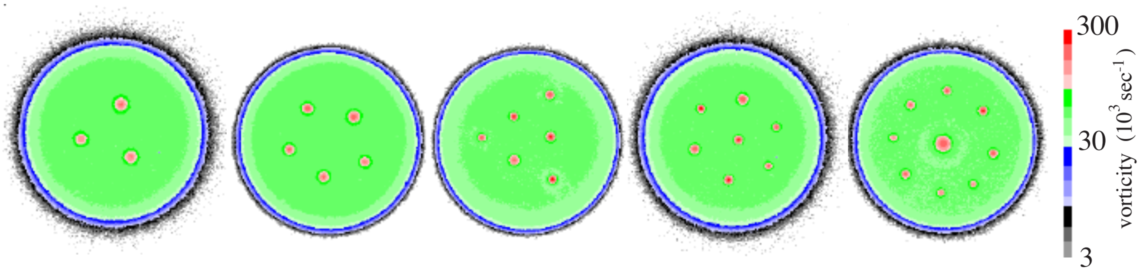

Figure 4.1: Vortex crystals observed in magnetized electron columns [9]. The color map is logarithmic. This figure shows vortex crystals with (from left to right) $M = 3$, 5, 6, 7, and 9 intense vortices immersed in lower vorticity backgrounds. In a vortex crystal equilibrium, the entire vorticity distribution $\zeta(r, \theta)$ is stationary in a rotating frame; i.e., ζ is a function of the variable $-\psi + \frac{1}{2}\Omega r^2$, where ψ is the stream function and Ω is the frequency of the rotating frame.

background. These rigid patterns persist for around 10^4 rotation periods before they are finally dissipated by nonideal effects. When the intense vortices have equal strength, the patterns are symmetric, and for this reason they have been called *vortex crystals*. A selection of vortex crystals is displayed in Fig. 4.1 (taken directly from Ref. [9]).

Although similar vortex crystals have been seen in dissipative systems such as two-fluid liquid helium [97], the rapid relaxation of a strongly magnetized electron column is believed to closely follow 2D Euler dynamics. It is surprising that inviscid fluid equations should provide a mechanism for cooling the chaotic advection of the intense vortices to a lattice in rigid rotation: to our knowledge, no previous experiment or simulation has demonstrated the spontaneous formation of vortex crystals from freely relaxing nondissipative turbulence. In order to show that the observed relaxation of turbulent flow to vortex crystals can be explained without incorporating physics beyond the ideal 2D fluid model, we compare the experiments directly to vortex-in-cell (VIC) simulations that numerically integrate the 2D Euler equations [58, 59]. The experiments and simulations are shown to relax at the same rates to vortex crystals with similar vorticity distributions. Close agreement between experiment and simulation provides strong evidence that 2D Euler theory alone can explain the formation of vortex crystals.

Of course, any numerical integration of the 2D Euler equations will differ from an exact solution. There is always concern that a new result is an artifact of the particular discretization scheme. However, we have confirmed that the VIC simulations conserve the robust integral invariants of 2D Euler flow. Moreover, the relaxation to a vortex crystal state occurs at the same rate whether the number of point-vortices in a simulation is 8×10^5, 4×10^5 or 1×10^5. In addition, the rate of relaxation does not change when the simulation's grid-point spacing (cell size) is increased by a factor of 2 or 4. Only subtle differences in the final vorticity distribution appear when the simulation parameters are changed. For example, an additional small vortex may appear in the final pattern.

By adding a slight random walk to each point-vortex in our simulation, we can observe the effect of a simple diffusive viscosity on the formation of vortex crystals [98]. Using this technique, we will show explicitly that viscosity in the Navier-Stokes equations acts to counter the formation of vortex crystals rather than enhance the rate at which the system of intense vortices relaxes to a pattern in rigid rotation. The reason is simple: viscosity acts to diffuse the intense vortices and level the vorticity distribution. The very high Reynolds number that is required to see vortex crystals may help explain why the formation of vortex crystals has not been observed in previous experiments or simulations of the Navier-Stokes equations.

As mentioned previously, vortex crystals cannot be explained either by considering global maximum entropy states[61-72] or minimum enstrophy states [61, 73, 74, 75]. Although complex vorticity patterns consisting of several asymmetric vortices can be predicted on the basis of maximum global entropy theory for certain special initial conditions, these patterns (corresponding to negative temperature states) typically consist of rather large slowly varying vortices that fill the confinement region, not the intense small vortices observed here. Furthermore, it is clear from observations of the evolution that the central regions of intense vorticity in the strong vortices arise from the initial flow, which consists of an intense striated vorticity pattern, and that these central regions *remain unmixed* with the larger low vorticity background. Global maximum entropy theory, which presumes ergodic mixing of all vorticity elements, clearly does not apply to this flow.

However, maximum entropy theory may apply to part of the flow- the low vorticity background. In a recent Letter [60], Jin and Dubin hypothesized that the turbulent flow is brought to a vortex crystal equilibrium due to the violent mixing of the diffuse background by the intense vortices. Assuming that the mixing of the background is ergodic, they argued that a vortex crystal is a state that maximizes disorder (entropy) in the background, subject to the constraints of 2D Euler flow. This *regional* maximum fluid entropy theory (so called because only the background vorticity is mixed, and the strong vortices are taken to be point-like without internal degrees of freedom) was shown to accurately predict the final positions of the intense vortices and the final background vorticity distributions of the experiments in Fig. 4.1, given the number of vortices and the energy, angular momentum and circulation.

Here, we present further evidence that the system is driven to a vortex crystal equilibrium through the turbulent mixing of the background by the intense vortices. First, we observe that the intense vortices do not cool to a vortex crystal when the background is removed from the simulation. We also find that the intense vortices do not cool in the opposite limit, when the background circulation dominates the circulation of the intense vortices. Presumably, the relaxation rate goes to zero in this limit because the vortices become ineffective mixers. As expected, the relaxation rate peaks at some intermediate level of the background, which is strong enough to influence the intense vortices but weak enough to be mixed.

4.2 Concerns with 2D Euler Theory and the Need to Compare Experiment to Simulation

4.2.1 Experiment

Figure 4.2 shows the experimental apparatus (Penning-Malmberg trap) with CCD imaging diagnostic. The electrons are confined radially by the force of a uniform magnetic field that is applied along the z-axis. They are trapped axially by negative voltages at opposite ends of the confinement cylinder.

The imaging diagnostic destructively measures the z-integrated electron density. By raising one end-potential rapidly to ground, the electrons are dumped onto a phosphor screen that radiates photons in proportion to the number of incident electrons, and the image is recorded with a 512 × 512 pixel CCD camera. Although the imaging is destructive, variations in the initial conditions are small ($\delta n/n \leq 10^{-2}$), so by dumping the electrons at a sequence of times we are able to study flows with this technique.

4.2.2 Ideal 2D Fluid Approximation

We can approximate the r-θ flow of electron density in our magnetized electron columns with the 2D drift-Poisson equations [6, 8, 48],

$$\partial n/\partial t + \vec{v} \cdot \nabla n = 0 \ , \tag{1a}$$

$$\vec{v} = \hat{z} \times c\nabla\phi/B \ , \tag{1b}$$

$$\nabla^2\phi = 4\pi en \ . \tag{1c}$$

Here, $n(r,\theta,t)$ is the z-averaged electron density, $\vec{v}(r,\theta,t)$ is the $\vec{E} \times \vec{B}$ drift in the r-θ plane, and $\phi(r,\theta,t)$ is the electrostatic potential. The equations are 2D because the electron motion has been averaged over a bounce period in the z-direction. The boundary condition at the wall of the confinement cylinder is $\phi(R_w,\theta,t) = 0$.

The equations that evolve vorticity, $\zeta \equiv \hat{z} \cdot \nabla \times \vec{v}$, can be obtained directly from the drift-Poisson equations. They are the Euler equations,

$$\partial\zeta/\partial t + \vec{v} \cdot \nabla\zeta = 0 \ , \tag{2a}$$

$$\vec{v} = \hat{z} \times \nabla\psi \ , \tag{2b}$$

$$\nabla^2\psi = \zeta \ , \tag{2c}$$

which also govern the flow of 2D inviscid incompressible fluids. The new field ψ is a rescaled electrostatic potential, $\psi \equiv c\phi/B$, and serves as a stream-function for the flow. Comparing Eqs. (4.1) and (4.2), we see that the vorticity is proportional to the electron density by the relation $\zeta = 4\pi ecn/B$. So, by measuring the electron density we are also taking a direct measurement of vorticity, insofar as 2D drift-Poisson theory is a good model for the experiment. The condition that ψ equals zero at R_w corresponds to a free-slip boundary condition at the wall of a circular container.

However, there is concern that the approximations used to derive Eqs. (4.1) and (4.2) neglect terms that are essential to the formation of vortex crystals. To begin with, Eqs. (4.1) and (4.2) describe the experiments only if the time scales associated with electron motion satisfy the inequalities $\tau_c \ll \tau_z \ll \tau_{\vec{E}\times\vec{B}}$. Here, τ_c denotes the period for an electron's small gyrations around a magnetic field line

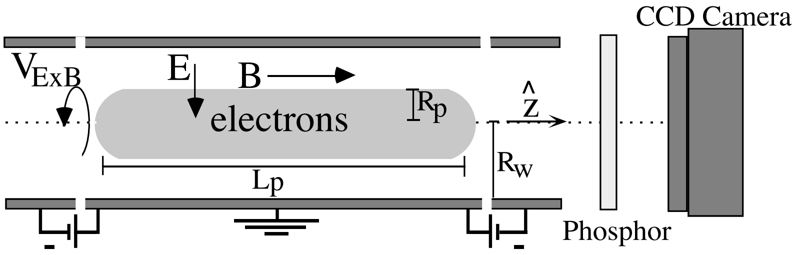

Figure 4.2: Cylindrical Penning-Malmberg trap and destructive imaging diagnostic. $\vec{E}$ is the electric field produced by the electrons and $\vec{B}$ is the uniform applied magnetic field. $V_{\vec{E}\times\vec{B}}$ denotes the counter-clockwise $\vec{E}\times\vec{B}$ drift of the electrons. $R_w = 3.5$ cm, $R_p \sim 1.5 - 2.5$ cm, and $L_p \sim 50$ cm.

(its cyclotron motion), τ_z is the time required for an electron to bounce between the ends of the plasma column in the z-direction, and $\tau_{\vec{E}\times\vec{B}}$ is the time scale for $\vec{E}\times\vec{B}$ drift. In our experiments, $\tau_c \sim 10^{-3}\mu$s, $\tau_z \sim 2\mu$s, and the internal turnover time for a typical vortex is $\tau_{\vec{E}\times\vec{B}} \sim 20\mu$s. Although τ_c is much less than τ_z and $\tau_{\vec{E}\times\vec{B}}$, the condition that $\tau_z \ll \tau_{\vec{E}\times\vec{B}}$ is only weakly satisfied. In addition to time scale constraints, there are length scale constraints. For example, the drift-Poisson approximation breaks down at length scales that are smaller than the cyclotron radius ($r_c \sim 10\mu$m). Furthermore, one assumes that the plasma is infinitely long in deriving Eqs. (4.1) and (4.2) since all variation in the z-direction is neglected. In reality, $L_p \sim 50$cm and $R_p/L_p \sim 0.05$.

A well-studied correction to the infinite-length approximation is that caused by the static electric fields that confine the plasma in the z-direction. These fields modify the bounce-averaged drift that is given by Eq. 4.1.b, and depending on circumstances this modification can enhance or suppress shear-flow instabilities [99, 100, 101]. In general, the modified drift increases with the kinetic energy of the electrons and a spread in electron energy will cause a vorticity profile to smear

[101].

Another correction to ideal fluid theory arises from the finite number N of "point-vortices" in the experiment. Each electron is like a 2D point-vortex after averaging over its z-motion. The Euler equations evolve the ensemble averaged density of a point-vortex gas only in the lowest order mean-field approximation, which neglects fluctuations due to finite N. These fluctuations can be treated with a collision term on the right hand side of the continuity Eq. 4.1.a or 4.2.a [102, 103]. This collision term is believed to be responsible for the eventual dissipation of vortex crystals that occurs in the experiments. The time scale for a vortex crystal to dissipate (10^3-10^4 rotations) far exceeds the time required for a vortex crystal to form (10-100 rotations). However, the collision term (due to finite N) may be enhanced at small length scales, and it was previously feared responsible for driving the turbulent flow to the metastable vortex crystal equilibrium.

4.2.3 Vortex-In-Cell Simulation

In this chapter, we address concerns over the ideal 2D fluid model by comparing the experiment directly to a VIC simulation that numerically integrates the 2D Euler equations [58, 59]. In the simulation, $N \leq 8 \times 10^5$ point-vortices are distributed to match the initial vorticity profile of the experiment. The vorticity is interpolated from the point-vortices to a square grid (usually 513×513) on which Poisson's equation is solved with the boundary condition $\psi(R_w, \theta, t) = 0$. The interpolation transfers vorticity from each point-vortex to the four nearest grid-points with the method of area weighting [58, 59]. Poisson's equation is solved with a five-point finite difference scheme that employs multigrid relaxation. The velocity field is obtained on the grid by taking the gradient of ψ and is then interpolated back to the particle positions. The particles move forward in time with second-order Adams-Bashforth steps.

In what follows, we will show that the VIC simulations are in good quantitative agreement with the experiments and that the simulation results are not sensitive to large variations in N or in the grid-point spacing. In doing so, we will demonstrate that vortex crystals are not caused by finite length effects, finite cyclotron radius effects, finite N effects or by any dynamics on time scales rapid compared to $\vec{E}\times\vec{B}$ drift (such as cyclotron motion or axial motion). In other words, although there exist subtle differences between a magnetized electron column and an ideal fluid, the observed vortex crystals can be explained without incorporating physics beyond 2D Euler theory [Eq. (4.2)].

4.3 Comparison of Experiment to Simulation

4.3.1 Integral Invariants

Before making a detailed comparison of experiment to simulation, it is important to check that both conserve the robust integral invariants of 2D Euler flow. The 2D Euler equations with θ-symmetric boundary conditions conserve the energy $H \equiv -\frac{1}{2}\int d\vec{r}^2\zeta\psi$, the canonical angular momentum $P_\theta \equiv \int d\vec{r}^2 r^2\zeta$, the total circulation $\Gamma_{\text{tot}} \equiv \int d\vec{r}^2\zeta$ ($\sim$ number of electrons) and all higher moments of the vorticity distribution $Z_m \equiv \frac{1}{m}\int d\vec{r}^2\zeta^m$, where $m = 2, 3, ...\infty$. By construction, our simulations conserve Γ_{tot}. They also conserve energy and angular momentum by roughly one part in 10^3. The experiments show up to 10% declines in Γ_{tot} over the first 100ms (100-1000 rotations), whereas the normalized quantities H/Γ_{tot}^2 and $P_\theta/\Gamma_{\text{tot}}$ fluctuate by only a few percent. The experimental decay in Γ_{tot} over time is probably caused by the slow ionization of background gas, which results in a loss of electrons. Although a small decrease in Γ_{tot} is undesirable, it seems incidental to the formation of vortex crystals. As we will see, the simulations produce vortex crystals while conserving Γ_{tot}.

Although Z_2 and all higher moments of vorticity Z_m are conserved by the 2D Euler equations, their measured values are generally not conserved in freely relaxing 2D turbulence. This is because any physical measurement of vorticity at a given position is an average over a cell of small but finite area. As vorticity filaments stretch and narrow to microscopic length scales, the measured vorticity along the filaments will decrease. An example of this decrease can be observed in Fig. 4.3, where the low vorticity (blue) regions increase in area over time.

The integrals H, P_θ and Γ_{tot} are insensitive to measurement coarse-graining of the vorticity. On the other hand, enstrophy Z_2 and all higher moments Z_m are fragile invariants, and their measured values will change due to coarse-graining.[1] In the experiments, vorticity is coarse-grained on a 512×512 pixel CCD camera, and the measured enstrophy Z_2 typically decays by a factor of 2 during the formation of a vortex crystal. In the VIC simulations, vorticity is coarse-grained on a 513×513 square grid, and the enstrophy of the coarse-grained vorticity also decays by a factor of 2 during the formation of a vortex crystal. We emphasize that a decay in the enstrophy of a coarse-grained vorticity distribution is entirely consistent with the 2D Euler equations.

4.3.2 Vortex Crystal Formation

We now proceed with a detailed comparison of experiment to simulation. Figure 4.3.a shows an experiment where an annular vorticity distribution evolves into a vortex crystal. Figure 4.3.b shows the results of a VIC simulation that starts with the same annular initial condition. The simulation has $N = 8 \times 10^5$ point-vortices and a 513×513 square grid. We will refer to the flow in Fig. 4.3 as

---

[1] Many papers on the statistical mechanics of 2D turbulence discuss the effect of coarse-graining on the integral invariants of 2D Euler flow. See for example, Ref. [65]

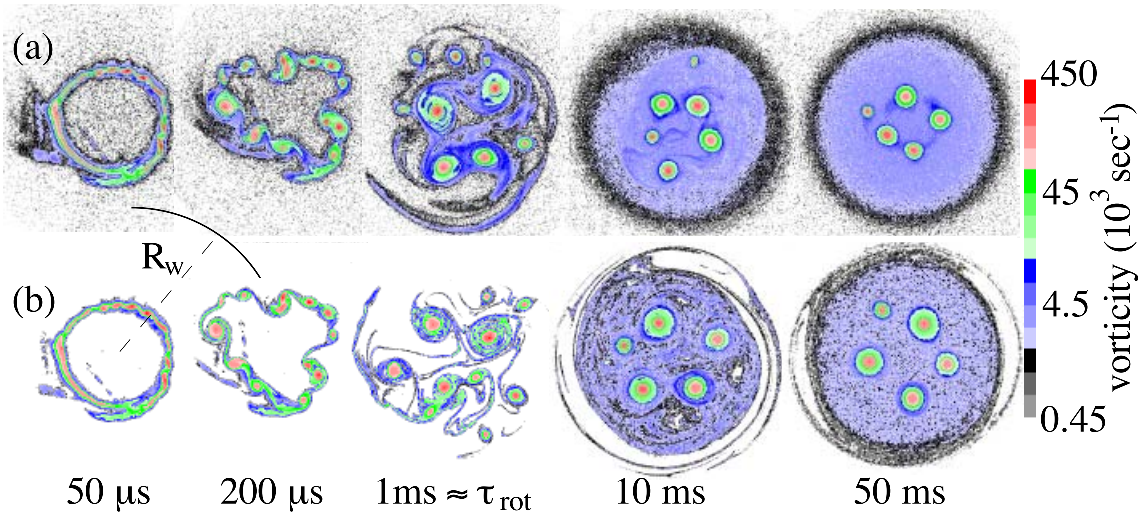

Figure 4.3: *Sequence I*, the formation of a vortex crystal from an annular vorticity distribution: (a) experiment, (b) simulation. The color map is logarithmic and the experimental vorticity is obtained from the relation $\zeta = 4\pi ecn/B$. All vorticity below the shot-noise threshold ($\zeta_{\text{thresh}} \sim 2.3 \times 10^3\text{sec}^{-1}$) was removed from the simulation's initial condition. The evolution is shown in a reference frame that rotates with frequency $5.872 \times 10^3 rad/sec$.

Sequence I.

In both the experiment and the simulation, a Kelvin-Helmholtz instability generates a "soup" of intense vortices. These vortices chaotically advect, merge and shed filaments that stretch and mix to form a diffuse background. Eventually the chaotic vortex motion cools, mergers stop and in both cases the intense vortices tend to a pattern in rigid rotation. Although our simulation does not reproduce the experiment exactly, both flows produce similar vortex crystals.

Most differences between the experiment and simulation emerge before one rotation period. These differences include the precise shapes and arrangement of intense vortices, and the filamentation which appears to be more "smeared" in the experiment than in the simulation. We speculate that these differences are primarily due to the additional drifts in the experiment that are caused by the electrostatic confinement fields and that vary with the axial kinetic energy of the electrons [99, 101].

Despite subtle differences, the experiment and simulation show good quantitative agreement in several key areas. First, they have similar evolutions in the number M of intense vortices. As in Ref. [9], the vortex census used here is essentially that of McWilliams [104] without the exclusion of elongated vortices; we define an intense vortex as a connected patch of vorticity for which $\zeta > \zeta_{\text{min}}$ and for which the mean diameter $d > d_{\text{min}}$. Here ζ_{min} and d_{min} are parameters of the counting algorithm. These parameters were changed slightly from those used in Ref. [9], so that vortices smaller than $d_{\text{min}} \equiv .05\text{cm}$ in diameter were not counted. A brief discussion of the uncertainties inherent in this census method can be found at the end of this section.

Figure 4.4.a shows that the evolution of the number M of intense vortices in the simulation (solid symbols) falls within the scatter of the experimental data (open symbols). The high degree of scatter at late times in the experiment is a consequence of slight differences in the initial conditions associated with each experimental "shot." Recall that each experimental datum is taken from a separate evolution due to the destructive imaging technique. After the Kelvin-Helmholtz instability and before M reaches its final value, the evolution in the number of intense vortices resembles a power-law decay, $M \sim t^{-\xi}$ for $0.3 < t/\tau_{\text{rot}} < 6$. Here $\tau_{\text{rot}} = 1.07$ ms is the time averaged rotation period of the vortex crystal in the simulation (Fig. 4.3.b). Linear least-squares fits to log-log plots of the data give $\xi_{\text{sim}} = 0.3 \pm 0.1$ and $\xi_{\text{exp}} = 0.2 \pm 0.1$. Power-law decays in M have been observed in previous simulations of ideal 2D fluid equations [104] and in simulations on discrete vortices that follow punctuated Hamiltonian dynamics [77]. Power law decays

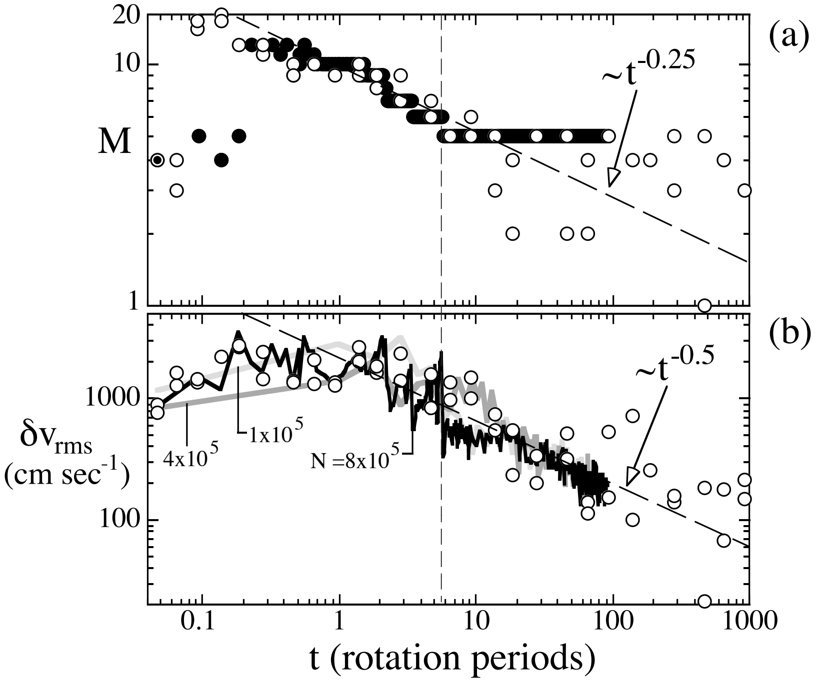

Figure 4.4: (a) Number of vortices M versus time for Sequence I. (b) Cooling curves $\delta v_{\mathrm{rms}}(t)$ for same flow. Black, dark grey and light grey correspond to simulations with $N = 8 \times 10^5$, 4×10^5 and 1×10^5 respectively. Open circles correspond to the experiment. The vertical dashed line indicates the time at which M reaches its terminal value. The slanted dashed lines suggest power-law decays. Time t is normalized to the rotation period of the vortex crystal in the simulation (Fig. 4.3.b), $\tau_{\mathrm{rot}} = 1.07$ ms.

occur in many processes where the decay rates $\dot{c}/c$ are proportional to powers of the concentration c, such as colloidal aggregation, certain chemical reactions and two or three body recombination [104, 105].

During the formation of vortex crystals, the chaotic advection of the intense vortices slowly relaxes, and as mergers stop the intense vortices tend to a pattern that rotates rigidly in a lower vorticity background. We refer to this process as *vortex cooling.* Vortex cooling is observed to occur at the same rate in the experiment and simulation. To show this requires a quantitative measure of vortex cooling.

First, the positions $\{\vec{r}_i\}$ $(i = 1, 2, \ldots, M)$ and the velocities $\{\vec{v}_i\}$ of the intense vortices are calculated relative to the flow's center of vorticity: $\vec{r}_i \equiv \int_{A_i} d\vec{r}^2 (\zeta - \zeta_{\text{min}})(\vec{r} - \vec{r}_{\text{cv}}) / \int_{A_i} d\vec{r}^2 (\zeta - \zeta_{\text{min}})$ and $\vec{v}_i \equiv \int_{A_i} d\vec{r}^2 (\zeta - \zeta_{\text{min}})(\vec{v} - \dot{\vec{r}}_{\text{cv}}) / \int_{A_i} d\vec{r}^2 (\zeta - \zeta_{\text{min}})$. Here, A_i denotes the region occupied by the i^{th} intense vortex and $\vec{r}_{\text{cv}}$ is the flow's center of vorticity defined by the equation $\vec{r}_{\text{cv}} \equiv \frac{1}{\Gamma_{\text{tot}}} \int d\vec{r}^2 \vec{r} \zeta$. The mean rotation of the intense vortices about $\vec{r}_{\text{cv}}$ is then subtracted from each $\vec{v}_i$, giving a set of velocity fluctuations $\{\delta\vec{v}_i\}$ about the mean rotation: $\delta\vec{v}_i \equiv \vec{v}_i - r_i \bar{\Omega}(t)\hat{\theta}$, where $\bar{\Omega}(t) \equiv \sum_{i=1}^{M} v_{i,\theta} / \sum_{i=1}^{M} r_i$ (radial-weighted averaging). A discussion of the error in the measurement of $\delta\vec{v}_i$ can be found at the end of this section.

As the pattern of intense vortices approaches uniform rotation, the root-mean-square value of the velocity fluctuations tends to zero; i.e., $\delta v_{\text{rms}} \equiv (\sum_{i=1}^{M} \delta\vec{v}_i^2 / M)^{1/2} \to 0$ as $t \to \infty$. We will refer to the graph of δv_{rms} versus time as the *cooling curve* of the flow.

Figure 4.4.b shows the cooling curves for the experiment and for the simulation of Sequence I. The cooling curves are approximately the same. Although one decade of vortex cooling does not suffice to accurately determine the functional form of $\delta v_{\text{rms}}(t)$, a power-law gives a good description at late times, $\delta v_{\text{rms}} \sim t^{-\alpha}$. Linear least-squares fits to log-log plots of the data give $\alpha_{\text{sim}} = \alpha_{\text{exp}} = 0.5 \pm 0.2$ for times greater than one rotation period.

A similar comparison to simulation has been made for an experiment that was taken directly from Ref. [9]. We will refer to this flow as Sequence II. Here, the vorticity in the experiment starts as a tightly wound filament, as seen in Fig. 4.5. Using $N = 8 \times 10^5$ point-vortices and a 513×513 square grid, our simulation failed to produce a vortex crystal from this initial condition. As reported in Ref. [9], small-scale details appear crucial in determining whether the spiral distribution will evolve into a vortex crystal or into an axisymmetric equilibrium. The essential

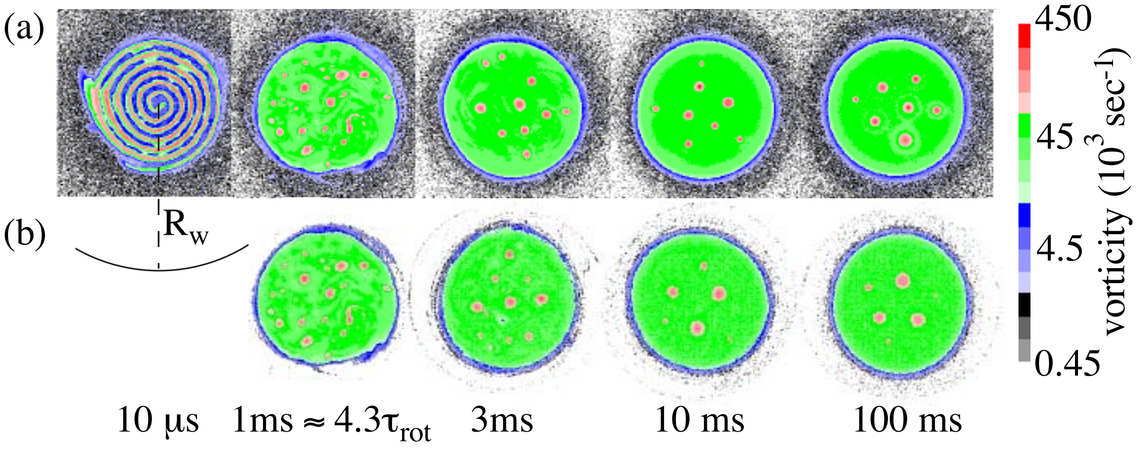

Figure 4.5: *Sequence II*, the formation of a vortex crystal from a spiral vorticity distribution: (a) experiment, (b) simulation. All vorticity below the shot-noise threshold ($\zeta_{\text{thresh}} \sim 2.3 \times 10^3 \text{sec}^{-1}$) was removed from the simulation's initial condition. The evolution is shown in the laboratory frame.

details may have been lost due to the finite resolution of the CCD imaging. Otherwise, the simulation's failure to produce a vortex crystal can only be blamed on slight dynamical differences with the experiment. To compensate, we began the simulation at a later stage of the flow (~ 4 rotations), at which time there were multiple intense vortices ($M = 15$).

Figure 4.6.a shows the evolution in the number of intense vortices over time for the simulation (solid black circles) and the experiment (open circles). The light grey data will be discussed shortly. The decay rates are similar, but the final number of intense vortices in the simulation ($M = 5$) falls below the experimental average ($M \approx 7$). Note that in the simulation the last merger event occurs at 25 rotation periods. The final drop in M from 6 to 5 (at $t/\tau_{\text{rot}} \approx 450$) corresponds to a small vortex being sheared apart as it periodically passes regions of intense shear-flow produced by neighboring strong vortices.

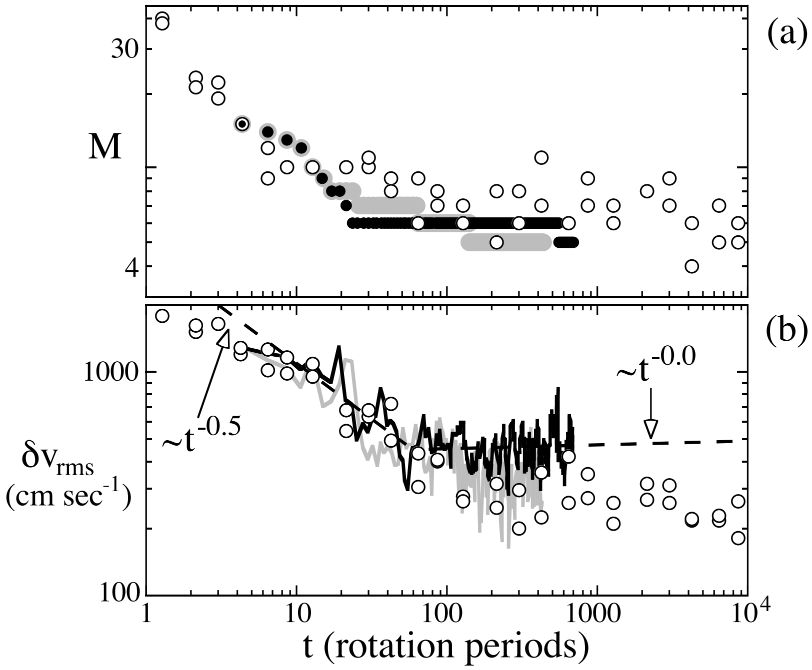

Figure 4.6: (a) Number of vortices M versus time for Sequence II. (b) Cooling curves $\delta v_{\mathrm{rms}}(t)$ for the same sequence. Black corresponds to the simulation in Fig. 4.5.b, open circles correspond to the experiment and light grey corresponds to a simulation that was initialized to include measured vorticity below the shot-noise threshold (grey fuzz in the experimental images). The dashed lines show that the cooling exponent α changes after mergers stop. Both lines correspond to power-law fits of the simulation data. Time t is normalized to the rotation period of the vortex crystal in the simulation where the shot-noise is removed, $\tau_{\mathrm{rot}} = 0.23$ ms.

The cooling curves for the simulation and the experiment are shown in Fig. 4.6.b. These cooling curves show close agreement during the initial turbulent phase of the flow, when mergers of intense vortices occur regularly. During this time period, least-squares fits to the data give cooling exponents $\alpha_{\mathrm{sim}} = 0.5 \pm 0.2$ and $\alpha_{\mathrm{exp}} = 0.4 \pm 0.1$. However, the cooling curve in the simulation levels off before cooling stops in the experiment. We can resolve this discrepancy in part by observing that in both cases cooling appears to stop shortly after the last merger event. Beyond the last merger, least squares fits to the data give cooling exponents $\alpha_{\mathrm{sim}} = 0.0 \pm 0.1$ and $\alpha_{\mathrm{exp}} = 0.1 \pm 0.1$.

An additional simulation was initialized to include the measured background vorticity below the shot-noise threshold (the grey fuzz in the experimental images). The data for this simulation is shown in grey in Figs. 4.6.a and 4.6.b. This flow differs from the previous simulation (black) in that the final merger event occurs at a much later time, a time that appears to be more consistent with the experiment (open circles). In addition, the cooling curve levels off at a lower value of δv_{rms}. This enhanced cooling may result from the additional merger at $t/\tau_{\mathrm{rot}} \approx 100$ or from an interaction with the low-vorticity (below the shot-noise threshold) background that was added to the exterior flow.

We end this section with a brief word on the uncertainty in the number of intense vortices M and in the measure of chaotic vortex motion δv_{rms}. To calculate M and δv_{rms} we use an automated vortex survey [104]. This survey has adjustable parameters ζ_{min} and d_{min} that are used to identify intense vortices in a turbulent flow. Recall that a vortex is defined to be a connected patch of vorticity for which $\zeta > \zeta_{\mathrm{min}}$ and for which the mean diameter $d > d_{\mathrm{min}}$. There is good agreement between the experiment and simulation regardless of the common parameters that we choose to analyze them both. However, the exact values of M and δv_{rms} will change with the specific parameter choice. For example, we have calculated $M(t)$ and $\delta v_{\mathrm{rms}}(t)$ for Sequence I (Fig. 4.3) with values of ζ_{min} between 4.5×10^4 and $4.5 \times 10^5 \mathrm{sec}^{-1}$ and with values of d_{min} between 2.5×10^{-2} and 7.5×10^{-2}cm. During the initial break-up of the annulus, there were large variations in the number of vortices M due to changes in ζ_{min} and d_{min} ($\delta M/M \sim 1$). However, the uncertainty in M dropped to $\sim 10\%$ after 1 rotation period and to 0% after the last merger. Before the last merger, the uncertainty in δv_{rms} was $\sim 20\%$ on average. After the last merger, the uncertainty in δv_{rms} dropped to less than 5%.

4.4 Discretization Effects and Viscosity

A magnetized electron column and a VIC simulation each consist of a finite number of point-vortices N. (The electron column consists of N lines of charge, each line charge corresponds to an electron trajectory averaged over the fast axial motion.) The 2D Euler equations govern the ensemble averaged vorticity distribution of a point-vortex gas only in the lowest order mean-field approximation, which neglects fluctuations due to finite N. These fluctuations are thought to cause the slow dissipation of vortex crystals that is observed in experiments with magnetized electron columns. An example of this dissipation process is shown in Fig. 4.7. Here, the decay occurs between 500 and 1000 rotation periods. The dissipation time scale is much greater than the time required for the system to reach a metastable vortex crystal equilibrium (∼10-100 rotations), but this fact alone does not eliminate the possibility that fluctuations due to finite N drive vortex cooling.

A statistical treatment of finite N effects leads to a collision term on the right hand side of the continuity Eqs. 4.1.a or 4.2.a. Unlike the constant viscosity ν of Navier-Stokes flow that leads to a simple diffusion of vorticity along streamlines, $\partial\zeta/\partial t + \vec{v}\cdot\nabla\zeta = \nu\nabla^2\zeta$, the collision term of a point-vortex gas must conserve H and P_θ. The correct form for the collision term of a point-vortex gas is still unresolved and is a topic of current research. For the case of axisymmetric ζ, a Klimontovich approach has been used to derive an explicit result [102, 103]. A more general equation for the collision term has yet to be written down. However, as N decreases the collision term should have an increasing effect on the evolution of ζ.

We examined the importance of finite N effects on the formation of vortex

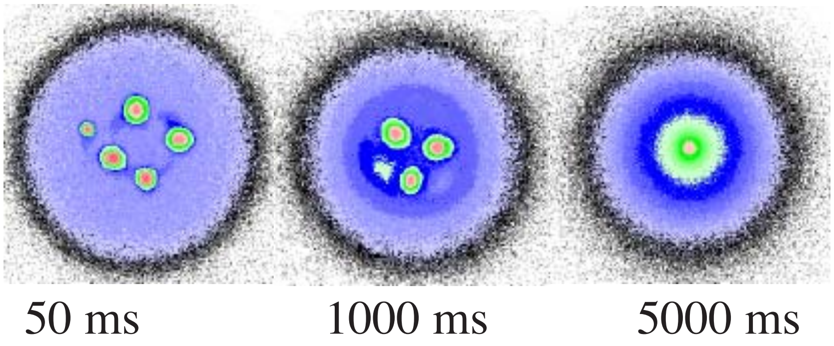

Figure 4.7: Finite N effects. (a) Dissipation of a metastable vortex crystal in an experiment. This dissipation is believed to be a finite N effect and conserves H/Γ_{tot}^2 and $P_\theta/\Gamma_{\text{tot}}$. The color map is the same as in Fig. 4.3.

crystals by changing the number of point-vortices in a simulation (Fig. 4.3.b) from 8×10^5 to 4×10^5 to 1×10^5. For $N = 4\times10^5$ and 1×10^5 an additional small vortex appeared in the final crystal, but the total circulation of the intense macroscopic vortices, $\sum_{i=1}^{M}\Gamma_i$, remained the same within 5%. Furthermore, the cooling curves for $N = 4\times10^5$ and 1×10^5 fall within the scatter of the cooling curve for $N = 8\times10^5$ (Fig. 4.4.b). This result suggests that the finite number of point-vortices is not important to the observed vortex cooling. This argument is strengthened by the fact that the experiment (Sequence I) has $\sim 10^8$ particles and cools at the same rate as the simulations.

We have also increased the grid-point spacing in the simulation by factors of 2 and 4, keeping N fixed at 8×10^5 particles. Once again, only subtle changes were observed. When the grid-point spacing was doubled, 2 additional vortices appeared in the vortex crystal. When the grid-point spacing was increased by a factor of 4, the two small vortices disappeared. In both cases, the cooling curves overlapped the original, within the scatter of the data.

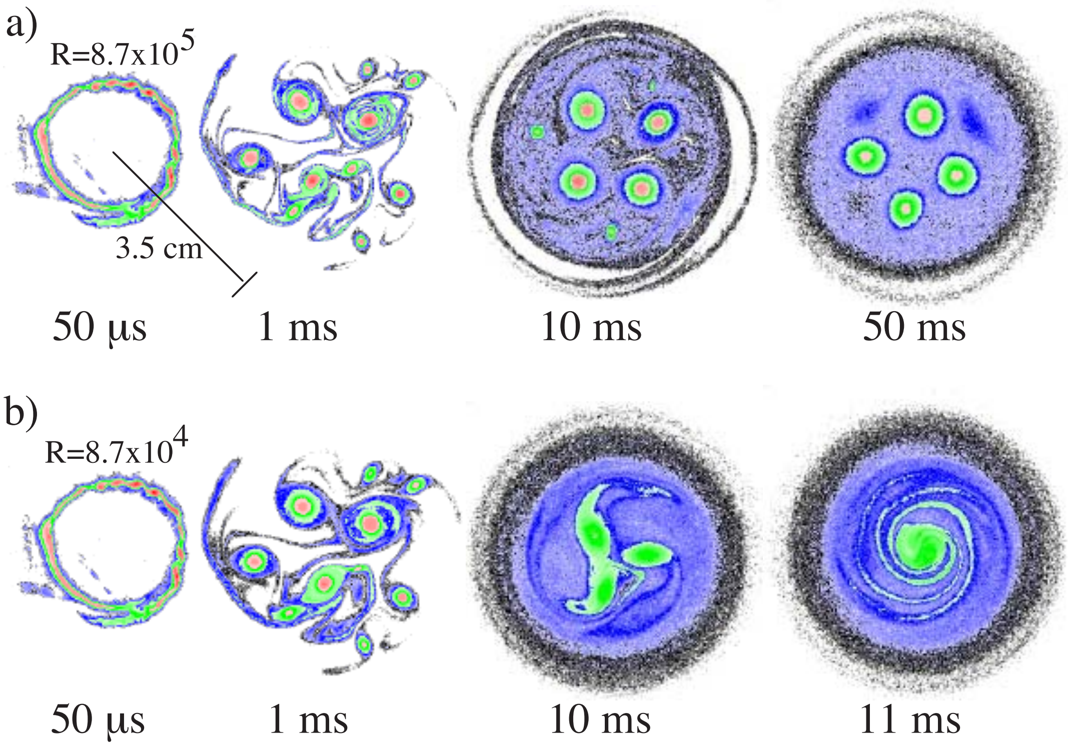

Figure 4.8: The effect of viscosity in the Navier-Stokes equations. (a) The evolution of an unstable annulus to a vortex crystal with viscosity $\nu = 0.127 cm^2/sec$ added to the simulation. (b) When $\nu = 1.27 cm^2/sec$, the viscosity is sufficiently high to prevent formation of a vortex crystal. The color map is the same as in Fig. (4.3), and the evolution is shown in a reference frame that rotates with frequency $5.872 \times 10^3 rad/sec$. The Reynolds number R is defined in the text.

While on the topic of nonideal effects, it is also of interest to estimate the minimum level of viscosity in the Navier-Stokes equations that is required to prevent the formation of a vortex crystal. Specifically consider Sequence I, where a vortex crystal forms from an unstable annulus (Fig. 4.3). In Sequence I, the final merger occurs at $T \approx 6ms$ (5.6 rotations). After mergers stop, the spacing L between vortex centers is $\sim$ 1cm and the average vortex radius ρ satisfies the condition $\rho < L/3.2$, which is required to prevent pair-wise mergers [78].

Now consider a flow with the same annular initial condition but with kinematic viscosity ν. Over time, viscosity will expand each vortex such that $\rho \sim \sqrt{4\nu t}$. Define the critical viscosity ν_c by the equation $\nu_c \equiv (L/3.2)^2\,(1/4T)$. If $\nu \gtrsim \nu_c$, the expanded vortices at time T are no longer stable against mergers in the vortex crystal configuration. In other words, if $\nu \gtrsim \nu_c$, viscosity should prevent the formation of a vortex crystal. For Sequence I, ν_c is approximately $4cm^2/sec$.

It is possible to model Navier-Stokes viscosity in a VIC simulation by adding a Gaussian random walk to the fluid drift of each point-vortex [98]. Figure 4.8.a and Fig. 4.8.b show the evolution of the annulus in Sequence I with $\nu = 0.127cm^2/sec$ and $\nu = 1.27cm^2/sec$ respectively. Once again, the simulations use 8×10^5 point-vortices and a 513×513 square grid. In Fig. 4.8.a, the vorticity distribution evolves into a pattern that resembles a vortex crystal. The estimated time for viscosity to generate a merger instability in this pattern is $\sim 190ms$, which is well beyond the simulation's run time. In Fig. 4.8.b, there appears to be no intermediate time scale during which the flow can be described as a vortex crystal. This result more or less agrees with our expectation that a vortex crystal should not form if $\nu \gtrsim \nu_c$.

To summarize our observation in dimensionless terms, we define a Reynolds number R by the equation $R \equiv \Gamma_{\text{tot}}/\nu$. In Fig. 4.8.a $R = 8.7 \times 10^5$, and in Fig. 4.8.b $R = 8.7 \times 10^4$. It is apparent from Fig. 4.8 that vortex crystals will form in Sequence I only if $R >> 10^5$.

4.5 Ideal Fluid Mechanism for Vortex Cooling

In this section, we address the question of how 2D Euler flow can bring a system that consists of intense self-trapped vortices and a diffuse background of small scale vorticity filaments to a vortex crystal equilibrium. This relaxation is described by the cooling curve $\delta v_{\text{rms}}(t)$, where δv_{rms} is the root-mean-square velocity fluctuation of the intense vortices. As the flow relaxes to a vortex crystal equilibrium, the chaotic advection of the intense vortices cools and δv_{rms} tends to zero. In Sequence I, vortex cooling continues indefinitely after mergers stop (Fig. 4.4), indicating that there exists a cooling mechanism independent of merger events. Such cooling would not occur if the intense vortices were simply advecting in their mutual fields like an isolated Hamiltonian system of point-vortices. However, the vortices are not isolated in that they can interact with the background.

Recall from the introduction that the observed vortex crystals are in excellent agreement with states that maximize disorder (fluid entropy) in the background [60]. According to regional maximum fluid entropy theory, vortex cooling is caused by the ergodic mixing of the diffuse background by the intense vortices. If the vortices are unable to mix the background, then no vortex cooling should occur, as verified by the following numerical results.

First consider Sequence I (Fig. 4.3.b) at 14 rotation periods, after which the number of intense vortices M and the total circulation of the intense vortices $\sum_{i=1}^{M}\Gamma_i$ remain fixed. Suppose that all vorticity below $\zeta \approx 10^4$ sec^{-1} is artificially removed from the simulation at this time, leaving only the intense vortices. Evolving this artificial system forward, we observe no cooling of the vortex motion. This result is shown in Fig. 4.9, and indicates that vortex cooling is not caused by internal motions within the vortices.

Figure 4.10 offers a more detailed description of how the cooling exponent α varies with the ratio of the background circulation Γ_b to the total circulation Γ_{tot} (the difference between Γ_{tot} and Γ_b is $\sum_{i=1}^{M}\Gamma_i$, the total circulation in the intense vortices). To obtain these data, the original background vorticity was multiplied by constants ranging from 0 to 3. Circles correspond to Sequence I (starting at 14 rotations) and squares correspond to Sequence II (starting at 172 rotations).

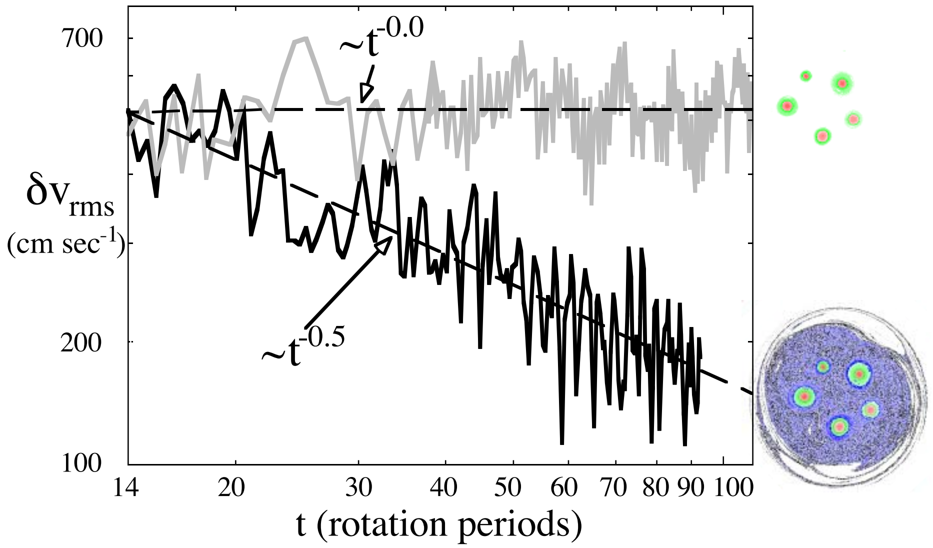

Figure 4.9: Cooling curves for vortex crystal with (black) and without (grey) background vorticity. Time t is normalized to the rotation period of the vortex crystal with background vorticity, $\tau_{\text{rot}} = 1.07$ ms.

In both sets of simulations, the number of intense vortices M remained fixed, with the exception of the data point to the far right, in which a small vortex was sheared apart toward the end of the simulation. As the background vorticity level increases from zero, vortex cooling increases and we observe growth in α. As $\Gamma_b/\Gamma_{\text{tot}}$ continues to increase, α reaches a maximum value and then begins to fall.

A rise and fall of α as $\Gamma_b/\Gamma_{\text{tot}}$ increases from 0 to 1 is consistent with our view that vortex cooling (in the absence of mergers) requires the turbulent mixing of an inhomogeneous background by the intense vortices. When there is no background, there is no vortex cooling. When $\Gamma_b/\Gamma_{\text{tot}}$ is close to 1, the velocity field is dominated by the contribution from the background vorticity. Presumably, the cooling rate becomes small in this limit because the vortices essentially become passive test particles and lose their capacity to mix the background.

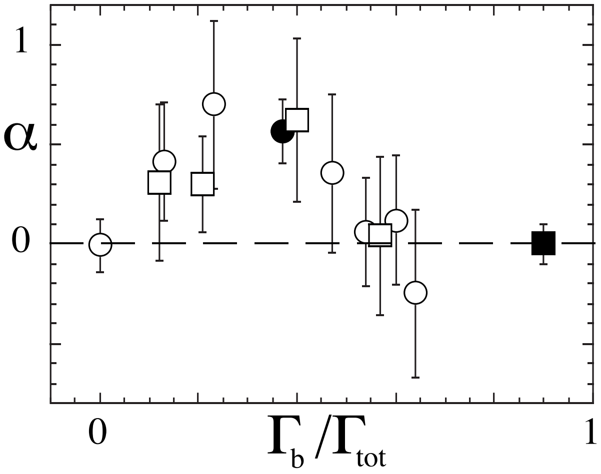

Figure 4.10: Cooling exponent α versus Γ_b/Γ_{tot}. Circles correspond to Sequence I (Fig. 4.3.b) starting at $t \approx 15$ msec (14 rotation periods), and squares correspond to Sequence II (Fig. 4.5.b) starting at $t \approx 40$ msec (172 rotation periods). The shaded symbols mark the cooling exponents for the original simulated flows. To obtain the remaining data, the original background vorticity ($\zeta \leq 1 \times 10^4$ sec^{-1} in Sequence I; $\zeta \leq 6.8 \times 10^4$ sec^{-1} in Sequence II) was multiplied by constants ranging from 0 to 3.

4.6 Conclusion

The conventional picture of freely relaxing 2D turbulence (with a single sign of vorticity) involves the chaotic advection of intense vortices punctuated by occasional mergers until only a single vortex remains. In experiments with magnetized electron columns, we have seen that mergers can stop due to the spontaneous formation of a vortex crystal. In this chapter, we have argued that the observed vortex crystals can be explained without incorporating physics beyond 2D Euler theory [Eq. (4.2)], despite small differences between a magnetized electron column and an ideal 2D fluid. Our argument was based on a comparison of two experiments to the results of a VIC simulation that numerically integrates the 2D Euler equations. We found good quantitative agreement in the evolution of the number of intense vortices M and in the cooling of their chaotic advection, described by $\delta v_{\mathrm{rms}}(t)$.

Even so, there were some issues to address. A magnetized electron column and a VIC simulation both consist of a finite number of point-vortices N. The 2D Euler equations govern the ensemble averaged vorticity distribution of a point-vortex gas only in the lowest order mean field approximation, which neglects fluctuations due to finite N. A statistical treatment of these fluctuations leads to a collision term on the right hand side of the continuity equation 2.a, which goes to zero as N goes to infinity and the fluctuations become negligible [102, 103]. There was concern that the collision term due to finite N was responsible for vortex cooling. However, the cooling curve $\delta v_{\mathrm{rms}}(t)$ did not change in Sequence I (Fig. 4.3) when N was decreased from 8×10^5 to 4×10^5 to 1×10^5 (Fig. 4.4.b). Moreover, the simulation curves fell within the scatter of the cooling curve for the experiment, which had $N \sim 10^8$ point-vortices. These results strongly suggest that finite N effects are not important to the formation of vortex crystals.

Another question concerned viscosity in the Navier-Stokes equations. In Sec. IV, we showed that a small level of viscosity can destroy the process of vortex crystal formation entirely (Fig. 4.8). Specifically, we found that Sequence I requires a Reynolds number $R \equiv \Gamma_{\mathrm{tot}}/\nu$ much greater than 10^5 to produce a vortex crystal. For $R \leq 10^5$, viscosity expands the vortices sufficiently fast so that they merge before they have time to settle into a vortex crystal geometry.

We have also discussed a mechanism for vortex cooling that is consistent with inviscid incompressible 2D fluid dynamics [Eq. (4.2)]. In a recent paper [60], Jin and Dubin showed that vortex crystals are well described as states that maximize an entropy functional of the background vorticity distribution, subject to the constraints of 2D Euler flow. This result suggests that the system is driven to a vortex crystal equilibrium through a process that requires the ergodic mixing of the background vorticity.

When the background circulation is much less than the combined circulation of the intense vortices (but not zero), it is reasonable that the vortices can generate the required mixing. On the other hand, when the background circulation dominates, the vortices become less effective mixers. Therefore, if the vortex cooling is driven by the turbulent mixing of the background by the intense vortices, the cooling rate should first rise and then fall as Γ_b increases from zero. Our simulation results are consistent with this picture (Fig. 4.10). When the background was removed, there was no vortex cooling and the intense vortices remained out of equilibrium. Only when the intense vortices were immersed in a low level of background vorticity did they cool toward a pattern in uniform rotation. As $\Gamma_b/\Gamma_{\text{tot}}$ was adjusted closer to 1, the rate of vortex cooling dropped below the accuracy of our measurements.

Finally, we note that the vorticity distributions in magnetized electron columns have two distinct features that may contribute to the arrest of vortex mergers and to the formation of vortex crystals. First, they have a single sign of (positive) vorticity. The effect on vortex crystal formation of adding negative vorticity to the flow is a subject of current research. Second, the background vorticity has a sharp edge where ζ drops rapidly to zero. The interaction between the intense vortices and surface-waves (Kelvin-waves) at the edge can not be ignored in a general treatment of the dynamics. A detailed study of this nonlinear interaction has recently been carried out and it has been shown to contain a plausible mechanism of vortex cooling at late times [106].

This chapter has been published in Physics of Fluids **11**, D. A. Schecter, D. H. E. Dubin, K. S. Fine and C. F. Driscoll, 905-914 (1999). D. A. Schecter was the primary investigator and author of this paper.

References

[1] D.G. Dritschel and B. Legras, "Modeling oceanic and atmospheric vortices," Phys. Today **46**, 44 (1993).

[2] A. P. Ingersoll, "Atmospheric dynamics of outer planets," Science **248**, 308 (1990).

[3] P. S. Marcus, "Numerical simulations of Jupiter's Great Red Spot," Nature **331**, 693 (1988).

[4] P. S. Marcus, "Vortex dynamics in a shearing zonal flow," J. Fluid Mech **215**, 393 (1990).

[5] J. Pedlosky, *Geophysical Fluid Dynamics* (Springer-Verlag New York Inc., 1987).

[6] R. C. Davidson, *Physics of Nonneutral Plasmas*, pp. 289-311 (Addison-Wesley Pub. Co., 1990).

[7] C. F. Driscoll, K. S. Fine, X.-P. Huang, T. B. Mitchell, and B. P. Cluggish, "Vortices and turbulent relaxation in magnetized electron columns," in *Transport, Chaos and Plasma Physics 2*, S. Benkadda, F. Doveil and Y. Elskens, editors, pp. 19-29 (World Scientific, Singapore, 1996).

[8] C. F. Driscoll and K. S. Fine, "Experiments in vortex dynamics in pure electron plasmas," Phys. Fluids B **2**, 1359 (1990).

[9] K. S. Fine, A. C. Cass, W.G. Flynn, and C. F. Driscoll, “Relaxation of 2D turbulence to vortex crystals,” Phys. Rev. Lett. **75**, 3277 (1995).

[10] X.P. Huang, K.S. Fine and C.F. Driscoll, “Coherent vorticity holes from 2D turbulence decaying in a background shear flow,” Phys. Rev. Lett. **74**, 4424 (1995).

[11] A.C. Cass, “Experiments on vortex symmetrization in magnetized electron columns,” Ph.D. dissertation, University of California at San Diego (1998).

[12] C.H. Liu and Lu Ting, “Interaction of decaying trailing vortices in spanwise shear flow,” Comp. & Fluids **15**, 77 (1987).

[13] C.G. Rossby, “On the displacements of intensity changes of atmospheric vortices,” J. Mar. Res. **7**, 175 (1948).

[14] V. A. Bogomolov, “On the Motion of a Vortex on a Rotating Sphere,” Izvestiya, Atmos. and Oceanic Phys. **21**, 298 (1985).

[15] M. DeMaria, “Tropical cyclone motion in nondivergent barotropic model,” Mon. Weath. Rev. bf 113, 1199 (1985).

[16] R.K. Smith and W. Ulrich, “An analytic theory of tropical cyclone motion using a barotropic model,” J. Atmos. Sci **47**, 1973 (1990).

[17] J. L. Evans, G. J. Hollan and R. L. Elsberry, “Interactions between a barotropic vortex and an idealized subtropical ridge. Part I: Vortex motion,” J. Atmos. Sci. **48**, 301 (1991).

[18] W. Ulrich and R.K. Smith, “A numerical study of tropical cyclone motion using a barotropic model. II: Motion in spatially varying zonal flows,” Q. J. R. Meteorol. Soc. **117**, 107 (1991).

[19] R.K. Smith, “An analytic theory of tropical cyclone motion in a barotropic shear flow,” Q. J. R. Meteorol. Soc. **117**, 685 (1991).

[20] G.M. Reznik, “Dynamics of singular vortices on the beta-plane,” J. Fluid Mech. **240**, 405 (1992).

[21] R.K. Smith and H. C. Weber, “An extended analytic theory of tropical cyclone motion in a barotropic shear flow,” Q. J. R. Meteorol. Soc. **119**, 1149 (1993).

[22] R.K. Smith,“On the theory of tropical cyclone motion,” in *Tropical Cyclone Disasters*, Lighthill et al (ed.), Peking Univ. Press, Beijing, 264 (1993).

[23] R.K. Smith and W. Ulrich, “Vortex motion in relation to the absolute vorticity gradient of the vortex environment,” Q. J. R. Meteorol. Soc. **119**, 207 (1993).

[24] G. M. Reznik and W.K. Dewar, “An analytic theory of distributed axisymmetric barotropic vortices on the β-plane,” J. Fluid. Mech **269**, 301 (1994).

[25] G.G. Sutyrin and G.R. Flierl, “Intense vortex motion on the beta plane: Development of beta gyres,” J. Atmos. Sci. **51**, 773 (1994).

[26] R.T. Williams and J. C.-L. Chan, “Numerical studies of the beta effect in tropical cyclone motion. Part II: Zonal mean flow effects,” J. Atmos. Sci. **51**, 1065 (1994).

[27] G.K.Korotaev and A. B. Fedotov, “Dynamics of an isolated barotropic eddy on a beta-plane,” J. Fluid. Mech. **264**, 277 (1994).

[28] Bin Wang and Xiaofan Li, “Propagation of a tropical cyclone in meridionally varying zonal flow: An energetic analysis,” J. Atmos. Sci. **52**, 1422 (1995).

[29] G.G. Sutyrin, J. S. Hesthaven,J. P. Lynov and J. Juul Rasmussen, “Dynamical properties of vortical structures on the beta-plane,” J. Fluid. Mech **268**, 103 (1994).

[30] Stefan G. Llewllyn Smith, “The motion of a non-isolated vortex on the beta-plane,” J. Fluid. Mech **346**, 149 (1997).

[31] G.F. Carnevale, R.C Kloosterziel and G.J.F. Van Heist, “Propagation of barotropic vortices over topography in a rotating tank,” J. Fluid Mech. **233**, 119 (1991).

[32] H.E. Willoughby, “Linear motion of a shallow-water, barotropic vortex,” J. Atmos. Sci. **45**, 1906 (1988).

[33] H.L. Berk, C.E. Nielsen and K.V. Roberts, “Phase space hydrodynamics of equivalent nonlinear systems,” Phys. Fluids **13**, 980 (1970).

[34] T.H. Dupree, “Theory of phase-space density holes,” Phys. Fluids **25**, 277 (1981).

[35] R.H. Berman, D.J. Tetreault, T.H. Dupree, and T. Boutros-Ghali, “Computer simulation of nonlinear ion-electron instablility”, Phys. Rev. Lett **48**, 1249, (1982).

[36] T.H. Dupree,“Growth of phase-space density holes,” Phys. Fluids **26**, 2460 (1983).

[37] P.W. Terry, P.H. Diamond, T.S. Hahm, “The structure and dynamics of electrostatic and magnetostatic drift holes,” Phys. Fluids B **2**, 2048 (1990).

[38] J. Juul. Rasmussen, J. P. Lynov, J.S.Hesthaven,and G.G. Sutyrin, "Vortex dynamics in Plasmas and Fluids," Plasma Phys. Control. Fusion **36**, B193 (1994).

[39] M.V. Melander, J.C. McWilliams and N.J. Zabusky, "Axisymmetrization and vorticity-gradient intensification of an isolated two-dimensional vortex through filamentation," J. Fluid Mech. **178**, 137 (1987).

[40] D.A. Bachman, "Nonlinear phenomena in a pure electron plasma studied with a 2D fluid code," Ph.D. dissertation, California Institute of Technology (1997).

[41] P. Koumoustakos, "Inviscid axisymmetrization of an elliptical vortex," J. Comp. Phys. **138**, 821 (1998)

[42] M.T. Montgomery and J. Enagonio, "Tropical cyclogenesis via convectively forced vortex rossby waves in a three-dimensional quasigeostrophic model," J. Atmos. Sci. **55**, 3176 (1997).

[43] S. Pillai and R.W. Gould, "Damping and trapping in 2D inviscid fluids," Phys. Rev. Lett. **73**, 2849 (1994).

[44] K.M. Case, "Stability of inviscid plane Couette flow," Phys. Fluids **3**, 143 (1960).

[45] N.J. Balmforth and P.J. Morrison, "Singular eigenfunctions for shearing fluids," preprint.

[46] G.G. Sutyrin, "Azimuthal waves and symmetrization of an intense vortex," Sov. Phys. Dokl. **34**, 104 (1989).

[47] M.T. Montgomery and C. Lu, “Free Waves in Barotropic Vortices. Part I: Eigenmode Structure,” J. Atmos. Sci. **54**, 1868 (1997).

[48] R. J. Briggs, J. D. Daugherty, and R. H. Levy, “Role of Landau damping in crossed-field electron beams and inviscid shear flow,” Phys. Fluids **13**, 421 (1970).

[49] N.R. Corngold, “Linear response of the two-dimensional pure electron plasma: Quasimodes for some model profiles,” Phys. Plasmas **2**, 620 (1995).

[50] R.L. Spencer and S.N. Rasband, “Damped diocotron quasi-modes of non-neutral plasmas and inviscid fluids,” Phys. Plasmas **4**, 53 (1997).

[51] A.V. Timofeev, “Resonance effects in oscillations of nonuniform flows of continuous media” in *Reviews of Plasma Physics* **17**, B.B. Kadomstev (ed.), Consultants Bureau, New York, 193 (1992).

[52] L. Landau, “On the vibration of the electronic plasma,” J. Phys. U.S.S.R. **10**, 25 (1946).

[53] N.A. Krall and A.W. Trivelpiece, *Principles of Plasma Physics*, San Francisco Press (1986).

[54] F.F. Chen, *Introduction to plasma physics and controlled fusion* **1** , Plenum Press (1990).

[55] N.G. Van Kampen, “On the theory of stationary waves in plasmas,” Physica **21**, 949 (1955).

[56] K.M. Case, “Plasma oscillations,” Annals of Physics **7**, 349 (1959).

[57] T.M. O'Neil, "Collisionless damping of nonlinear plasma oscillations," Phys. Fluids **8**, 2255 (1965).

[58] A. Leonard, "Vortex methods for flow simulations," J. Comp. Phys. **37**, 288 (1980).

[59] C. K. Birdsall and A. B. Langdon, *Plasma Physics Via Computer Simulation*, (Adam Hilger, 1991).

[60] D.Z. Jin and D. H. E. Dubin, "Regional maximum entropy theory for vortex crystal formation," Phys. Rev. Lett. **80**, 4434 (1998).

[61] M. R. Brown, "Experimental evidence of rapid relaxation to large-scale structures in turbulent fluids: Selective decay and maximal entropy," J. Plasma Physics, Vol. **57**, Part 1, 203 (1996).

[62] D. Lynden-Bell, "Statistical mechanics of violent relaxation in stellar systems," Mon. Not. R. Astron. Soc. **136**, 101 (1967).

[63] R. Robert and J. Sommeria, "Statistical equilibrium states for two-dimensional flows," J. Fluid Mech. **229**, 291 (1991).

[64] J. Miller, P. B. Weichman and M. C. Cross, "Statistical mechanics, Euler equations and Jupiter's Great Red Spot," Phys. Rev. A. **45**, 2328 (1992).

[65] J. Miller, "Statistical mechanics of Euler equations in two dimensions," Phys. Rev. Lett. **65**, 2137 (1990).

[66] A. Thess, J. Sommeria and B. Jütner, "Inertial organization of a two-dimensional turbulent vortex street," Phys. Fluids **6**, 2417 (1994).

[67] L. Onsager, "Statistical hydrodynamics," Nuovo Cimento Suppl. **6**, 279 (1949).

[68] G. Joyce and D. Montgomery, "Negative temperature states for the two-dimensional guiding-center plasma," J. Plasma Phys. **10**, 107 (1973).

[69] D. L. Book, Shalom Fisher, and B . E. McDonald, "Steady-state distributions of interacting discrete vortices," Phys. Rev. Lett. **34**, 4 (1975).

[70] T.S. Lundgren and Y.B. Pointin, "Statistical mechanics of two-dimensional vortices," J. Stat. Phys. **17**, 323 (1977).

[71] R.A. Smith and T.M. O'Neil, "Nonaxisymmetric thermal equilibria of a cylindrically bounded guiding-center plasma or discrete vortex system," Phys. Fluids B **2**, 2961 (1990).

[72] D. Montgomery, X. Shan and W. H. Matthaeus, "Navier-Stokes relaxation to Sinh-Poisson states at finite Reynolds numbers," Phys. Fluids A **5**, 2207 (1993).

[73] F. P. Bretherton and D. B. Haidvogel, "Two-dimensional turbulence above topography," J. Fluid Mech. **78**, 129 (1976).

[74] W. H. Matthaeus and D. Montgomery, "Selective decay hypothesis at high mechanical and magnetic Reynolds numbers," Annals New York Academy of Sciences, 203 (1980).

[75] X.-P. Huang and C. F. Driscoll, "Relaxation of 2D turbulence to a metaequilibrium near the minimum enstrophy state," Phys. Rev. Lett. **72**, 2187 (1994).

[76] M. V. Melander, N. J. Zabusky and J. C. McWilliams, "Symmetric vortex merger in two dimensions: causes and conditions," J. Fluid.Mech **195**, 303 (1988).

[77] G. F. Carnevale, J. C. McWilliams, Y. Pomeau, J. B. Weiss, and W. R. Wang, "Evolution of vortex statistics in two-dimensional turbulence," Phys. Rev. Lett. **66**, 2735 (1991).

[78] K.S. Fine, C.F. Driscoll, J.H. Malmberg and T.B. Mitchell, "Measurements of symmetric vortex merger," Phys. Rev. Lett. **67**, 588 (1991).

[79] I.M. Lansky, T.M. O'Neil and D.A. Schecter, "A theory on vortex merger," Phys. Rev. Lett. **79**, 1479 (1997).

[80] R. Fjortoft, "On the changes in the spectral distributions of kinetic energy for two-dimensional non-divergent flow," Tellus **5**, 225 (1953).

[81] D.G. Dritschel, "The repeated filamentation of two-dimensional vorticity interfaces," J. Fluid. Mech **194**, 511 (1988).

[82] N.K.-R. Kevlahan and M. Farge, "Vorticity filaments in two-dimensional turbulence: creation, stability and effect," J. Fluid. Mech. **346**, 49 (1997).

[83] G.K. Batchelor, "Computation of the energy spectrum in homogeneous two-dimensional turbulence," Phys. Fluid Supp. II, II-233 (1969).

[84] Reta Beebe,"Characteristic zonal winds and long-lived vortices in atmospheres of the outer planets," Chaos **4**, 113 (1994); for data.

[85] I.B. Bernstein, J.M. Greene and M.D. Kruskal, Phys. Rev. **108**, 546 (1957).

[86] M.K. Nezlin, "Rossby solitary vortices, on giant planets and in the laboratory," Chaos **4**, 187 (1994)

[87] I.S. Gradshteyn and I.M. Ryzhik, *Table of Integrals, Series and Products*, Fifth Edition, ed. A. Jeffrey, Academic Press, Inc., 613 (1994).

[88] A.P. Bassom and A.D. Gilbert, "The spiral wind-up of vorticity in an inviscid planar vortex," J. Fluid. Mech. **371**, 109 (1998).

[89] T.S. Lundgren,"Strained spiral vortex model for turbulent fine structure," Phys. Fluids **25**, 2193 (1982).

[90] W.McF. Orr, "Stability and instability of steady motions of a perfect fluid," Proc. R. Irish. Acad. **27**, 6 (1907).

[91] S.N. Brown and K. Stewartson, "On the algebraic decay of disturbances in a stratified linear shear flow," J. Fluid. Mech. **100**, 811 (1980).

[92] Lord Kelvin, "On the vibrations of a columnar vortex," Phil. Mag. **10**, 155 (1880).

[93] A.J. Bernoff and J.F. Lingevitch, "Rapid relaxation of an axisymmetric vortex," Phys. Fluids **6**, 3717 (1994).

[94] P.B.Rhines and W.R.Young, "How rapidly is a passive scalar mixed within closed streamlines?," J. Fluid Mech. **133**, 133 (1983).

[95] R.A. Smith and M.N. Rosenbluth, "Algebraic instability of hollow electron columns and cylindrical vortices," Phys. Rev. Lett. **64**, 649 (1990).

[96] Lord Kelvin, "On a disturbing infinity in Lord Rayleigh's solution for waves in a plane vortex stratum," Nature **23**, 45 (1880).

[97] L. J. Campbell and R. M. Ziff, "Vortex patterns and energies in a rotating superfluid," Phys. Rev. B **20**, 1886 (1979).

[98] A.J. Chorin, "Numerical study of slightly viscous flow," J. Fluid Mech. **57** 785-796 (1973).

[99] R. A. Smith, "Effects of electrostatic confinement fields and finite gyroradius on an instability of hollow electron columns," Phys. Fluids B **4**, 287 (1992).

[100] C. F. Driscoll, "Observation of an unstable $l = 1$ diocotron mode on a hollow electron colulmn," Phys. Rev. Lett. **64**, 645 (1990).

[101] A. J. Peurrung and J. Fajans, "A limitation on the analogy between pure electron plasmas and two-dimensional inviscid fluids," Phys. Fluids B **5**, 4295 (1993).

[102] D. H. E. Dubin and T. M. O'Neil, "Two-dimensional guiding-center transport of a pure electron plasma," Phys. Rev. Lett. **60**, 1286 (1988).

[103] D. H. E. Dubin and T. M. O'Neil, "Two-dimensional bounce-averaged collisional particle transport in a single species non-neutral plasma," Phys. Plasmas **5**, 1305 (1998).

[104] J. C. McWilliams, "The vortices of two-dimensional turbulence," J. Fluid Mech. **219**, 361 (1990).

[105] S. Chandrasekar, "Stochastic problems in physics and astronomy," Rev. Mod. Phys. **15**, 1 (1943).

[106] D. Z. Jin, Ph.D. dissertation, University of California at San Diego (1999).